Fault Tolerant Model Predictive Control of an Electrical Variable Transmission

Dries Heungens

Supervisors: Prof. dr. ir. Jan Melkebeek, Prof. dr. ir. Frederik De Belie
Counsellor: Joachim Druant

Master's dissertation submitted in order to obtain the academic degree of
Master of Science in Electromechanical Engineering

Department of Electrical Energy, Metals, Mechanical Constructions & Systems
Chair: Prof. dr. ir. Luc Dupré
Faculty of Engineering and Architecture
Academic year 2016-2017

GHENT UNIVERSITY

Fault Tolerant Model Predictive Control of an Electrical Variable Transmission

Dries Heungens

Supervisors: Prof. dr. ir. Jan Melkebeek, Prof. dr. ir. Frederik De Belie
Counsellor: Joachim Druant

Master's dissertation submitted in order to obtain the academic degree of
Master of Science in Electromechanical Engineering

Department of Electrical Energy, Metals, Mechanical Constructions & Systems
Chair: Prof. dr. ir. Luc Dupré
Faculty of Engineering and Architecture
Academic year 2016-2017

GHENT UNIVERSITY

Permission of Usage

Toelating tot bruikleen

Preface

Motivation

One year ago, each student was asked to choose a subject of their master dissertation. An enormous list of proposals became available. The most important aspect to ensure the successful completion of a thesis is choosing a subject in your own personal interest. It's my conviction that *energy-related* problems will be one of the greatest challenges that our generation will have to deal with. Using energy in an efficient way is thus very important. A second main challenge for our generation will be the reduction of waste. Our current mindset is the following: '*If something doesn't work any more, we just throw it away*'. Tough it is possible that a minor fix can solve the problem such that, the device (e.g. you phone) can still be used. To solve this, people should be noted what is broken in the system such that they can evaluate the seriousness of this problem.

I would like to offer my contribution to solve these challenges. This is why I chose this master dissertations. It covers both topics. The implementation of the Electrical Variable Transmission in HEV's is a way to reduce the fuel consumption and can result in less air pollution. The second major subject of this master dissertation is the implementation of a fault-detection system, covering the second reason of my choice.

Acknowledgments

During the development of this thesis, assistance was offered from various direction, therefore I would like to thank these people:

First , Drof. Dr. Ir. J. Melkebeek. The professor teaching every course on electrical machines and drives. His course are the base of this master dissertation and are an added value to my education.
My supervisor: Prof. Dr. Ir. F. De Belie, providing valuable feedback concerning the research topics and pointing all faces in the same direction.
ir. Joachim Druant, my counsellor. Without him, I would not have been able to write this master dissertation. Thank you for the numerous times listening to my questions and the hints you gave me during the year. I hope this master dissertation is useful for your own PD research, returning the favour.

My classmates Lynn, Wannes, Jelle, Andreas and Jasper, for cheering up the the atmosphere in building 913.
Last, my parents and friends, who haven been supportive and listened to my stories concerning this master dissertation. Special thanks to Femke, Thomas and Thijs for proofreading this text

Fault Tolerant Model Predictive Conrtol of an Electrical Variable Transmission

by

Dries Heungens

Master's dissertation submitted in order to obtain the academic degree of Master of Science in Electromechanical Engineering

Academic year: 2016-2017

Supervisors: Prof. dr. ir. J. Melkebeek, Prof. ir. F. De Belie
Counsellor: Ir. J. Druant
Faculty of Engineering and Architecture
Ghent University

Department of Electrical Energy, Metals, Mechanical Construction & Systems
Chair: Prof. dr. ir. Luc Dupr

Summary

The user of an Permanent Magnet Electrical Variable Transmission(PM-EVT) wants the system to be reliable. To do this, a fault detection system must be designed. Different faults exist in electrical machines. In chapter 2, these faults are discussed, and also how some of them can be detected. From this chapter it can be concluded that a reliable fault-detection system requires an accurate model and controller. This is the first main subject of this master dissertation and is discussed in chapter 3 and 4. The controller regulates the current and is based on the method Finite Set Model Based Predictive Control(FS-MBPC). The model described in chapter 3 is, due to practical reasons, not useful for this control-method. Therefore simplifications will have to be made. To this end, the entire system is implemented in a matlab-simulink environment. Afterwards, the controller is compared to a PI-controller. This is elaborated in chapter 5. After designing a controller, having a good performance over the entire operation range, the control-method can be extended with a fault-detection system, which is the second subject of this thesis. This was done for open-switch failures in the inverters, feeding the PM-EVT, and is elaborated

in chapter 6. Simulation results prove the effective functioning of this detection method. A fault-diagnosis only is not enough, if possibble, a fault-tolerant operation mode should be activated as well. It is derived that this is possible, and is discussed in detail in the last part of chapter 6.

Keywords: Model Based Predictive Control, Permanent-Magnet Electrical Variable Transmission, Fault detection, Fault tolerant operation

Fault Tolerant Model Predictive Control of an Electrical Variable Transmission

Dries Heungens
Supervisors: ir. Joachim Druant, prof. dr. ir. Fredrik De Belie & prof. dr. ir. Jan Melkebeek

***Abstract*— A Permanent Magnet Electrical Variable Transmission (PM-EVT) is an electrical machine consisting of a stator and two concentric rotors. The inner diameter of the inner rotor is layered with PM's. For each of its applications, reliability is an important issue. It is required that the electrical machine itself and the accompanied inverters operate correctly. When a fault occurred, the user wants to know what caused this fault and, if possible, a fault-tolerant operation mode must be activated. In this paper, a fault tolerant operation mode has been derived if an open-switch fault occurrs within one of the inverters. To do this, a fault-detection & desicion system had to be designed. This mechanism is an extension of the already used Finite-Set Model Based Predictive Control (FS-MBPC) algorithm. No extra measurements are required. A reliable fault-detection system requires an accurate prediction of the current in any operation mode. Due to cross-effects and saturation, the inductance parameters in the model of the PM-EVT are variable, depending on the operation point. Therefore a more detailed model has been derived, which is still suitable to be used in an Field Programmable Array. Computer simulations were executed to validate the proposed system.**

***Index Terms*— Model Based Predictive Control, Electrical Variable Transmission, Fault-detection, Fault tolerant operation**

I. Introduction

A PM-EVT can be used in various application. The most commonly known application is the use in a Hybrid Electrical Vehicle (HEV). It replaces the planetary gear set and two electrical machines[1]. This is however not the only application. It is useful in any application where mechanical and electrical drives are combined. For each application, the user wants the system to be reliable. More and more attention is paid to this, especially in industry. The break down of a machine results in downtime which is also translated into decreased earnings. If an entire spare one is available, this downtime can be minimized. Though an entire production unit can be out of operation for hours [2]. Further an extra cost is added for the new electrical machine. In this throwaway society and the pressure to reduce the downtime, it may occur that the entire system is replaced while a minor repair can solve the problem. If the user knows what is wrong with the electrical system, this can reduce the down-time and the extra cost. To do this, a fault-diagnosis system can be useful. As an extension, if possible, the system should activate a fault tolerant operation mode.

This electrical machine consists of a stator and two concentric rotors. This is shown in Fig 1. The inner diameter of the inner rotor is mounted with PM's. The main advantage of the EVT lies within the ability to split power.[3]. The two rotors are the mechanical ports of the transmission. The energy transfer between both rotors occurs in an electromagnetic way. The remaining power is then transferred in a purely electric way. To this end, two electrical ports are available, being the stator and inner rotor windings. The latter is available trough slip rings. The power flow depends on the speed difference between both rotors [3]. Both electrical ports are connected to a common battery by two back to back 2L-VSI inverters. This battery can be used to add extra power to the stator such that an extra torque is transferred to the outer rotor. Naturally, this battery can also be used to store this electrical energy. Since some application do not require a high continuous stator torque. When the flux-linkage between the stator and outer rotor is high, needless iron losses are induced within the stator. Therefore a DC field winding is installed, changing the flux-linkage between the stator and outer rotor, while maintaining the flux-linkage between both rotors.

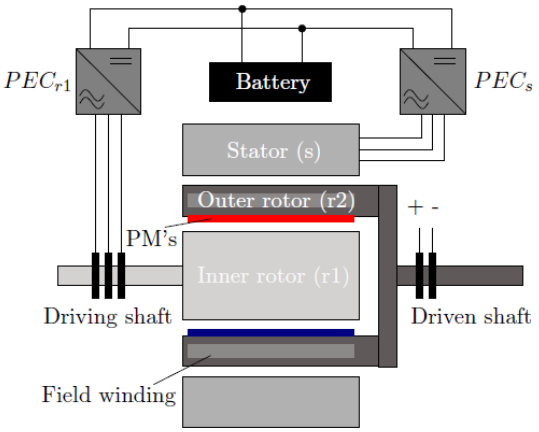

Fig. 1: EVT

The complexity of this electrical system implies that a lot of possible faults may occur in electrical machines. These may occur within the machine itself, but also in the inverters feeding the stator and inner rotor. In this paper, there will be focussed on as specific inverter-faults, mainly, open-switch failures in the inverters. In [4], it has been proven that a fault-detection system can be derived as an extension of the control-method Finite-Set Model Based Predictive Control (FS-MBPC). A fault-detection system based on FS-MBPC, requires an accurate prediction of the current as well. To this end, a detailed model is required as well. Though, it has to be taken into account that the the model is still useful to implement in an Field Programmable Area (FPGA). This will be the first subject of this paper. Afterwards the detection-

system will be explained.

Finally, it has been shown in [4], that by connecting the affected inverter-leg, to the center-tap of the system the DC-bus the machine can still operate.

II. Finite Set Model Based Predictive Control

The controller must be designed such that it can determine what the optimal switch-configuration in each inverter will be, in order to approximate the reference current, in both windings, as close as possible. Due to the high complexity of this system, controlling the current is a major challenge. A PI-controller can be used to do this. However, the parameters of this controller are tuned based upon step-response or models and are thus fixed. For linear systems this is fine, but since this system is highly non-linear, the performance of the controller will be sub-optimal in some operation points. This is not the case when a MBPC controller is used. When an accurate model is available, the performance of the controller is optimal for almost the entire operation range of the system. It has been shown in literature [5] that FS-MBPC method is one of the better approaches, due to the finite number of switching states of the inverters. There are 64 possible switch configurations if both 2L-VSI are considered.

The FS-MBPC principle is explained in Fig 2. The main purpose of this system is to determine what the optimal switch-configuration will be, at the next time instant.

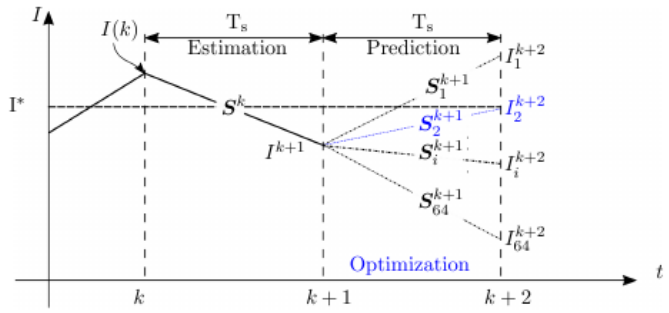

Fig. 2: Principle FS-MBPC

This method can be divided into three steps:

1) Estimation: Using the measurements I^k available at time instant k and the switch configuration $\boldsymbol{S}^k$, determining the voltage coming out of the inverter, the controller can estimate what the current i_{k+1} will be at the next time-instant $k+1$. The switch configuration is the result of the optimization at the previous time step $k-1$.
2) Prediction: Using this estimation as initial condition, the controller determines what the current I_i^{k+2} will be at $k+2$ for every possible switch-configuration.
3) Optimization: Based on a certain cost-function the optimal prediction is then selected. The corresponding switch-configuration will then be set at time instant $k+1$. Afterwards the controller is cleared and the algorithm starts over with the new measurements at $k+1$.

Different cost-functions can be chosen here[6]. In this paper, it is opted to use a cost-function minimizing the squared error between the predictions and the reference value of each current components.

III. Modelling PM-EVT

Using MBPC requires a model. In order to be able to model this PM-EVT, some assumptions are made [7]:

- a three-phases symmetrical winding,
- all windings are sinusoidally distributed,
- skin-effects as well as proximity effects are neglectable,
- influence of the slot openings on the magnetic field is neglectable.

In the qd-reference frame of the outer rotor, the following machine equations are derived.

$$\begin{cases} V_{\mathrm{s,q}} = \mathrm{R_s} I_{\mathrm{s,q}} + p\Psi_{\mathrm{s,q}} - \omega_{\mathrm{r2}}\Psi_{\mathrm{s,d}} \\ V_{\mathrm{s,d}} = \mathrm{R_s} I_{\mathrm{s,d}} + p\Psi_{\mathrm{s,d}} + \omega_{\mathrm{r2}}\Psi_{\mathrm{s,q}} \end{cases} \tag{1a}$$

$$\begin{cases} V_{\mathrm{r1,q}} = \mathrm{R_{r1}} I_{\mathrm{r1,q}} + p\Psi_{\mathrm{r1,q}} - (\omega_{\mathrm{r2}} - \omega_{\mathrm{r1}})\Psi_{\mathrm{r1,d}} \\ V_{\mathrm{r1,d}} = \mathrm{R_{r1}} I_{\mathrm{r1,d}} + p\Psi_{\mathrm{r1,d}} + (\omega_{\mathrm{r2}} - \omega_{\mathrm{r1}})\Psi_{\mathrm{r1,q}} \end{cases} \tag{1b}$$

In these equation, p represents the Laplace operator. ω_{r1} and ω_{r2} denote respectively the electrical speed of the inner and outer rotor. It has been shown in [8], what the impact is of different currents on the flux-linkages in both the stator and inner rotor.

$$\Psi_{\mathrm{s/r1/r2,q/d}} = f(I_{\mathrm{s,q}}, I_{\mathrm{s,d}}, I_{\mathrm{r2,d}}, I_{\mathrm{r1,q}}, I_{\mathrm{r1,d}}) \tag{2}$$

These functions are available under the form of a look-up table. Using this, the derivatives of the flux-linkages to time , in equation 1, can be written as a function of the derivatives of the current components by calculating the *Jacobian* of equations 2

$$\frac{d\boldsymbol{\Psi}}{dt} = \boldsymbol{J}\frac{d\boldsymbol{I}}{dt} \tag{3}$$

where:

$$\frac{d\boldsymbol{\Psi}}{dt} = \begin{bmatrix} \frac{d\Psi_{\mathrm{s,q}}}{dt} & \frac{d\Psi_{\mathrm{s,d}}}{dt} & \frac{d\Psi_{\mathrm{r2,d}}}{dt} & \frac{d\Psi_{\mathrm{r1,q}}}{dt} & \frac{d\Psi_{\mathrm{r1,d}}}{dt} \end{bmatrix}^T \tag{4}$$

$$\frac{d\boldsymbol{I}}{dt} = \begin{bmatrix} \frac{dI_{\mathrm{s,q}}}{dt} & \frac{dI_{\mathrm{s,d}}}{dt} & \frac{dI_{\mathrm{r2,d}}}{dt} & \frac{dI_{\mathrm{r1,q}}}{dt} & \frac{dI_{\mathrm{r1,d}}}{dt} \end{bmatrix}^T \tag{5}$$

$$\boldsymbol{J} = \begin{bmatrix} \frac{\partial\Psi_{\mathrm{s,q}}}{\partial I_{\mathrm{s,q}}} & \frac{\partial\Psi_{\mathrm{s,q}}}{\partial I_{\mathrm{s,d}}} & \frac{\partial\Psi_{\mathrm{s,q}}}{\partial I_{\mathrm{r2,d}}} & \frac{\partial\Psi_{\mathrm{s,q}}}{\partial I_{\mathrm{r1,q}}} & \frac{\partial\Psi_{\mathrm{s,q}}}{\partial I_{\mathrm{r1,d}}} \\ \frac{\partial\Psi_{\mathrm{s,d}}}{\partial I_{\mathrm{s,q}}} & \frac{\partial\Psi_{\mathrm{s,d}}}{\partial I_{\mathrm{s,d}}} & \frac{\partial\Psi_{\mathrm{s,d}}}{\partial I_{\mathrm{r2,d}}} & \frac{\partial\Psi_{\mathrm{s,d}}}{\partial I_{\mathrm{r1,q}}} & \frac{\partial\Psi_{\mathrm{s,d}}}{\partial I_{\mathrm{r1,d}}} \\ \frac{\partial\Psi_{\mathrm{r2,d}}}{\partial I_{\mathrm{s,q}}} & \frac{\partial\Psi_{\mathrm{r2,d}}}{\partial I_{\mathrm{s,d}}} & \frac{\partial\Psi_{\mathrm{r2,d}}}{\partial I_{\mathrm{r2,d}}} & \frac{\partial\Psi_{\mathrm{r2,d}}}{\partial I_{\mathrm{r1,q}}} & \frac{\partial\Psi_{\mathrm{r2,d}}}{\partial I_{\mathrm{r1,d}}} \\ \frac{\partial\Psi_{\mathrm{r1,q}}}{\partial I_{\mathrm{s,q}}} & \frac{\partial\Psi_{\mathrm{r1,q}}}{\partial I_{\mathrm{s,d}}} & \frac{\partial\Psi_{\mathrm{r1,q}}}{\partial I_{\mathrm{r2,d}}} & \frac{\partial\Psi_{\mathrm{r1,q}}}{\partial I_{\mathrm{r1,q}}} & \frac{\partial\Psi_{\mathrm{r1,q}}}{\partial I_{\mathrm{r1,d}}} \\ \frac{\partial\Psi_{\mathrm{r1,d}}}{\partial I_{\mathrm{s,q}}} & \frac{\partial\Psi_{\mathrm{r1,d}}}{\partial I_{\mathrm{s,d}}} & \frac{\partial\Psi_{\mathrm{r1,d}}}{\partial I_{\mathrm{r2,d}}} & \frac{\partial\Psi_{\mathrm{r1,d}}}{\partial I_{\mathrm{r1,q}}} & \frac{\partial\Psi_{\mathrm{r1,d}}}{\partial I_{\mathrm{r1,d}}} \end{bmatrix} \tag{6}$$

In the assumption that the variation of the DC-field current $i_{\mathrm{r2,d}}$ is known, this system is solvable. After discretizing these equations derived above, it is possible to determine the current at the next time-instant.

TABLE I: Controller models

Model	$\Psi_{s,q}$	$\Psi_{s,d}$	$\Psi_{r1,q}$	$\Psi_{r1,d}$
a	$L_{s,q}I_{s,q}$	$L_{s,d}I_{s,d}$	$L_{r1,q}I_{r1,q}$	$L_{r1,d}I_{r1,d}$
b	$L_{s,q}I_{s,q}$	$\boldsymbol{f(I_{s,d}, I_{r2,d})}$	$L_{r1,q}I_{r1,q}$	$L_{r1,d}I_{r1,d}$
c	$L_{s,q}I_{s,q}$	$f(I_{s,d}, I_{r2,d})$	$\boldsymbol{f(I_{r1,q}, I_{s,q})}$	$L_{r1,d}I_{r1,d}$
d	$L_{s,q}I_{s,q}$	$f(I_{s,d}, I_{r2,d})$	$f(I_{r1,q}, I_{s,q})$	$\boldsymbol{f(I_{r1,d}, I_{s,d}, I_{r2,d})}$
e	$\boldsymbol{f(I_{s,q})}$	$f(I_{s,d}, I_{r2,d})$	$f(I_{r1,q}, I_{s,q})$	$f(I_{r1,d}, I_{s,d}, I_{r2,d})$
f	$\boldsymbol{f(I_{s,q}, I_{s,d}, I_{r2,d})}$	$f(I_{s,d}, I_{r2,d})$	$f(I_{r1,q}, I_{s,q})$	$f(I_{r1,d}, I_{s,d}, I_{r2,d})$
g	$f(I_{s,q}, I_{s,d}, I_{r2,d})$	$\boldsymbol{f(I_{s,q}, I_{s,d}, I_{r2,d})}$	$f(I_{r1,q}, I_{s,q})$	$f(I_{r1,d}, I_{s,d}, I_{r2,d})$

IV. Control Design

The entire control system is implemented in a Matlab-Simulink environment, see Fig 3

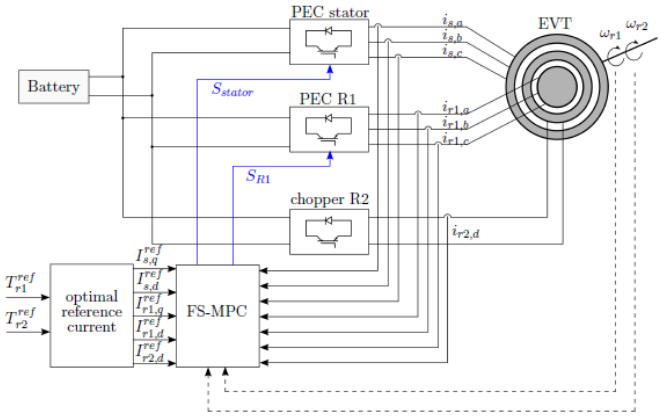

Fig. 3: Control design operation principle

Based on the desired torque at the inner and outer rotor, optimal current values are determined, as described in [9]. The FS-MBPC controller, must regulate the currents, in the stator and inner rotor, as close as possible to the desired values. To do this, the controller determines the optimal switch configuration at each time instant k. The optimal switch configuration, resulting in a certain phase voltage, is then supplied to the EVT-model described in the previous section. When the model described above, is used by the controller, accurate predictions are obtained. Though, this cannot be implemented in reality, since the determination of the Jacobian, requires recursive formulas. Since a fast computational time is required, this cannot be implemented in reality. Therefore the model will have to be simplified. It has been shown in [8], that the impact of some current components on a certain flux-linkage is negligible. For example, due to the decoupling effect between the stator and inner rotor, the impact of a rotor current will have almost no impact on the stator flux linkage.

A sensitivity study has been executed to evaluate the impact of each current component on the controller model. The tested controller models are listed in Tab I. These models, except the ideal model, do not use any look-up tables. Every flux-linkage has been transformed into a function. It is desired that the controller shows an acceptable performance under each operating condition. Therefore the controller was subjected to different test-cases, see Tab II. The DC-bus voltage is set to be 600 V.

TABLE II: Test cases

Case	T_s[Nm]	T_{r1}[Nm]	N_{r1}[rpm]	N_{r2}[rpm]
1	0	0	1500	2500
2	-50	0	1500	2500
3	-100	0	1500	2500
4	-150	0	1500	2500
5	-200	0	1500	2500
6	-250	0	1500	2000
7	-300	0	1500	3000
8	0	-150	1500	2500
9	0	-50	1500	2500
10	-50	-50	1500	2500
11	-100	-100	1500	2500
12	-250	-100	1500	2000

For each test-case combined with a controller-model, the Mean Squared Error MSE and the bias of each current component has been calculated, according to the following formulas.

$$MSE = \frac{1}{N}\sum_{k=1}^{N}(I(k) - I_k^{ref})^2 \tag{7}$$

$$MSE = \frac{1}{N}\sum_{k=1}^{N}|I(k) - I_k^{ref}| \tag{8}$$

The results are shown in, respectively figures 5 and 6. In order to give a compact result, the averaged MSE and bias of all currents is depicted. A first thing to notice, is that the controller has great difficulties for case 6 and 12. In these cases, the reference d-axis stator current $I_{s,d}^{ref}$ is negative, so is the field current $I_{r2,d}^{ref}$. In this operating range, and due to the high DC-bus voltage, the current will highly fluctuate around its desired value. This results in the stator yoke becoming alternating saturated and magnetically linear, see Fig 4.

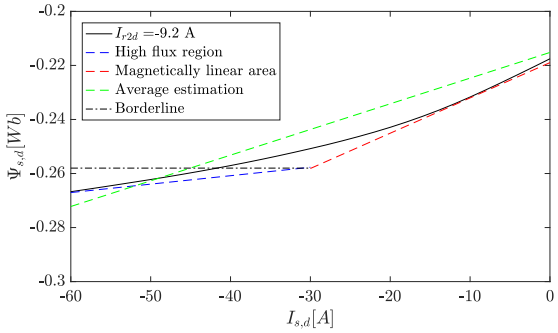

Fig. 4: Issue when using the ideal model. The black line denotes the variation based on FEM-calculations. The blue and the red dotted line denote the discritized function, used in the controller. The dotted black line, denotes the separation between the magnetic linear part and the high flux region, implemented in the controller.

In this figure the d-axis stator flux $\Psi_{\mathrm{s,d}}$ as function of the corresponding current $I_{\mathrm{s,d}}$ is shown. It can be noted that the slope changes continuously. The same can be noticed for $\Psi_{s,q}$. Therefore, the partial derivatives of the stator flux to the stator current, in general, will vary a lot. To overcome this problem an accurate stator model is required. Indeed, model G, using the most accurate stator flux-model performs the best. Note that this model performs even better in comparison to the ideal case. Due to the, rather low, switching frequency of 10 kHz, the controller will still calculate the current components, at the next time-instant $k+1$, based on the present magnetic state of the iron. At the next control instant, it may occur that the magnetic state of the iron is completely different. In the discretized controller model G, this is solved, by using an averaging estimation of magnetic state of the iron, see Fig 4. In this way, better results are obtained.

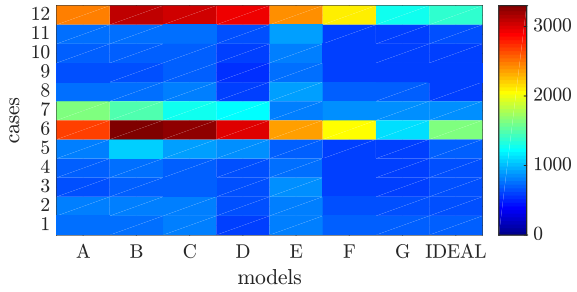

Fig. 5: Average MSE

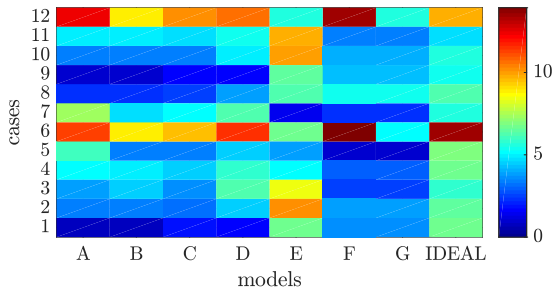

Fig. 6: Average Absolute Bias

V. Inverter faults: fault-detection

After the design of the controller, the entire MBPC-system has been extended with a fault-detection system. This is done for this specific fault: open-switch inverter faults [10]. These represent the situation for which an IGBT doesn't want to close any more. This can be due to a fault in the IGBT itself, but also in the driver providing the switching signal to the IGBT. If this fault occurs, the controller model gives incorrect estimations, such that a bad performance can be noted. In a first step these faults must be modelled. Note that this detection system is applicable for any three-phase system in general.

A. modelling

In order to determine whether or not a fault occurred, the faulty current-vector at $k+1$, see Fig 2, should be calculated as well. This is possible using the optimal controller model, derived in the previous sections. To do this, the voltage over the load must be known. For a 2L-VSI, the output voltage of one inverter leg, is solely determined by the sign of the current. In general, the output voltage can be described as:

$$v^{k}_{y,x\mathrm{n}} = S_{\mathrm{dc},y,x}\frac{\mathrm{V_{dc}}}{2} \tag{9}$$

where $S_{\mathrm{dc},y,x}$ is

$$S_{\mathrm{dc},y,x} = sign(i_{y,x}) \tag{10}$$

where y denotes the stator s or inner rotor r1 and x denotes the phase a, b or c. Using this, the faulty current-vector, at $k+1$, for each fault situation, corresponding to the failure of an IGBT, can be estimated at time instant k. Since there are a total of 12 IGBT's in this electrical system, 12 fault current vectors will be calculated. These values are then stored in the memory of the controller under a matrix form, as well as the estimated faultless-current vector. At the next time instant k+1, the measured currents will be compared with the estimated current vectors, stored in the memory. Since cross-effects and saturation are incorporated into the controller model, the failure of each IGBT will affect every current component in both the stator and inner rotor. In order to determine the optimal estimate, each component of the measured current vector must be compared with the corresponding component of the estimated current vectors. To determine the the optimal estimate, the norm of the difference between both vectors is used as a comparison. The vector corresponding to the smallest norm-difference, then gets a penalty assigned. This is also stored in the memory.

B. Fault decision

Deciding that a switch is broken, based on one penalty assignment to a faulty situation, is very unwise. Therefore some measures will be taken such that a fault-situation is not mistakenly detected. First, it may occur that different fault situations result in the same estimate of the current vector at that time, in order to extract as much information as possible, distributed assignment is used. The principle works as follows. If n fault-situations result in a norm-difference smaller than the accuracy range of the current measurements and the faultless situation is not included, then each fault-situation will be assigned a penalty value of 1/n. If the same situation occurs and the faultless situation is included, then the faultless situation will get more credibility. A penalty of 0.5 will be assigned to the faultless situation and 0.5/(n-1) will be assigned to the other (fault) situations. Secondly, Inaccuracies measuring voltage, current and rotational speed will have an influence on the estimations of the current at the next time instant. Also, the controller model is still an approximation of the real system. For example, temperature variations aren't taken into account. This can also have an impact on the reliability of the estimations. It can occur that an erroneous penalty is assigned to a faulty situation. Therefore the controller will only decide that a fault-situation occurred when multiple penalties are assigned to the proceeding fault-situation. It was opted in [4], to do this by introducing a Moving Average (MA) and a threshold. A MA takes into

account the previous penalties assigned to each fault situation. The priniple is explained in Fig 7.

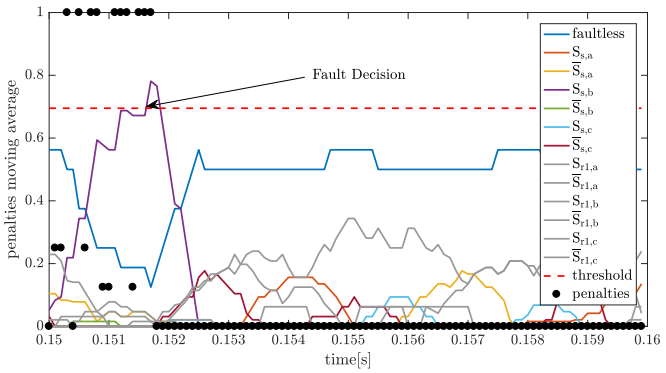

Fig. 7: Principle of a MA and the use of threshold

As stated before, the penalties assigned to each fault situation are stored in the memory. A MA with a window size of n, takes into account by taking an average of the n previously assigned penalty points to a certain fault situation. When, this MA-penalty rises above the threshold, only then the controller will decide that a faulty situation occurred. The question remains what should be chosen for the threshold and window of the MA. It is desired that the fault-decision system works in every operation condition. Simulation pointed out that the number of penalties assigned to a certain fault situation, is strongly depended with the rotational speed of both rotors. The moving average window and the threshold value should be fine-tuned such that a fault-decision system works at any speed. Based on simulations, the optimal values of the MA window and the threshold are determined. This resulted in a MA window of 8 and an threshold value of 0.695.

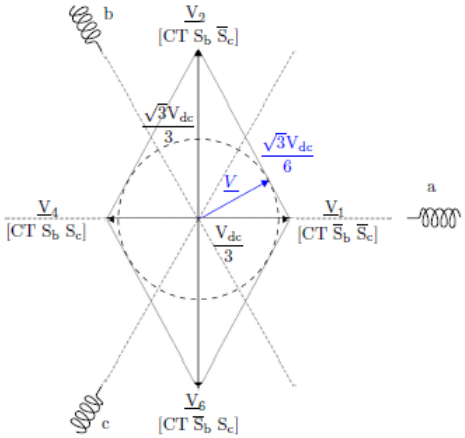

Fig. 8: Space vector representation in a faulty sitation, here phase a is connected to the neutral clamp of the DC-bus.

VI. Fault-tolerant operation

In the previous section a detection/decision-method was derived. However, the decision only is not enough. As stated in the introduction, minor adjustments to the electrical system, ensure the operation of the system when this typical fault occurred. By connecting the affected phase to the neutral point of the DC-bus, a fault tolerant operation is possible. A connection of one inverter-leg to the center-tap, means that output voltage of this leg equals zero but this does not mean that the voltage over the corresponding winding equals zero. The voltage will be equal to the average output phase voltages of each inverter-leg. Since the two IGBT's of the affected IGBT are not used any more, only 4 different switching states remain. The $\alpha\beta$-representation of this load voltage is shown in Fig 8.

From this it can be derived that a fault-tolerant operation is possible when connecting the affected phase to the center-tap. The 4 remaining space vectors are oriented in such a way that a rotating field can be created. The maximum average voltage that can be supplied to the three-phase system, is determined by the inscribed circle of the rhombus, see Fig 8. The inradius of a rhombus with diagonal p and q can be calculated as follows:

$$V_{max} = \frac{p \cdot q}{2\sqrt{p^2+q^2}} = \frac{\frac{2}{3}V_{dc}\frac{2\sqrt{3}}{3}V_{dc}}{2\sqrt{(\frac{2}{3}V_{dc})^2 = (\frac{2\sqrt{3}}{3}V_{dc})^2}} = \frac{\sqrt{3}}{6}V_{dc} \tag{11}$$

This is significantly lower then in the faultless case ($V_{max} = 1/\sqrt{3}V_{dc}$). By considering equations 1, in steady state, it is possible to determine what the average q- and d-axis voltage should be in order to be able to supply a certain current, i.e. torque, to the stator and inner rotor.

Knowing what the maximum deliverable voltage is, it is possible to determine if these currents can be supplied in a fault-tolerant mode or not. The qd-reference frame, rotating at the speed of the PM-field, will thus result in a rotating vector $\underline{V}$. It is this vector, that must be approximated by applying different switch-con

figurations at each control instant. The values of the q- and d-axis voltage, determine the amplitude of the rotating voltage vector.

$$|\underline{V}| = \sqrt{V_{y,q}^2 + V_{y,d}^2} \leq V_{max} \tag{12}$$

Note that the required voltage to supply a certain current in the stator and inner rotor, is depended on the rotational speed of both rotors. This is due to the fact that these values determine the back-EMF in both electrical systems. The maximum torque deliverable stator and inner rotor torque, is shown in respectively Fig 9 and 10. This is also validated by simulation. From this it can be seen that the maximum deliverable torque is a bit lower. This is due to the fact that, the derivative of each flux-component to time also plays a role.

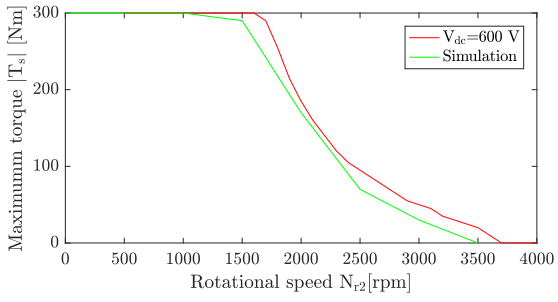

Fig. 9: Maximum deliverable T_s in fault tolerant operation.

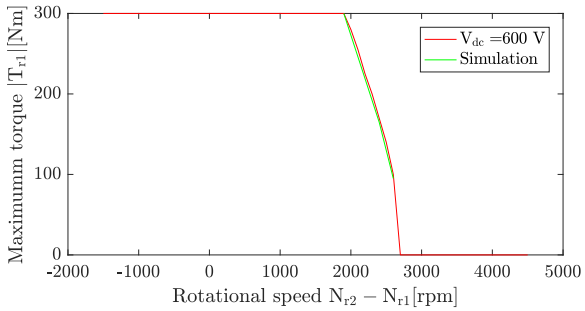

Fig. 10: Maximum deliverable T_{r1} in fault tolerant operation.

VII. SIMULATION

The fault-detection, -decision system and fault tolerant mode are now brought together. If a fault occurs, the fault-detection system, using distributed assignment, will assign penalties to the proceeding fault-situation. If the MA penalty increases above 0.695 the controller will decide that a fault occurred. The controller then gives a close signal to the switch between the infected inverter-leg and the center-tap of the source. In this way a fault tolerant mode is activated. In order to test this controller, the system is completely implemented in matlab. To ensure that this simulation approximates the reality as close as possible, measurement errors and resistor variations are included as well. A fault has been introduced in the the IGBT $S_{s,b}$ connecting phase B to the positive DC-bus at 0. 015 s. Firstly note that the controller model indeed makes accurate estimations of the current in both the q- and d-axis of the stator, see respectively Fig 12 & 13. After only 0.002 seconds, the controller decides that a fault occurred. The controller signals the switch, between the center-tap and inverter-leg b of the PECs, to close. A fault tolerant operation mode is activated. The controller knows this. However, the reference value cannot be approximated any more. This can also be noted when examining the abc-currents, see Fig 11. This is due to the fact that the desired stator torque, being 100 Nm, is larger then the maximum torque deliverable at this speed, in fault tolerant mode, see Fig 9. Therefore, the wanted stator torque is lowered to 60 Nm. In that case, the controller is able to approximate the reference current value. This proves that the statements, derived above, are valid.

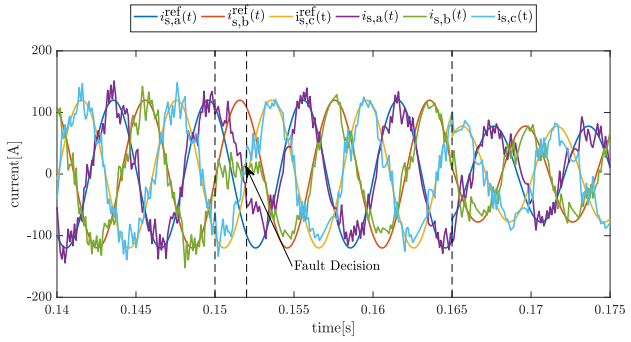

Fig. 11: Simulations: Fault-detecion stator current

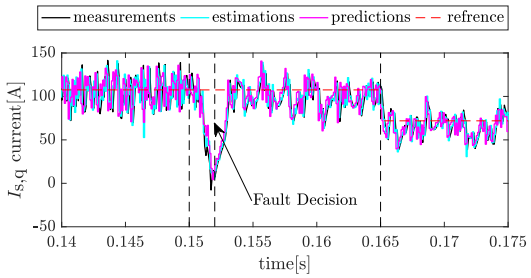

Fig. 12: Simulations: Fault-detecion $I_{s,q}$

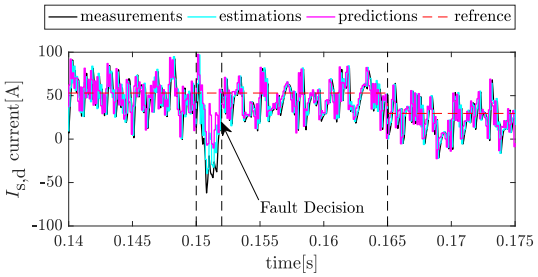

Fig. 13: Simulations: Fault-detecion $I_{s,d}$

VIII. CONCLUSION

In this paper, a controller model and fault-diagnosis system has been derived. The system is designed in such a way that the system is implementable in an FPGA. Simulations showed that the occurence of an open-switch fault in an inverter is detected after less then 2 ms. Further more, a fault tolerant operation mode has been derived. By connecting the affected phase to the neutral clamp of the Dc-bus, the continuity of the machine is ensured. Though, with a reduced maximum deliverable torque

REFERENCES

[1] P. Pisek, B. Stumberger, T. Marcic, and P. Virtic, "Design analysis and experimental validation of a double rotor synchronous pm machine used for hev," *IEEE Transactions on Magnetics*, vol. 49, no. 1, pp. 152–155, Jan 2013.

[2] IEEE, "Ieee recommended practice for the design of reliable industrial and commercial power systems," *IEEE Std 493-2007 (Revision of IEEE Std 493-1997)*, pp. 1–689, June 2007.

[3] J. Druant, F. De Belie, P. Sergeant, and J. Melkebeek, "Power flow in an induction machine based electrical variable transmission," 2016, pp. 1197–1202.

[4] J. Druant, T. Vyncke, F. D. Belie, P. Sergeant, and J. Melkebeek, "Adding inverter fault detection to model-based predictive control for flying-capacitor inverters," *IEEE Transactions on Industrial Electronics*, vol. 62, no. 4, pp. 2054–2063, April 2015.

[5] S. Kouro, P. Cortes, R. Vargas, U. Ammann, and J. Rodriguez, "Model predictive control 2014;a simple and powerful method to control power converters," *IEEE Transactions on Industrial Electronics*, vol. 56, no. 6, pp. 1826–1838, June 2009.

[6] F. D. Belie, E. D. Brabandere, J. Druant, P. Sergeant, and J. Melkebeek, "Model based predictive torque control of an electric variable transmission for hybrid electric vehicles," June 2016, pp. 1203–1207.

[7] J. Melkebeek, *Dynamics of Electrical Machines and Drives*. University of Ghent, 2016.

[8] J. Druant, H. Vansompel, F. De Belie, J. Melkebeek, and P. Sergeant, "Torque analysis on a double rotor electrical variable transmission with hybrid excitation," *IEEE Transactions on Industrial Electronics*, 2016.

[9] J. Druant, H. Vansompel, F. De Belie, and P. Sergeant, "Optimal control for a hybrid excited dual mechanical port electric machine," *IEEE TRANSACTIONS on energy conversion*, 2017.

[10] J. O. Estima and A. J. M. Cardoso, "Impact of inverter faults in the overall performance of permanent magnet synchronous motor drives," in *2009 IEEE International Electric Machines and Drives Conference*, May 2009, pp. 1319–1325.

Contents

List of Figures

List of Tables

List of Abbreviations and Symbols

Abbreviations

2L-VSI Two Level Voltage Source Inverter

EMF ElectroMotive Force

EV Electric Vehicles

FS-MPC Finite Set Model Based Predictive Control

HEV Hybrid Electrical Vehicles

ICE Internal Combustion Engine

IGBT Insulated Gate Bipolar Transistor

IM Induction Machine

MA Moving Average

PD Partial Discharge

PM Permanent Magnet

SM Synschonous Machine

Nomenclature

Chapter 1

Introduction

Using energy resources carefully is more and more a compelling responsibility. Our generation is confronted with various new challenges concerning energy and the environment. Energy savings are a topical subject. On the one hand due to economic reasons, on the other, due to environmental and sustainability reasons. These are rooted in the gradual exhaustion of classical energy resources and special raw materials, but also in the need for a reduction in carbon dioxide emissions. From industry it is expected to work with materials in a sustainable and cost-effective manner and to undertake serious efforts in carbon dioxide emissions. This policy is underpinned by different organizations and European guidelines.

One way to achieve energy savings, is to increase the energy efficiency of an industry plant. An Electrical Variable Transmission (EVT) can be used to replace subsystems with a combination of mechanical (electrical machines, flywheels, loads,...) and electrical ports (DC-bus, batteries, supercapacitor). In an EVT, energy is transferred in an electromechanical way. There is no mechanical contact between the mechanical input and output port of this system. The latter is the main reason for the increased efficiency. Also, the possibility exists to transfer/deliver electrical energy from/to the output. This not only results in a higher efficiency, but also in a reduction in the number of components, by combining for example a gearbox and an electrical machine.

However, industry is not the main cause of air pollution. The transportation sector plays a major role here as well. Car manufacturers undertake high efforts to reduce the exhaust gasses of traditional vehicles. Though, last year scandals were encountered concerning emission control during laboratory emission testing. Just think about *Dieselgate*. It seems like exhaust reductions for traditional cars have reached their limits. Therefore Hybrid Electrical Vehicles (HEV) and Electrical Vehicles (EV) receive more and more attention, with a slight preference for an HEV. This due to the limited driving range of an EV. HEV is a combination of both. It still contains an Internal Combustion Engine (ICE), as well as, battery which is also able to deliver energy to the wheels. Here, an EVT can also be used. It can replace the planetary gear set and two electrical machines in Hybrid Electrical Vehicles (HEV's) [32]. In this way, a complete decoupling of the ICE and the wheels is possible. The ICE can thus work in its optimal state, minimizing for example the fuel consumption.

In both applications, the user wants the system to be reliable. More and more attention is paid to this, especially in industry. The break down of a machine results in downtime witch is also

translated into decreased earnings. If a spare one is available, this downtime can be minimized. Though an entire production unit can be out of operation for hours [2]. Furthermore an extra cost is added for the new electrical machine. In this throwaway society and the pressure to reduce the downtime, it may occur that the entire system is replaced while a minor repair can solve the problem. If the user knows what is wrong with the electrical system, this can reduce the down-time and the extra cost. To do this, a fault-diagnosis system can be useful. As an extension, if possible, the system should activate a fault tolerant operation mode. The latter is certainly important for the application in an HEV. hazardous situations can be avoided. Think about the consequences of a breakdown of an EVT, when driving on a high-way. This will be the subject of this thesis.

Chapter 2

Faults in Electrical Machines

2.1 Overview

As indicated in the introduction, the user wants the system to be reliable. Though, different faults can exist in an electrical machine. In this chapter, an overview will be given and also how, some of them, can be detected. An overview is shown in figure 2.1. This classification is cause-based. Faults in electrical machines can be largely divided into 2 groups, i.e. external and internal faults. External faults occur due to causes from outside of the machine itself. Three main causes can be distinguished: electrical, mechanical and environmental faults. Internal faults originate from inside the machine. These faults are further subdivided into three types: electrical, mechanical and magnetic faults. Since every type of electrical machine has some symmetry in it's design, these faults will induce a distortion in the air gap field [1]. This will affect the performance and lifespan of the machine.

The chance of occurrence of each fault is different. This can be seen from statistical studies. A first study by IEEE standard dating from 1983 shows the most common faults and their statistic occurrences for different types of machines, see table 2.1. From this it can be seen that mechanical faults appear the most, 43.68 %, as cause for a failure of an electrical machine. A second important part are winding faults, occurring 25.5 % of all failures.

Table 2.1: 1983 IEEE survey on the reliability of large motors (> 200 hp). The number of failures for each fault-type [2].

Failed component	Induction motor	Synchronous motor	Wound rotor motor	DC motor	All types
Bearing fault	152	2	10	2	166
Winding fault	75	16	6	-	97
Rotor fault	8	1	4	-	13
Shaft or coupling	19	6	-	-	19
brushes or sliprings	N.A.	7	8	2	16
External Devices	10	9	-	2	18
Not specified	40	9	-	2	51
Total	304	41	29	6	380

Figure 2.1: Faults in electrical machines [1]

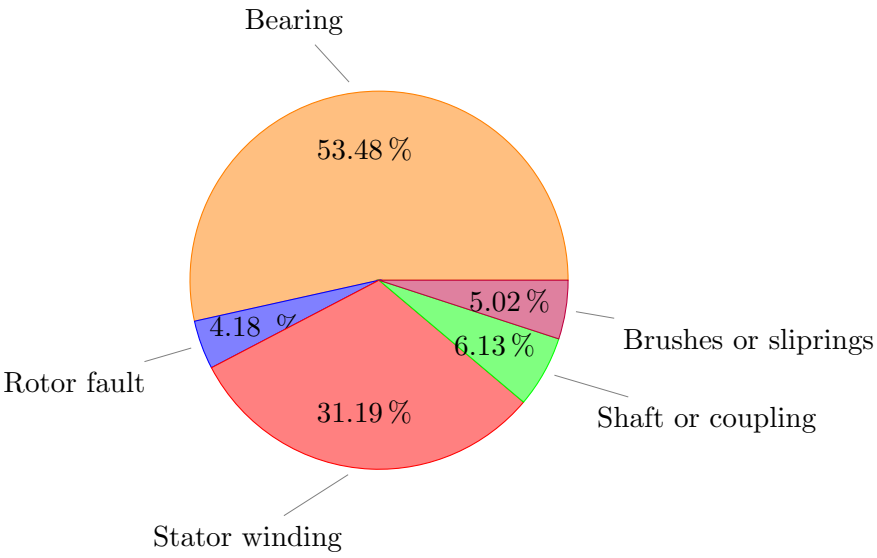

Figure 2.2: Extrapolated distribution of internal faults in electrical motors (based on [2])

More recent studies [11, 12] show similar results. Note that 13.4 % of the failures couldn't be identified. It is reasonable to assume that these failures follow a similar distribution. If now only the internal faults are considered, the relative percentage of each fault is shown in figure 2.2. From this it can be seen that bearing faults and stator winding faults are the most common. Since the EVT used in this master dissertation, basically behaves like a Permanent Magnet Synchronous Machine (PM-SM), faults specific for this type will be emphasised. For example, rotor faults are described as a bar breakage in Induction Machines (IM) while for PM-SM, rotor faults are referred to as demagnetizing faults. in no way the intention of this text to give a complete overview of all possible causes and consequences of faults.

2.2 Internal faults

2.2.1 Electrical faults

This type of fault is common for every electrical machine. For the PM-EVT, two types are distinguished: the breakdown of sliprings and winding faults. In classic electrical machines, thee latter fault-type is the second most common cause of error. Since this type of EVT has 2 wounded electrical parts, the occurrence of a winding fault is more likely to happen. It is therefore instructive to investigate the possibility to detect these different types of winding faults exist, see figure 2.3.

Each fault will have a different effect on the operation performance of the electrical system. They are largely subdivided into two classes: the fatal and damaging ones. Obviously, fatal faults are those for which the machine cannot continue operating. Phase-to-phase an coil-to-ground faults are included in this group. These faults both lead to a large increase in the current. An external circuit breaker should react as fast as possible, in order to protect the electrical system itself and its environment, e.g. prevent the start of a fire.

The other faults, i.e. turn-to-turn faults, open-circuit and coil-to-coil faults will affect the

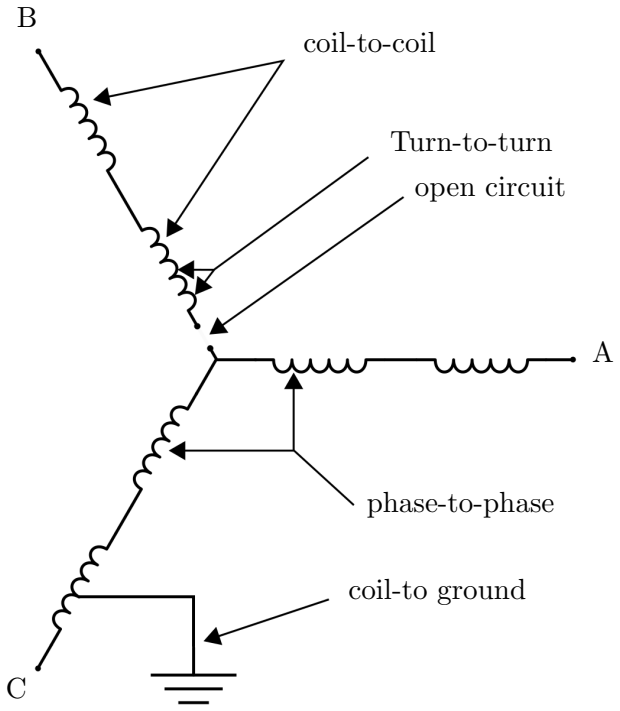

Figure 2.3: Winding faults in electric machines [3].

performance of the electrical machine, but the machine can still operate. An open-circuit, so called *single phasing*, is mostly due to a poor power connection, e.g. at the motor terminals, or the blow-up of one of the fuses protecting the motor [13]. The cause of this problem is hardly ever coming from inside the electrical machine. Therefore it will be discussed in the next section.

Coil-to-coil and turn-to-turn faults are so called *Insulation faults*. They can be caused due to several reasons [14]:

1. A high ambient temperature inside the machine
2. Contamination due to oil, moisture,...
3. Starting conditions
4. ...

Recently, another cause has arisen for this fault-type. These days, variable frequency drives are commonly used in industry. These drives use devices with a very fast rise time and thus also voltage peaks [15, 16]. These short rise times can give an inhomogeneous voltage distribution along the windings. Due to the large voltage difference between these turns, the phenomenon *Partial Discharge (PD)* may occur. This is explained in figure 2.4

PD is referred to as "*an electrical pulse or discharge in a gas-filled void or on a dielectric surface of a solid or liquid insulation system*" [4]. If now the voltage difference between both turns is very high, it may occur that a discharge occurs between both windings. This is the case, especially when a number of voids are present within the insulation or between the copper and insulation. This lowers the breakdown voltage of the insulation. Naturally this results in a decreased life time of the insulation or even a failure.

When a turn-to-turn fault exist, it may propagate rapidly because of the larger current in the

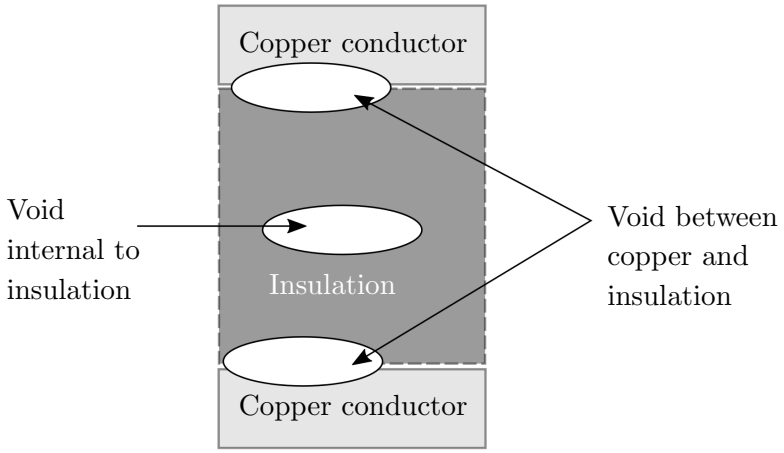

Figure 2.4: Principle of PD [4]

shorted winding. This can result in a localized heating and affect the health of the entire machine [17]. After some time, the machine will breakdown, see figure 2.5. Detecting this fault in an early stage of the machine, can save a lot of money. Not only can the motor be repaired by just replacing the affected winding in the machine, also the downtime of the machine is reduced significantly. Several techniques already exist to detect these fault-types.

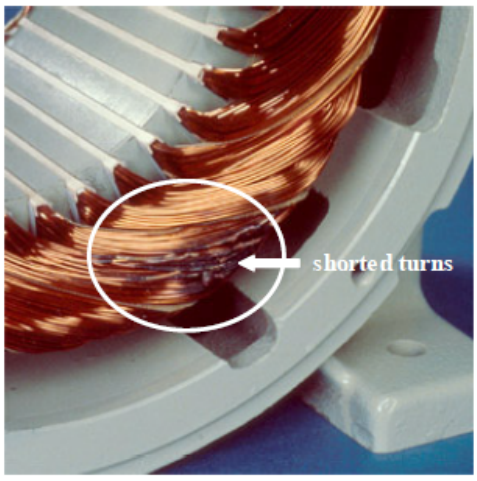

Figure 2.5: Result of a turn-to-turn fault[5].

Turn-to-turn faults result in an asymmetry. This asymmetry can be detected by analysing the symmetrical components of the current in the electrical system. Though, in my opinion this is not a very reliable detection method since there are different causes from which a negative sequence component can originate, e.g. from an unbalanced voltage supply. However, the presence of a negative sequence current is a signal that something is wrong in the system. Therefore it is valuable to analyse these components.

Secondly these faults can also be detected by analysing currents in the frequency domain [18]. Asymmetry in a machine will result in reverse rotating magnetic fields, as well as rotating fields with a different speed. By analysing the Fourier spectrum it is possible to detect a winding fault. Again, this detection method is not always reliable, since the use of an inverter automatically results in different harmonics [19]. This makes it difficult to detect a pattern. However, the

presence of an inverse field is a reason to decide that something is wrong.

Thirdly, the presence of a turn-to-turn fault can be diagnosed, by detecting the occurrence of a PD. This can be done by using a high pass filter and an electromagnetic sensor [20] and is proven to be a valid solution to detect a PD-discharge, which may be an indication that a turn-to-turn fault occurred. In order to be able to execute an online detection, the sensor must be placed permanently on the stator surface. The high pass filter is used to eliminate the noise originating from electrical interference [17].

Finally, these faults can also be detected model based [5]. The affected phase is split into two parts, the healthy and shorted proportion. In a healthy PM-SM, analysing the behaviour in a qd-reference frame is very simple. This due to the symmetrical built-up of every electrical machine. When modelling a turn-to-turn fault, the system becomes asymmetrical. Applying the Clarke and Park transformations [21], will now result in equations varying, not only in time, but also in the instantaneous angle of the rotor. This makes it much more difficult to analyse the system in a qd-reference frame. Though very complex, it is possible to model these fault-types. For the PM-EVT, which has a far more complicated model compared to classical machines, a firs step will be to determine an accurate model in a healthy situation. Based on this model, the model can be extended with this specific fault-type.

2.2.2 Mechanical faults

The most common faults in electrical machines are the mechanical ones. For a PM-EVT, bearing faults and eccentricity faults are very dangerous since this machine contains two rotors. This can result in an increase in the chance of occurrence of these faults. As many other faults, initially, no damage is brought to the machine. But, if nothing is done, these faults will propagate in time and result in a complete failure of the electrical machine. Therefore it is valuable to install an early-detection mechanism, such that the user can be informed about this issue. This can result in a lot of resource savings and a reduction in downtime.

Even in normal operation and a perfect design of a machine, the failure of bearing due to fatigue may occur. Note that in a machine the mechanical parts are almost always the first ones to fail. The reason for this is that the bearings are the only rotating parts having a physical contact. It is therefore only logical that these occur first [22]. Bearing faults can have different causes [14]:

1. Bad lubrication
2. Vibrations
3. Contamination and Corrosion
4. Misalignment

Bearing faults can result in an eccentricity fault as well. These two faults are thus closely related. Regardless of the cause of the bearing failure, these faults generate additional vibrations. By analysing these vibrations it is possible to detect this fault-type. Note that the real challenge for detecting these faults, is to distinguish the vibration components based on their origin. Mostly these faults are detected based on the Fast Fourier Transform (FFT) of the acceleration measurements [23]. Note that other, more efficient, methods are described in literature [23, 24].

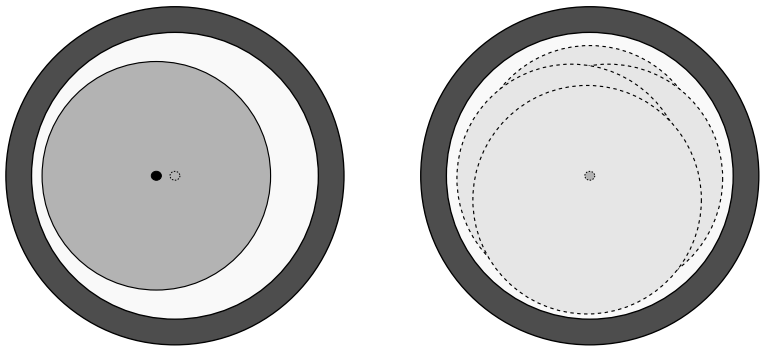

Figure 2.6: Eccentricity faults. Left: static eccentricity, right dynamic eccentricity

As mentioned above, bearing faults and eccentricity faults are closely related to each other. Eccentricity faults can be caused by [25]:

1. The bending of a shaft. This may occur due to a failure at the load itself.

2. Incorrect alignment. Though, this is referred to as an external fault, see figure 2.1, it still has the same result.

3. Bearing faults

4. Mechanical stresses from outside the machine.

These faults have impact on the air gap field. Different types of eccentricity are distinguished, see figure 2.6. Static eccentricity is referred to as a misalignment of the rotors rotation pin [1]. This type is mostly caused by a misalignment of the rotor itself. Dynamic eccentricity, to the contrary, is the kind of eccentricity causing the rotor centre to move, meaning that the rotation point is moving. This latter causes the air gap to change continuously. It's obvious that it is much easier to detect a static eccentricity in comparison to the detection of a dynamic eccentricity. In reality, it is mostly a mix of both.

It is already stated that eccentricity will cause an asymmetrical air-gap field. By making an estimate of the air gap field over time, it is possible to detect eccentricity, as well as a demagnetizing fault. This can be done based on the measurement of the current and rotational speed of the motor. In order to make an estimate of the air gap field, an accurate model is required. In [26], it is opted to detect air gap eccentricity based on the saturation level of the stator yoke. This method has been proven to be very accurate. There is on drawback, this method requires detailed FEM-calculations. Therefore the detection system has to be recalculated for a different machine.

The detection of eccentricity is also possible based on a motor current signature analysis [27]. Although this method has been proven to be valid, there are again some drawbacks to be mentioned. First, as mentioned above, the presence of certain frequency components in the current, can tell the user that something is wrong. Though an identification of the cause of this problem is not possible. Secondly, the system must operate under steady state conditions. For some applications, such as an HEV, this is major drawback.

2.2.3 Magnetic faults

The last type of internal fault that will be discussed are demagnetizing faults. There are multiple causes for a demagnetization of the PM's [28]:

1. A high starting torque. High starting torques mostly result in high currents as well. These high currents can cause a demagnetization.
2. High temperatures. When a high ambient temperature is present in the machine itself, the possibility exists that a demagnetization occurs. This temperature, so called *curie temperature*, is depending on the type of material that is used as a magnet [29].
3. Centrifugal forces can cause the PM's to fail. This breakdown will also result in a partial demagnetization.

Once a magnet is partially demagnetized, an asymmetric PM-field will be present in the air gap. This will result in a vicious circle resulting in a demagnetization of all the other PM's as well. Two types of demagnetization are distinguished. Symmetrical and asymmetrical demagnetization. The first type is referred to as a uniform partial demagnetization of all the PM's. When only one PM gets partially demagnetized, the second type is considered. Obviously the first type is much easier to detect.

Different methods exist to detect these fault-types. The first one is again based on the Fourier spectrum of the measured currents. The same drawbacks as before can be mentioned here. Also, the presence of a certain frequency component depends on the configuration of the stator windings, the detection must be redesigned for different winding configurations. Secondly, a PM-demagnetization can be detected by monitoring the back-EMF of a system [30]. Again based on a Fourier spectral analysis a detection is possible. An estimation of the back-EMF requires an accurate model.

2.3 External faults

2.3.1 Single phasing

As stated before, single phasing is the phenomenon where one of the three supply lines gets disconnected and no current flows trough this winding. The cause of this fault is mostly originating from outside the system, e.g. bad power connections. A detection of this fault-type is fairly easy since the disconnection of phase will result in zero current in one of the phases. It is therefore easy to detect this. Also, if one phase drops out, a pulsating torque will be created and the machine will slow down fast. In this way there is also a visual detection. Though an operation is still possible. This has been studied in literature [13].

2.3.2 AC driver Faults

Last, AC driver faults will be discussed. Altough these faults are not directly related to the the electrical machine itself, they are common in industry. Even a basic 2-level Voltage Source Inverter (2L-VSI) is already complex and thus very susceptible to suffer critical failures [31].

This can affect the driver performance and thus also have an impact on the electrical system connected to it. These faults are categorized in two classes:

1. Short-circuit faults. In an inverter-leg of a 2L-VSI, two IGBT's are present. It is absolutely not allowed to close both IGBT's at once. This would result in a short-circuit of the DC-bus. This always leads to a breakdown of the inverter itself. These faults may occur when the driver of an IGBT is not operating correctly or the IGBT itself doesn't want to turn off any more. In this case, an external device should detect this short-circuit current and decouple the inverter from the DC-bus.
2. Open-circuit faults. This fault is described as follows. When the IGBT is in an off-state and gets a gate pulse, the device doesn't react. These faults are far less dangerous for both the device and the DC-bus. The machine is still able to operate. A fault-detection system has been derived for a three-level flying-capacitor inverter [8]. This detection principle is model based.

2.4 Conclusion

In this chapter an overview is given of the different faults in electrical machines. Although these faults are described for PM-SM in general, they are also present in a PM-SM. Different detection methods exist for these faults. An overview is given in table 2.2.

Table 2.2: Overview of possible detection techniques

	Bearing	Stator windings	Demagnet-ization	Air-gap Eccentricity	Inverter faults
Fourier spectrum current	+-	+-	+-	+-	+-
Vibration analysis	x			x	
Partial Discharge		x			
model based		x	x	x	x

In an ideal situation, it is possible to detect faults based on the FFT of the current components. However, these fault situations can result in the same frequency component, such that, the controller can only sense that something is wrong. But, for some situations, it can not determine what the cause of the problem is. The detection of a turn-to-turn fault based on PD-detection, has proven to be very useful. Remark that an extra sensor is needed here. Vibration analysis is also useful to detect eccentricity and bearing faults. Similar to the PD-detection, this method also requires extra measurement equipment. last, a model based detection method has been described. A model based detection method only requires current and speed measurements. These are already used to control a PM-EVT. This method is proven to be useful for almost every fault situation. From this it is clear that this method is the most promising one. It has been shown that, in order to be able to execute a reliable model based detection of failures in machines, an accurate model is required. This will be the first subject of this master dissertation.

Chapter 3

The Electrical Variable Transmission

3.1 Introduction

In the previous chapter, it has been shown that a model based fault detection requires an accurate model, this will be the subject of this chapter. A PM-EVT will be described and modelled. This type is considered in this master dissertation since it tends to be the most effective in Hybrid Electrical Vehicles [34]. It has a higher power density and variable flux linkage. Also it is the type used in the experimental setup in the lab. Other types of an EVT exist (e.g. an Induction Machine based EVT [7, 35, 36]) and have been analysed in literature .

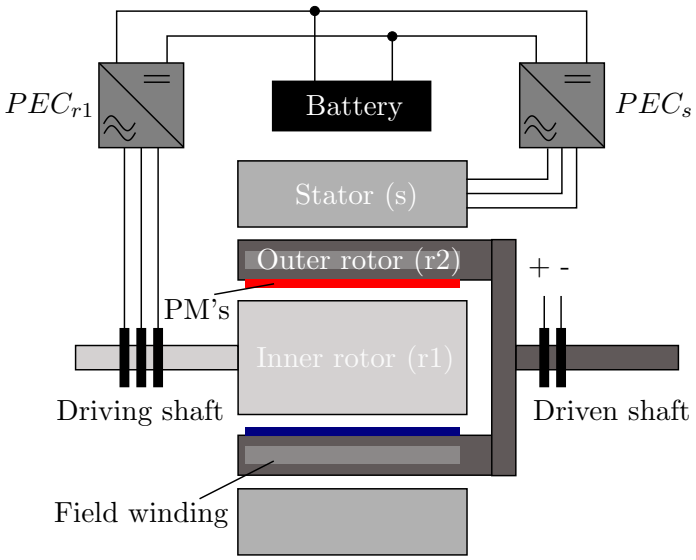

Figure 3.1: Schematic of a single layer permanent magnet EVT with DC-field winding [6]

3.2 General Description

Figure 3.1 highlights the main components of a PM-EVT. It is described first by M. J. Hoeijmakers [37]. Every EVT consists of a stator, an inner rotor and outer rotor. For this specific type, the outer rotor is layered with PM's at the inner diameter. At the outer diameter a field winding is present. The latter can be used to influence the coupled flux between the stator and outer rotor. This winding is electrically accessible trough sliprings. The three phase windings of the inner rotor and stator are accessible in a similar way. Other types of PM-EVT's exist and are described in literature [38]. These will not be considered here. The stator and inner rotor windings are each connected to a separate Power Electronic Converter (PEC). The DC-side of both PEC's is connected to a common battery.

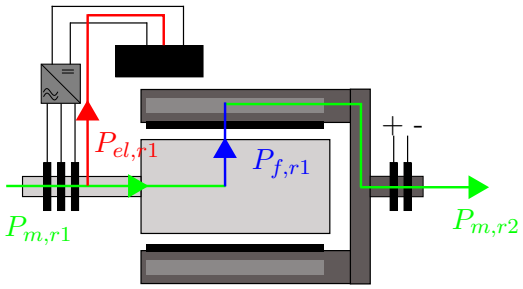

Figure 3.2: Power flows in the subsystem inner and outer rotor ($\Omega_{r1} > \Omega_{r2}$)

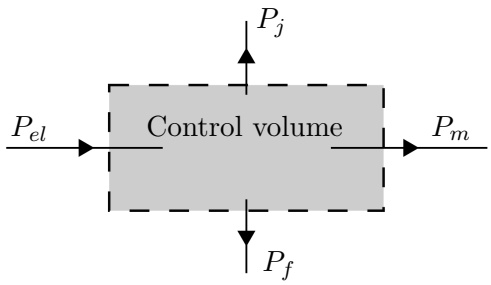

Figure 3.3: Motoring convention power flows reference directions [7]

As stated in the introduction of this chapter, an EVT is an efficient and dynamic electromechanical converter. To understand this, consider only the inner and outer rotor. Suppose that the inner rotor is fixed. Sending an AC-current trough the windings of the inner rotor creates a rotating field. Classic machine theory shows that the outer rotor will start rotating [39]. This is nothing more then a PM-SM. Only now the rotating part is at the outer diameter of the machine. The transmission of torque occurs in an electromagnetic way [40]. It is the result of the interaction between the rotating field created by the current flowing in the inner rotor and the field originating from the PM's on the outer rotor.

If now the inner rotor is driven by , e.g. a ICE, this rotor will rotate as well. Mechanical power will be supplied to inner rotor

$$P_{m,r1} = \Omega_{r1} T_{r1} \tag{3.1}$$

where Ω_{r1} is the angular velocity of the inner rotor and T_{r1} the mechanical torque supplied by the driving element. The basic operation principle of this electrical system didn't change. By sending an appropriate current trough the three phase windings of the inner rotor, the torque delivered on the driving shift will be transferred to the driven shaft, see figure 3.2. This transfer occurs in an electromagnetic way trough the air gap magnetic field. This transferred power is called the field power P_f. For now assume that the electrical power $P_{el,r1}$ is delivered by a battery. If this machine is assumed to be lossless, Newton's third law states that the torque delivered on the driving shaft T_{r1} will be the same torque T_{r2} on the driven shaft. Using the

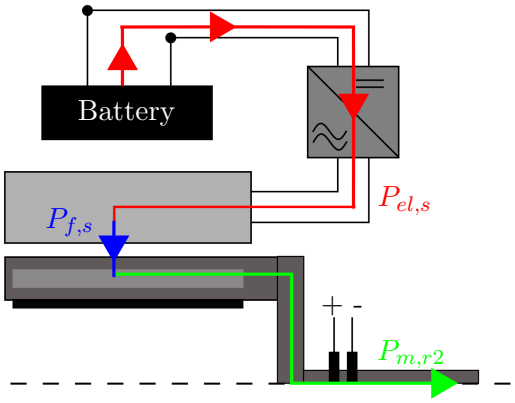

Figure 3.4: Power flows in the subsystem stator and inner rotor

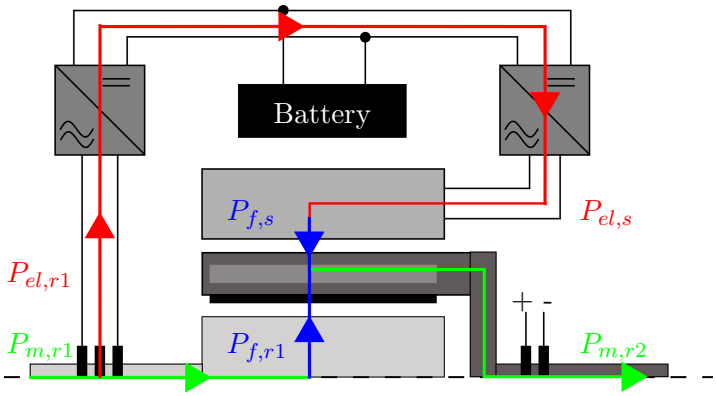

Figure 3.5: Power flows in the EVT operating as a CVT ($\Omega_{r1} > \Omega_{r2}$)

motoring-convention (see figure 3.3), with the control volume being both rotors, conservation of energy states that

$$\begin{aligned} P_{m,r2} &= T_{r2}\Omega_{r2} \\ &= -P_{m,r1} + P_{el,r1} \\ &= -T_{r1}\Omega_{r1} + P_{el,r1} \end{aligned} \tag{3.2}$$

The input and output mechanical speed are denoted by respectively Ω_{r1} and Ω_{r2}. The power flow is shown in figure 3.2. Each colour represents a different type of power flow. The red, green and blue path denote respectively the electrical, mechanical and field power flow. Note that the torque T_{r1} delivered to the inner rotor (driving shaft) must be negative. The direction of $P_{el,r1}$ depends on the speed difference between both rotor, see figure 3.2. By sending an appropriate current to the inner rotor, the energy transfer between both rotors can be controlled. Note that the joule losses P_j are not present here, since the machine is assumed to be lossless.

Until now, the described electrical system is nothing more then a Continuous Variable Transmission (CVT) though more efficient then other types of CVT's in certain operations points [40]. Note that this is not an exact definition of a CVT since some electrical power must be added.

The main advantage of the EVT lies within the ability to split power. To clarify this, only consider the stator and outer rotor. This subsystem is a conventional PM-SM, see figure 3.4. Applying again the laws of energy conservation, respecting the convention depicted in figure 3.3, results in:

$$P_{el,s} = 3V_{f,s}I_{f,s}cos(\phi_s) = P_{m,r2} = T_{r2}\Omega_{r2} = -T_s\Omega_{r2} \tag{3.3}$$

If now the previously described electrical systems are combined, the original machine shown in figure 3.1 is obtained. Yet, the power transmission between each subsystem didn't change. The total torque at the outer rotor T_{r2} is now the sum of those delivered by the inner rotor T_{r1} and the stator T_s.

$$T_{r2} = -(T_s + T_{r1}) \tag{3.4}$$

By changing the amplitude and frequency of the current delivered to the stator, torque on the driven shaft can be changed while keeping the torque T_{r1} delivered by the driving element constant. Since there is no mechanical contact between both rotors, the speed of both rotors can be changed continuously. Note that when the speed of the outer rotor changes while the speed of the inner rotor is kept constant, the current supplied to the inner rotor must change if the torque delivered to the outer rotor must be kept constant. Combining the results derived above, with the control volume being the whole EVT (exclusion of the battery and PEC's), conservation of energy states the total electrical power must equal the total mechanical power.

$$\begin{aligned} P_{el,r1} + P_{el,s} &= P_{m,r1} + P_{m,r2} \\ &= T_{r1}\Omega_{r1} + T_{r2}\Omega_{r2} \end{aligned} \tag{3.5}$$

Pending on the operation condition, the electric power on the stator and inner rotor can be positive and negative. Since both electrical windings are connected by a PEC, the EVT can operate without a battery (CVT-mode). In that case the electrical power delivered to (leaving) the stator must be opposite to the power leaving (delivered to) the inner rotor, see figure 3.5. Equation 3.5 now simplifies to:

$$T_{r2} \cdot \Omega_{r2} = -T_{r1} \cdot \Omega_{r1} \tag{3.6}$$

In reality a loss therm needs to be added. The losses however are now completely different from a conventional CVT. The main contributions are copper losses in the windings, iron losses and magnet losses due to eddy currents in the magnets. Equation 3.6 can also be written as

$$-T_{r2} \cdot \Omega_{r2} = T_{r1} \cdot \Omega_{r2} + T_{r1}(\Omega_{r1} - \Omega_{r2}) \tag{3.7}$$

Comparing this with equation 3.2, shows that the electrical power delivered to the inner rotor now originates from the speed difference between both rotors. In the case of figure 3.5, the speed of the inner rotor Ω_{r1} must be bigger then the speed of the outer rotor Ω_{r2} in order for the power flows to be correct.

If now the battery is added, the electrical power delivered to the stator en inner rotor is not restricted. This explains how the power split works. The EVT can work in different modes (Electrical, Hybrid,...) as will be explained in sequel of this chapter.

Until now, nothing is mentioned about the fied winding present in the outer rotor. It has been proven in literature that the PM-flux linkage is strongly coupled with the inner rotor [6, 41], see figure 3.6. The stator flux linkage will be rather low and therefore only a small part of the electrical power delivered to the stator will be transferred to the outer rotor. This is not a problem in most applications since the required stator torque is low most of the time [42]. Keeping this flux-linkage low will result in a lower iron loss in the stator. To achieve this low flux-linkage, a flux bridge is present underneath the field winding ,see figure 3.6. By applying a DC-current to the field windings, the saturation-state of this flux bridge can be altered. The results is a higher flux-linkage between the outer rotor and the stator. This will be discussed extensively in 3.4.4.

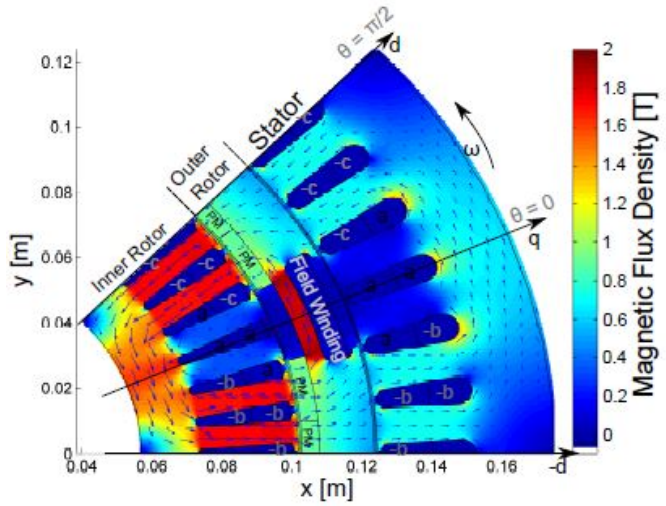

Figure 3.6: Cross sectional view of the EVT. All currents are zero. [6]

3.3 Operation modes

Operation modes are distinguished based on the power flow in the EVT itself. There are three main modes: electrical, mechanical and hybrid mode. The purely mechanical mode, namely the CVT-mode, has already been described above. The other two modes will be elaborated here.

3.3.1 Electrical mode

In a purely electrical mode, the inner rotor torque is zero. When the outer rotor is assumed to be at a physical standstill and no current can flow in the inner rotor windings, the operation is similar to a classic SM. This has already been described in section 3.2. In reality, some current will be applied to the inner rotor because of the presence of a rotating field originating from the stator and inner rotor. This will induce a negative torque on the driven shaft. For HEV's this is undesirable. A clutch between the ICE and EVT must be installed such that an negative inner rotor torque can be maintained [43].

3.3.2 Hybrid mode

In this mode, the inner rotor is driven to provide mechanical energy to the outer rotor. This mode is segmented based on the rotational speed and desired torque of both rotors. Some of these modes have already been described. An overview of is given in figure 3.8. The sign-convention for this PM-EVT is also shown in figure 3.9.

To explain these different modes, the machine is again assumed to be lossless. In the first quadrant, power is delivered to the outer rotor and the rotational speed Ω_{r2} is positive. In figure 3.8, the torque working on the inner rotor shaft is assumed to be negative, also the rotational speed of the inner rotor is taken to be positive. This is mostly the case in application for which the EVT is used. As an example, consider the application HEV's. In this case, the inner rotor

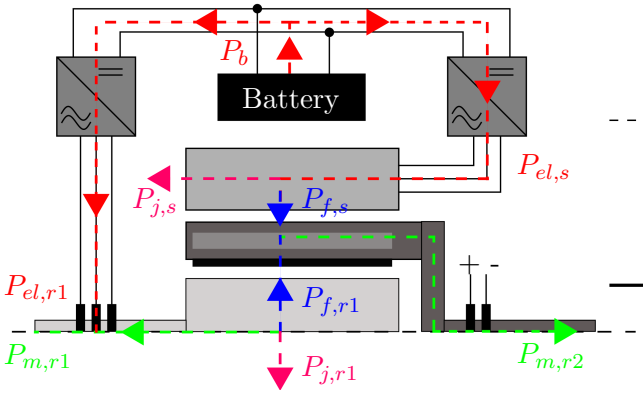

Figure 3.7: reference power flow based on the motoring convention 3.3

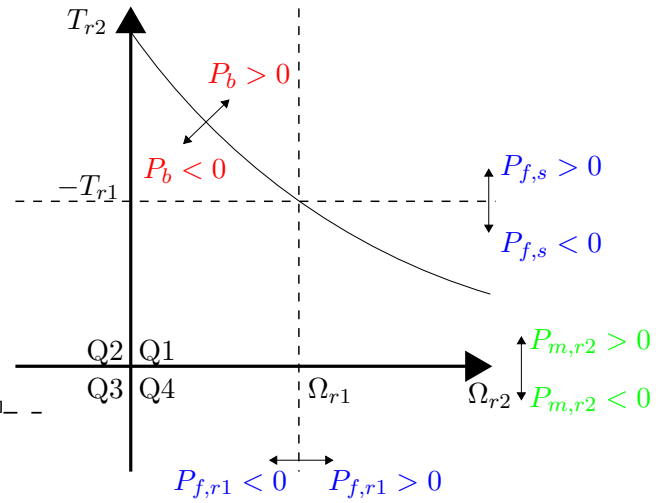

Figure 3.8: Power flow in hybrid mode, only for Q1 and Q4. [7]

is connected to an ICE. An ICE is made to rotate in one direction and deliver mechanical power such that the operation point of the inner rotor will always be situated in the first quadrant.

In hybrid mode, mechanical power at the inner rotor does not match the desired mechanical power at the outer rotor. To overcome this mismatch, the battery will be used. In general the power delivered by (stored in) the battery P_b can be written as follows:

$$P_b = P_{m2} + P_{m3} \tag{3.8}$$

So if the power delivered to the inner rotor is lower then the desired at the outer rotor, electrical power will leave the battery and vice versa. The line for which the battery power is zero, is indicated on figure 3.9. Due to losses, this line is shifted downwards since extra power is needed to overcome these losses. The electric power delivered by (stored in) the battery, is then split in two parts. One part energizes the inner rotor, while the other part energizes the stator.

$$P_b = P_{el,s} + P_{el,r1} \tag{3.9}$$

The sign of each electrical power depends on the operation point of the EVT. If the desired torque T_{r2} at the outer rotor is bigger then the torque $-T_{r1}$ delivered to the inner rotor. Then the electrical power supplied to the stator windings will be positive and vice versa, see equations 3.3 and 3.4. The electrical power delivered to the inner rotor is thus only depended on the torque difference between both rotors. This in contrast to the electrical power supplied to the inner rotor, which is depended on the speed difference between both rotors, see equation 3.2.

When the EVT operates in the fourth quadrant, the torque on the outer rotor is negative, as well as the mechanical power delivered by the outer rotor $P_{m,r2}$. In that case, a high amount of energy will be stored in the battery along the stator windings. Pending on the speed difference between both rotors, energy will also be delivered to the battery along the inner rotor windings.

A similar reasoning can be applied for the second and third quadrant. Only now, the mechancal speed at the outer rotor is reversed [7].

3.4 Modelling

The availability of a model is vital for a fault-detection system. A model for this type of EVT is derived based on the theory given in the course *Dynamics of Electrical Machines and Drives* [21]. In this section, the modelling will be limited to the EVT itself. It can be seen from figure 3.1 that other elements require modelling as well: the controller, the PEC's, the battery and the load. These will be threatened in another chapter.

3.4.1 Assumptions

In a first approach a number of assumptions must be made before it's possible to derive a model with workable machine equations. For the justification of these assumptions, please refer to this book [21].

- A three-phase symmetrical machine
- Sinusoidal distributed stator/inner rotor windings (no higher space harmonics of current layer, MMF or field)
- No skin-effects
- No saturation
- No slot-effects

3.4.2 Reference frames

Since both rotors can rotate at a different speed, multiple reference frames can be considered in this PM-EVT. Note that a three phase symmetrical winding is present in the stator and inner rotor. Compare this to the outer rotor wich is two phase symmetrical, see figure 3.6. To simplify the analysis of this system, some transformations must be applied. First the Clarke transformation must will be used to transform each group of three phase voltages and currents abc to the $\alpha\beta 0$-frame. The transformation matrices are given in equation 3.10.

$$\begin{bmatrix} F_\alpha \\ F_\beta \\ F_0 \end{bmatrix} = T_c \begin{bmatrix} F_a \\ F_b \\ F_c \end{bmatrix} = \frac{2}{3} \begin{bmatrix} 1 & \frac{-1}{2} & \frac{-1}{2} \\ 0 & \frac{\sqrt{3}}{2} & \frac{-\sqrt{3}}{2} \\ \frac{1}{2} & \frac{1}{2} & \frac{1}{2} \end{bmatrix} \tag{3.10a}$$

$$\begin{bmatrix} Fa \\ Fb \\ Fc \end{bmatrix} = T_c^{-1} \begin{bmatrix} F_\alpha \\ F_\beta \end{bmatrix} = \begin{bmatrix} 1 & 0 \\ -\frac{1}{2} & \frac{\sqrt{3}}{2} \\ -\frac{1}{2} & -\frac{\sqrt{3}}{2} \end{bmatrix} \begin{bmatrix} F_\alpha \\ F_\beta \end{bmatrix} \tag{3.10b}$$

Note that for the inverse transformation ($\alpha\beta 0 \rightarrow abc$), the zero sequence-component is left out. The zero-sequence component is the average of a three-phase group. Since in this system the

neutral is not connected the sum of currents in each group of three phase windings is always zero, see equation 3.11.

$$i_a(t) + i_b(t) + i_c(t) = 0 \tag{3.11}$$

This means that the zero-sequence current component can never exist. Although a zero-sequence voltage component can be present, no power will be associated with this voltage. Therefore it will have no impact on the electrical behaviour of this system. the result is a two phase representation.

The stator is at a physical standstill as well as the corresponding reference frame. The reference frame of each rotor is rotating with an (electrical) rotational speed $\omega_{r.}$. Note that the rotational speed of the reference frame is not equal to the mechanical rotational speed. To understand this reconsider figure 3.6. This is only 1/8th of the cross-sectional view of the EVT. The d- and q-axis are highlighted on this figure. These axes represent the reference frame of the outer rotor. The main-flux flows along the d-axis. Since the EVT considered in this thesis has N_p= 4 pole pairs and the machine must be symmetrical, the pulsation of the PM-field is equal to $\omega_{r2} = \Omega_{r2} N_p$ and thus 4 times faster then the mechanical speed of the outer rotor. A similar reasoning can be applied for the inner rotor.

By using the Park-transformation, $\alpha\beta$-components can be expressed in another reference frame rotating at a certain speed ω_b. This reference frame, also called the qd-reference frame, is chosen in such a way that the q-axis lags the d-axis [21]. The instantaneous angle of this reference frame is known at any time and is denoted by $\theta_b = \omega_b t$. The Park transformation is given by the following transformations.

$$\begin{bmatrix} F_q \\ F_d \end{bmatrix} = T_{park} \begin{bmatrix} F_\alpha \\ F_\beta \end{bmatrix} = \begin{bmatrix} cos(\theta_b) & sin(\theta_b) \\ -sin(\theta_b) & cos(\theta_b) \end{bmatrix} \begin{bmatrix} F_\alpha \\ F_\beta \end{bmatrix} \tag{3.12a}$$

$$\begin{bmatrix} F_\alpha \\ F_\beta \end{bmatrix} = T_{park}^{-1} \begin{bmatrix} F_q \\ F_d \end{bmatrix} = \begin{bmatrix} cos(\theta_b) & -sin(\theta_b) \\ sin(\theta_b) & cos(\theta_b) \end{bmatrix} \begin{bmatrix} F_q \\ F_d \end{bmatrix} \tag{3.12b}$$

The general transformations to a common reference frame at a rotational ω_b speed applied on both the stator and inner rotor are depicted in 3.9. For simplicity, the number of pole pairs is chosen equal to 1.

Several options for ω_b are possible. In this thesis the rotational speed of the common reference frame is chosen to be the pulsation ω_{r2} of the PM-field. This is the most obvious choice since the PM-flux isn't changing over time in that case. The same holds for the inductance matrix.

3.4.3 Basic model

In a first approach, respecting the assumptions made in section 3.4.1, a basic model is derived based on Faraday's and Ohm's law. For more detailed information concerning this derivation

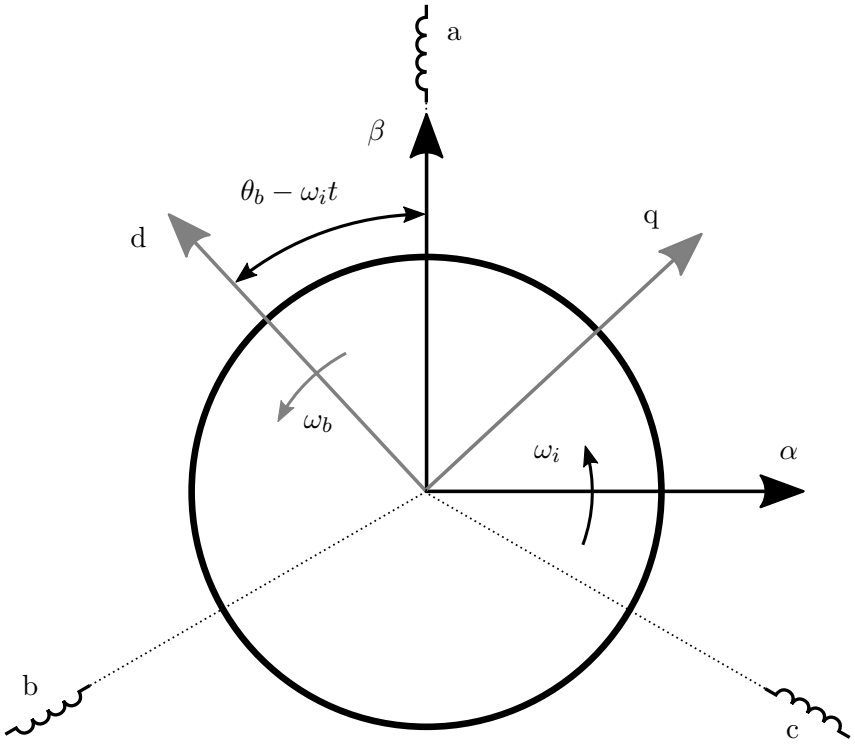

Figure 3.9: Reference frame: representation in general. ω_i is O for the stator reference frame and ω_{r1} for the inner rotor reference frame

refer to [21, 44].

$$\begin{cases} V_{s,q} = R_s I_{s,q} + p\Psi_{s,q} - \omega_{r2}\Psi_{s,d} \\ V_{s,d} = R_s I_{s,d} + p\Psi_{s,d} + \omega_{r2}\Psi_{s,q} \end{cases} \tag{3.13a}$$

$$\begin{cases} V_{r1,q} = R_{r1} I_{r1,q} + p\Psi_{r1,q} - (\omega_{r2} - \omega_{r1})\Psi_{r1,d} \\ V_{r1,d} = R_{r1} I_{r1,d} + p\Psi_{r1,d} + (\omega_{r2} - \omega_{r1})\Psi_{r1,q} \end{cases} \tag{3.13b}$$

In both equations p denotes the Laplace operator. Since the outer rotor is composed of PM's, no equations exists for the inner rotor. Note that it is assumed that no dynamics are present in the field winding. This is only partially true. But since a current in the field windings only influences the flux-linkages in both equations, it can be omitted.

The flux-components used in equation 3.13 are influenced by several factors. This in contrast to the IM based EVT[10] where it is possible to determine *inductance parameters*. For a PM-EVT, there is no easy way modelling them. In a first approach, omitting cross-effects and saturation, each flux component in equation 3.13 can be written as a linear function with parameter the corresponding current.

$$\begin{cases} \Psi_{s,q} &= L_{s,q} I_{s,q} \\ \Psi_{s,d} &= L_{s,d} I_{s,d} + \Psi_{s,PM} \end{cases} \tag{3.14a}$$

$$\begin{cases} \Psi_{r1,q} &= L_{r1,q} I_{r1,q} \\ \Psi_{r1,d} &= L_{r1,d} I_{r1,d} + \Psi_{r1,PM} \end{cases} \tag{3.14b}$$

Using these findings, equations 3.13 can be simplified to:

$$\begin{cases} V_{s,q} = R_s I_{s,q} + pL_{s,q} I_{s,q} - \omega_{r2}(L_{s,d} I_{s,d} + \Psi_{s,PM}) \\ V_{s,d} = R_s I_{s,d} + pL_{s,d} I_{s,d} + \omega_{r2} L_{s,q} I_{s,q} \end{cases} \tag{3.15a}$$

$$\begin{cases} V_{r1,q} = R_{r1} I_{r1,q} + pL_{r1,q} I_{r1,q} - (\omega_{r2} - \omega_{r1})(L_{r1,d} I_{r1,d} + \Psi_{r1,PM}) \\ V_{r1,d} = R_{r1} I_{r1,d} + pL_{r1,d} I_{r1,d} + (\omega_{r2} - \omega_{r1}) L_{r1,q} I_{r1,q} \end{cases} \tag{3.15b}$$

The model described above is sufficient when a long-therm behaviour of the EVT needs to be examined. In the scope of this thesis where the possibility of fault-detection is investigated, a more sophisticated model is required.

3.4.4 Saturation and cross-effects

Before deriving a more detailed model, revisit the assumptions in paragraph 3.4.1. For this electrical machine, cross-effects are very important. For example, finite element calculations show that next to the q-axis inner rotor current $I_{r1,q}$, also the q-axis stator current $I_{s,q}$ has an influence on the flux-component $\Psi_{r1,q}$ [6]. These cross-effects will be included in the new model.

Until now, the effect of the current $I_{r2,d}$ in the field windings has been omitted as well. Note that $I_{r2,q}$ can not exist since only a DC-current can flow trough te field-winding, creating a field along the d-axis. Applying a negative DC-current to the field winding increases the flux coupling between the stator and outer rotor ($\Psi_{s,d}$ & $\Psi_{s,q}$). Obviously it will also haven an effect on the flux coupling between the inner and outer rotor ($\Psi_{r1,d}$ & $\Psi_{r1,q}$). These effects must be brought into account as well.

Last, in conventional electrical machines, saturation is neglected most of the time. But in order to have a accurate model of the real machine, it has to be included as well. From now on saturation, the effect of the field current and cross-effects will be taken into account. These effects will be discussed extensively in the next section.

Using FEM-calculations all flux-linkages were mapped as a function of different current components. This was done by my counsellor. Using predefined look-up tables it is possible to determine the flux-linkage based on all current components.

$$\Psi_{s/r1/r2,q/d} = f(I_{s,q}, I_{s,d}, I_{r2,d}, I_{r1,q}, I_{r1,d}) \tag{3.16}$$

The base for this model is still equation 3.13. Only now, the simplifications made in the previous section ,see equation 3.15, are not applicable any more. The derivative to time of each flux linkage component can be written as the sum of the product of the partial derivative to each variable

and the derivative to time of that variable.

$$\begin{bmatrix} \frac{d\Psi_{s,q}}{dt} \\ \frac{d\Psi_{s,d}}{dt} \\ \frac{d\Psi_{r2,d}}{dt} \\ \frac{d\Psi_{r1,q}}{dt} \\ \frac{d\Psi_{r1,d}}{dt} \end{bmatrix} = \begin{bmatrix} \frac{\partial\Psi_{s,q}}{\partial I_{s,q}} & \frac{\partial\Psi_{s,q}}{\partial I_{s,d}} & \frac{\partial\Psi_{s,q}}{\partial I_{r2,d}} & \frac{\partial\Psi_{s,q}}{\partial I_{r1,q}} & \frac{\partial\Psi_{s,q}}{\partial I_{r1,d}} \\ \frac{\partial\Psi_{s,d}}{\partial I_{s,q}} & \frac{\partial\Psi_{s,d}}{\partial I_{s,d}} & \frac{\partial\Psi_{s,d}}{\partial I_{r2,d}} & \frac{\partial\Psi_{s,d}}{\partial I_{r1,q}} & \frac{\partial\Psi_{s,d}}{\partial I_{r1,d}} \\ \frac{\partial\Psi_{r2,d}}{\partial I_{s,q}} & \frac{\partial\Psi_{r2,d}}{\partial I_{s,d}} & \frac{\partial\Psi_{r2,d}}{\partial I_{r2,d}} & \frac{\partial\Psi_{r2,d}}{\partial I_{r1,q}} & \frac{\partial\Psi_{r2,d}}{\partial I_{r1,d}} \\ \frac{\partial\Psi_{r1,q}}{\partial I_{s,q}} & \frac{\partial\Psi_{r1,q}}{\partial I_{s,d}} & \frac{\partial\Psi_{r1,q}}{\partial I_{r2,d}} & \frac{\partial\Psi_{r1,q}}{\partial I_{r1,q}} & \frac{\partial\Psi_{r1,q}}{\partial I_{r1,d}} \\ \frac{\partial\Psi_{r1,d}}{\partial I_{s,q}} & \frac{\partial\Psi_{r1,d}}{\partial I_{s,d}} & \frac{\partial\Psi_{r1,d}}{\partial I_{r2,d}} & \frac{\partial\Psi_{r1,d}}{\partial I_{r1,q}} & \frac{\partial\Psi_{r1,d}}{\partial I_{r1,d}} \end{bmatrix} \begin{bmatrix} \frac{dI_{s,q}}{dt} \\ \frac{dI_{s,d}}{dt} \\ \frac{dI_{r2,d}}{dt} \\ \frac{dI_{r1,q}}{dt} \\ \frac{dI_{r1,d}}{dt} \end{bmatrix} \tag{3.17}$$

Using this and taking into account that the derivative of the field current ($I_{r2,d}$) is known, equation 3.13 can be solved. This matrix with partial derivatives, the so called ***Jacobian***, can be derived easily from the given look-up tables. Combining this gives:

$$\begin{bmatrix} \frac{\partial\Psi_{s,q}}{\partial I_{s,q}} & \frac{\partial\Psi_{s,q}}{\partial I_{s,d}} & \frac{\partial\Psi_{s,q}}{\partial I_{r1,q}} & \frac{\partial\Psi_{s,q}}{\partial I_{r1,d}} \\ \frac{\partial\Psi_{s,d}}{\partial I_{s,q}} & \frac{\partial\Psi_{s,d}}{\partial I_{s,d}} & \frac{\partial\Psi_{s,d}}{\partial I_{r1,q}} & \frac{\partial\Psi_{s,d}}{\partial I_{r1,d}} \\ \frac{\partial\Psi_{r1,q}}{\partial I_{s,q}} & \frac{\partial\Psi_{r1,q}}{\partial I_{s,d}} & \frac{\partial\Psi_{r1,q}}{\partial I_{r1,q}} & \frac{\partial\Psi_{r1,q}}{\partial I_{r1,d}} \\ \frac{\partial\Psi_{r1,d}}{\partial I_{s,q}} & \frac{\partial\Psi_{r1,d}}{\partial I_{s,d}} & \frac{\partial\Psi_{r1,d}}{\partial I_{r1,q}} & \frac{\partial\Psi_{r1,d}}{\partial I_{r1,d}} \end{bmatrix} \begin{bmatrix} \frac{dI_{s,q}}{dt} \\ \frac{dI_{s,d}}{dt} \\ \frac{dI_{r1,q}}{dt} \\ \frac{dI_{r1,d}}{dt} \end{bmatrix} = \begin{bmatrix} V_{s,q} - R_s I_{s,q} + \omega_{r2}\Psi_{s,d} - \frac{\partial\Psi_{s,q}}{\partial I_{r2,d}}\frac{dI_{r2,d}}{dt} \\ V_{s,d} - R_s I_{s,d} - \omega_{r2}\Psi_{s,q} - \frac{\partial\Psi_{s,d}}{\partial I_{r2,d}}\frac{dI_{r2,d}}{dt} \\ V_{r1,q} - R_s I_{r1,q} + (\omega_{r2} - \omega_{r1})\Psi_{r1,d} - \frac{\partial\Psi_{r1,q}}{\partial I_{r2,d}}\frac{dI_{r2,d}}{dt} \\ V_{r1,d} - R_s I_{r1,d} - (\omega_{r2} - \omega_{r1})\Psi_{r1,q} - \frac{\partial\Psi_{r1,d}}{\partial I_{r2,d}}\frac{dI_{r2,d}}{dt} \end{bmatrix} \tag{3.18}$$

The model described in this section, is a good approximation of the real set-up. The resulting torque can be calculated based on the equations below [21]. It's is this inner rotor torque T_{r1} that is then subjected to the driving element, e.g. the combustion engine.

$$T_s = \frac{3}{2}N_p(\Psi_{s,d}I_{s,q} - \Psi_{s,q})i_{s,d}) \tag{3.19a}$$

$$T_{r1} = \frac{3}{2}N_p(\Psi_{r1,d}I_{r1,q} - \Psi_{r1,q})i_{r1,d}) \tag{3.19b}$$

$$T_{r2} = -(T_s + T_{r1}) \tag{3.19c}$$

3.4.5 Simulation

These equations can be solved easily in a simulation-environment. This differential model will be used during the sequel of this thesis. To ease the calculations in a Simulink-environment, this model is discretized using the Euler-approximation. With a specified sample time T_s, this model is solved based on the following expression:

$$I_{.,.}(t + T_s) = I_{.,.}(t) + \frac{I_{.,.}}{dt} \cdot T_s \tag{3.20}$$

Using the look-up tables, provided by my counsellor, and the discretization of equation 3.18, the system can be implemented in Simulink.

3.5 Flux-linkage

As stated in the previous section, each current component has a different impact on each flux component, see equation 3.17. In the next chapter, the model described above will be further simplified in order to determine the optimal controller model. The determination of this optimal controller model requires knowledge of the influence of each current on the flux-linkage. This will be elaborated first. To do this, FEM-calculations were executed by my counsellor. Every figure in this section is based on these calculation. This section is partially based on [6].

3.5.1 The stator magnetic field

The d-axis stator flux

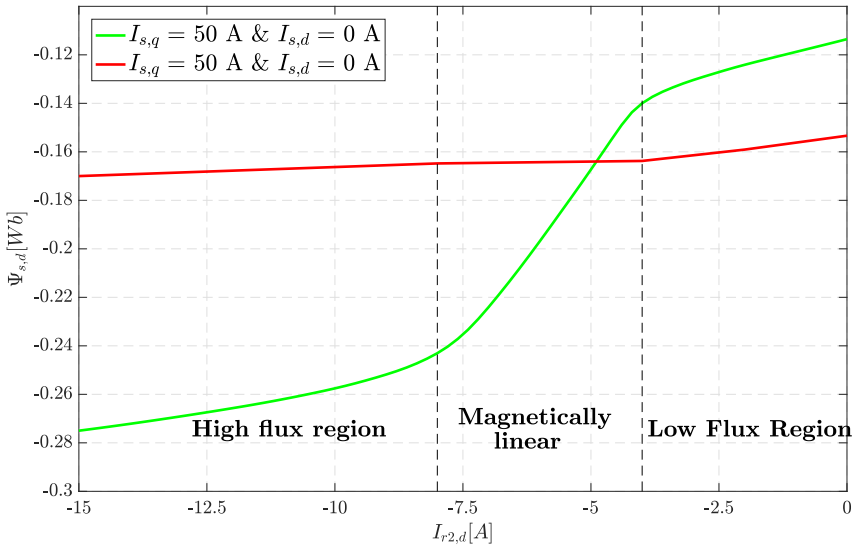

Figure 3.10: FEM-calculations: the stator d-axis flux $\Psi_{s,d}$ as a function of the field current $I_{r2,d}$

As described in the previous section, the stator flux linkage is low when no field current $I_{r2,d}$ is applied to the EVT. The PM-flux is highly coupled with the inner rotor. This is due to the flux bridge present beneath the field winding, see figure 3.6. In no load condition, the PM-field is the only field present in the system. Magnetic flux will always try to follow the path of least magnetic reluctance [29]. Since air has a high permeability, the magnetic reluctance of the air-gap will be high. The flux will thus avoid to flow trough the air-gap between the stator and other rotor. If only the PM-field is present, the flux bridge will be highly saturated, resulting in a much lower permeability and thus lower magnetic reluctance. Therefore, the flux will follow the path trough this bridge and the stator flux-linkage will be low. This can be seen in figure 3.10. The advantage is that the iron losses induced by the PM-field in the stator to be low. This region is called the low flux region. If now a DC-current flows through the field winding, the corresponding field will counteract the PM-field working on the flux bridge. From a certain

$I_{r2,d}$, the flux bridge will become magnetically linear resulting in very high permeability lowering the magnetic flux density in the flux bridge. The PM-flux path will change and the magnetic flux-linkage with the stator will be increased, see figure 3.11a. This causes more electrical power from the stator to be transferred to the outer rotor. A highly negative $I_{r2,d}$ will result again in

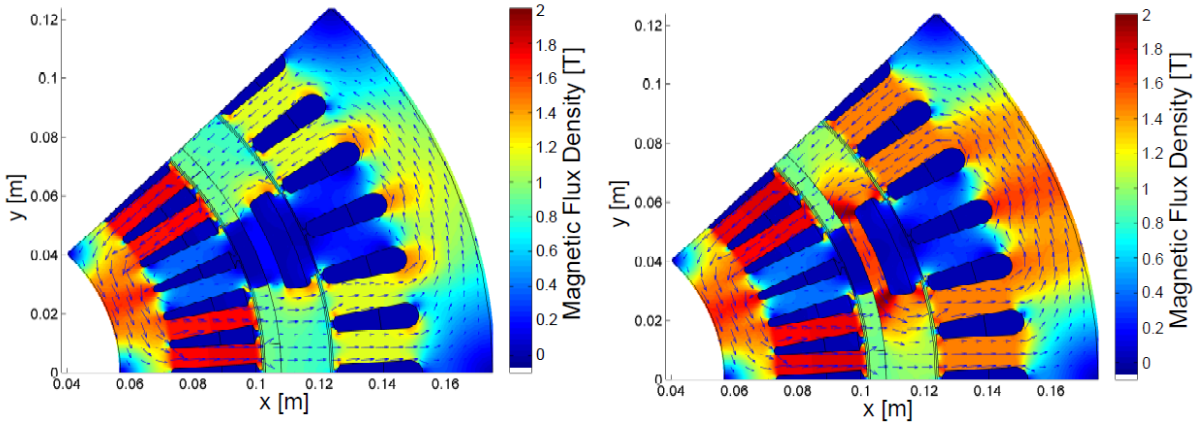

(a) $I_{r2,d}$=-6A (b) $I_{r2,d}$=-10A

Figure 3.11: Impact of the DC-field current on the flux linkage in the PM-EVT [6]

the saturation of the flux bridge. Only now, the flux will flow in the opposite direction trough the flux bridge, see figure 3.11b. Next to saturation of the flux bridge, also the stator yoke will become saturated when $I_{r2,d}$ is highly negative. This is due to the higher flux coupling with the stator. This region is called the high-flux region. On figure 3.10, the impact of $I_{r2,d}$ on the inner rotor flux-linkage is also shown. It can be seen that the impact is much lower.

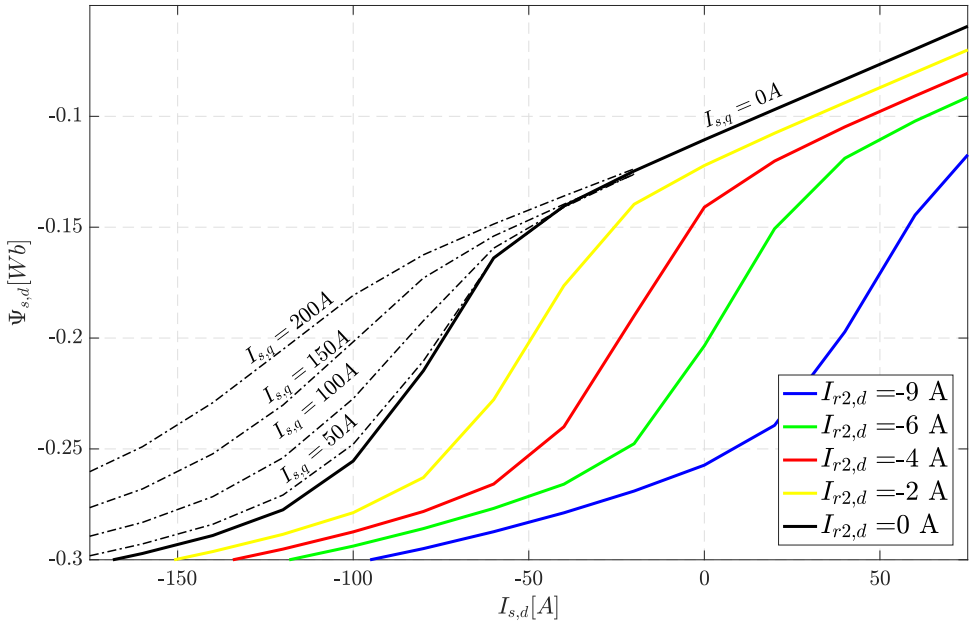

Figure 3.12: FEM-calculations: The d-axis stator flux $\Psi_{s,d}$ as a function of the stator d-axis current $I_{s,d}$ for different values of the field current $i_{r2,d}$

The d-axis stator flux $\Psi_{s,d}$ as a function of the d-axis stator current$I_{s,d}$ is shown in figure3.12. in no load, the magnetic coupling with the stator is maximal along the negative d-axis. This flux

originates from the PM's. Increasing $I_{s,d}$ will weaken $\Psi_{s,d}$. A negative $I_{s,d}$ will have the reverse effect. If the stator yoke and/or the flux bridge is saturated, then an increase of the d-axis stator current will not result in a high increase of the corresponding flux. The two saturation areas are characterized by this and visible in figure 3.12. By comparing figure 3.10 and 3.12, it can be noted that the effect of $I_{r2,d}$ and $I_{s,d}$ is very similar. These three areas are noticeable here as well.

In [6] it is derived that, for the magnetically linear part, the stator d-axis flux $\Psi_{s,d}$ can be referred to a equivalent stator d-axis current $I_{s,d,eq}$.

$$I_{s,d,eq} = I_{s,d} + 12.4 I_{r2,d} \tag{3.21}$$

This factor r=12.4 depends on the physical properties of the PM-EVT (the air gap width, the number of windings,...). Indeed, by looking at figure 3.12, shifting each graph with $12.4 I_{r2,d}$ means that each curve coincides. This is only an approximation for the saturated part of each equation, but it still gives a good comparison if this part is shifted with -0.003$I_{r2,d}$.

The influence of the stator q-axis current $I_{s,q}$ on the d-axis stator flux $\Psi_{s,d}$ is also shown in figure 3.12. For high $I_{s,q}$ the stator yoke will be saturated. The magnetically linear behaviour will thus mitigate for an increasing Is, q.

The influence of the q-axis inner rotor current $I_{r1,q}$ is almost completely negligible because both subsystems are separated by the PM's. The same holds for the d-axis inner rotor current$I_{r1,d}$. Yet, it has a similar effect on $\Psi_{s,d}$ as the stator d-axis current in both saturation areas. It has been shown in [6] that stator flux deviates only 2 % from the case where $I_{r1,d}$ is zero. These derivations are not solely based on the figures shown in this section. In appendix A.1 other graphs are depicted showing the influence of different current components.

The q-axis stator flux

Since the magnetic flux originating from the PM's flows along the d-axis, the q-axis stator flux is zero if no current is applied to the PM-EVT. From equation 3.19, it can be seen that increasing this current has a major contribution to the stator torque delivered to the outer rotor. This is due to the high proportion of the d-axis stator flux. Though, Increasing I_{sq} also means an increase of $\Psi_{s,q}$. This can be seen in figure 3.13.

From figure 3.13, it can be deduced that the influence of the d-axis stator current $I_{s,d}$ and field current $I_{r2,d}$ is negligible if $I_{s,d}$ is positive. A highly negative $I_{r2,d}$ causes saturation of the flux bridge in the other direction, see figure 3.11. Since a negative $I_{s,d}$ contributes to the flux-linkage between the stator and outer rotor, the stator yoke will be already saturated. Therefore an increase of the q-axis stator current will result in a smaller effect on $\Psi_{s,q}$.

Indeed, figure 3.14 shows that a negative d-axis stator current$I_{s,d}$ has an impact $\Psi_{s,q}$. This figure shows the impact of $I_{s,d}$ for different values of the field current $I_{r2,d}$. It can be seen that the q-axis stator flux can be described by the same equivalent d-axis stator current $I_{s,d,eq}$ used to calculated the d-axis stator flux $\Psi_{s,d}$. This can be derived physically by applying the same reasoning to determine equation 3.21, as described in [6]. Note that this only holds for the magnetically linear part but it is still a good approximation for the saturated areas.

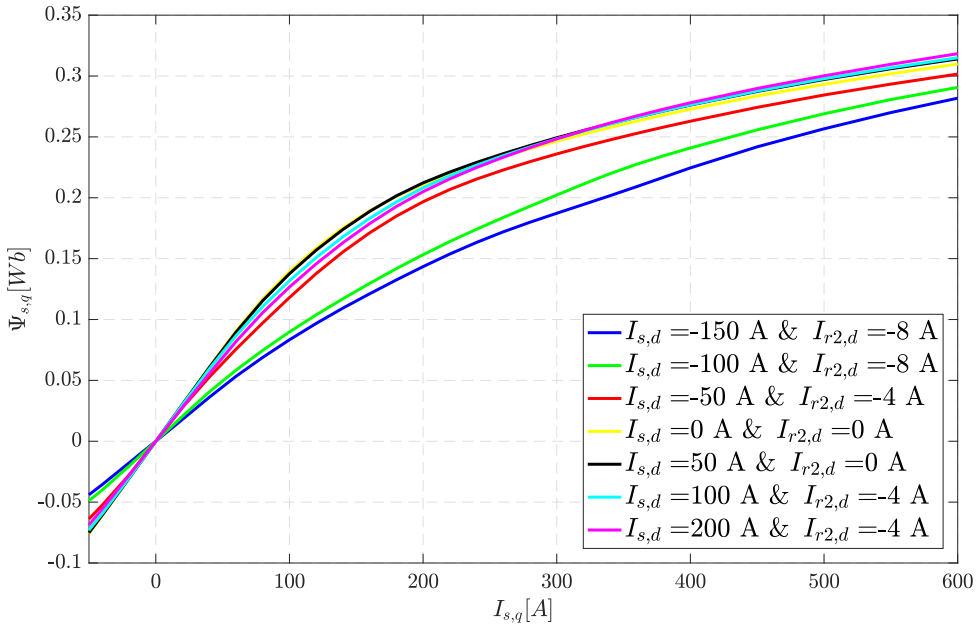

Figure 3.13: FEM-calculations: the q-axis stator flux $\Psi_{s,q}$ as a function of the q-axis stator current $I_{s,q}$ for different values of the d-axis stator current $I_{s,d}$ and the field current $I_{r2,d}$. Inner rotor current is zero.

In figure 3.14, the impact of $I_{s,d}$ on $\Psi_{s,q}$, for different values of $I_{s,q}$ and at a constant field current $I_{r2,d}$=-8 A, is also shown. Note that the effect of $I_{s,d}$ is stronger for higher $I_{s,q}$. This because, as mentioned before, a negative d-axis stator current $i_{s,d}$ causes the stator yoke to be saturated resulting in a lower q-axis stator flux $\Psi_{s,q}$.

The impact of the inner rotor current when the machine operates in hybrid mode, is smaller in comparison to the stator or field current. It is derived that a positive q-axis inner rotor current causes the flux to deviate maximum 10 % from the case where no current in the inner rotor is applied [6]. This is only the case for a few situation. Mostly the deviation due to the current $I_{r1,d}$ is smaller then 2% and thus negligible. As Will be seen in the next chapter, the $I_{r1,d}$ will be kept zero 4.4.2. The influence of this current is therefore of less importance in this master dissertation.

Some figures providing a base for the statements above, are not shown here. Please refer to appendix A.2 to view these figures. This is to keep this text clear for the reader.

3.5.2 The inner rotor magnetic field

The d-axis inner rotor flux

Since most of the MMF from the PM's is permanently coupled with the inner rotor, the inner rotor yoke will be already highly saturated. the impact of each current on the inner rotor flux is then much easier to describe. Figure 3.6 shows that flux-linkage between both rotors is maximal along the negative d-axis.

A negative $I_{r1,d}$ will increase the flux-linkage between both rotors, see figure 3.15. Due to the fact

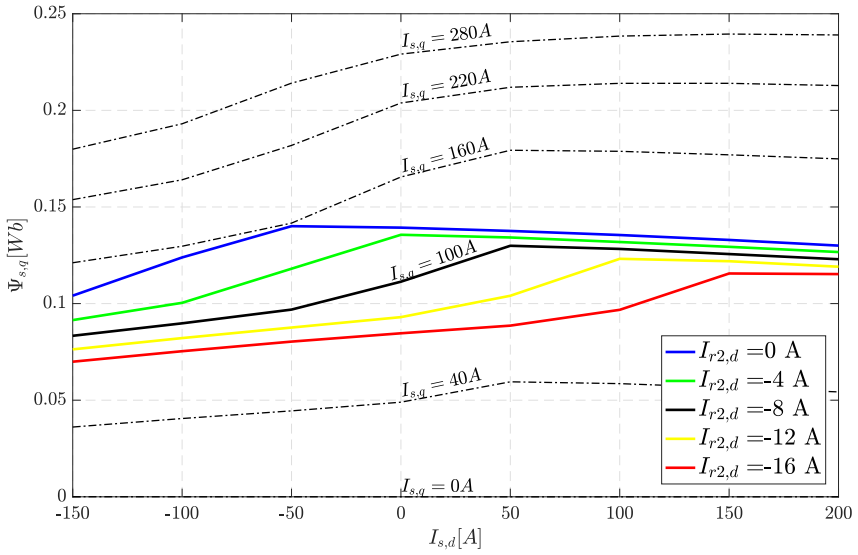

Figure 3.14: FEM calculations: the q-axis stator current $\Psi_{s,q}$ as a function of the d-axis stator current $I_{s,d}$ for different values of the field current $I_{r2,d}$

that the inner rotor is already saturated, the impact of $I_{r1,d}$ is the same in the whole operation area. the impact of the related q-axis current $I_{r1,q}$ is small. This again due to saturation of the inner rotor yoke. Note that the sign of $I_{r1,q}$ doesn't influence the impact on $\Psi_{r1,d}$. This due to the symmetrical construction of the machine.

From the previous section it is known that the field current $I_{r2,d}$ has an effect on the flux coupling between the stator and outer rotor. It has also been shown that a negative field current increases the flux linkage between both rotors, see figure 3.10. Figure 3.16 shows the impact of the d-axis stator current $I_{s,d}$. Again, different areas can be distinguished. A positive d-axis stator current $I_{s,d}$ causes flux-weakening. Therefore the inner rotor yoke will desaturated such that the magnetic reluctance increases. A negative $I_{s,d}$ causes the stator and inner rotor yoke to be more saturated, such that the impact is then almost negligible [6]. Note that the impact of both the field current $I_{r2,d}$ and d-axis stator current $I_{s,d}$ can be described, again, by using the same equivalent d-axis stator current $I_{s,d,eq}$, see equation 3.21. These derivations are based on multiple figures. Please refer to A.3.

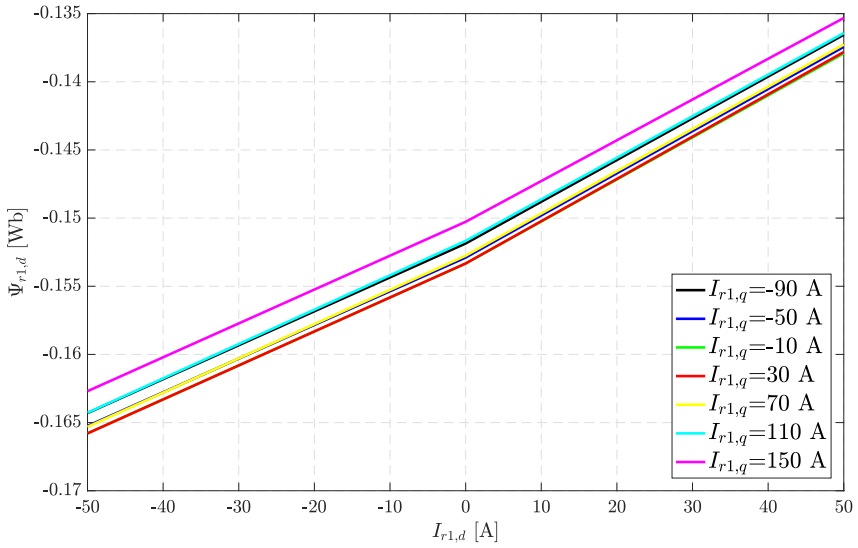

Figure 3.15: FEM calculations: the d-axis inner rotor flux $\Psi_{r1,d}$ as function of the d-axis inner rotor current $I_{r1,d}$ with parameter: the q-axis inner rotor current $I_{r1,q}$

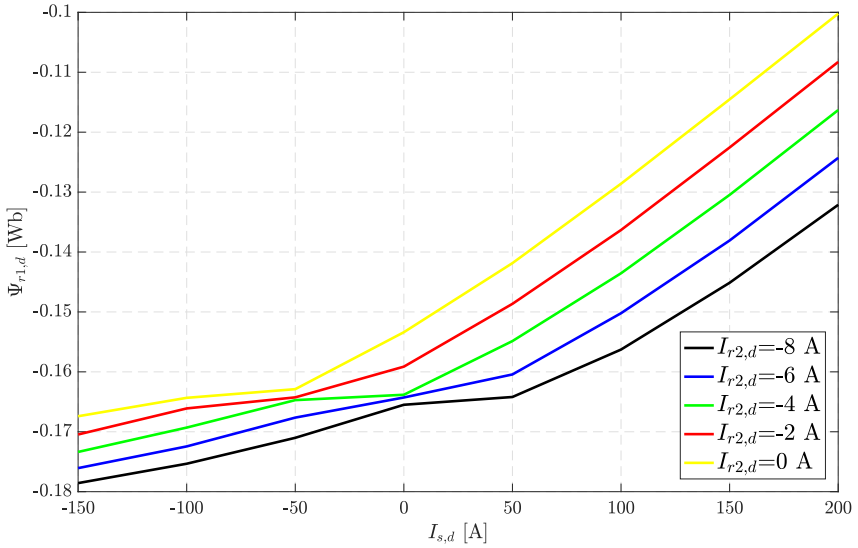

Figure 3.16: FEM calculations: the d-axis inner rotor flux $\Psi_{r1,d}$ as function of the d-axis stator current $I_{r1,d}$ with parameter: the field current $I_{r2,d}$. No current is applied to the inner rotor

The q-axis inner rotor flux

Last, the impact of different currents on the q-axis inner rotor flux $\Psi_{r1,q}$ will be elaborated.As previously stated, the inner rotor yoke is saturated due to the permanent flux linkage between both rotors. This causes the impact of the q-axis inner rotor current $I_{r1,q}$ to be constant, see figure 3.17. As expected, the influence of a small inner rotor d-axis current $I_{s,d}$is negligible due to high saturation of the inner rotor yoke.

A second important impact on $\Psi_{r1,q}$ is the q-axis stator current $I_{s,q}$. This is important when the machine is in a hybrid mode. The impact of $I_{s,q}$ is shown in figure 3.18. For high $I_{s,q}$ a, though small, impact can be noticed. Note that the effect change slightly for different values of

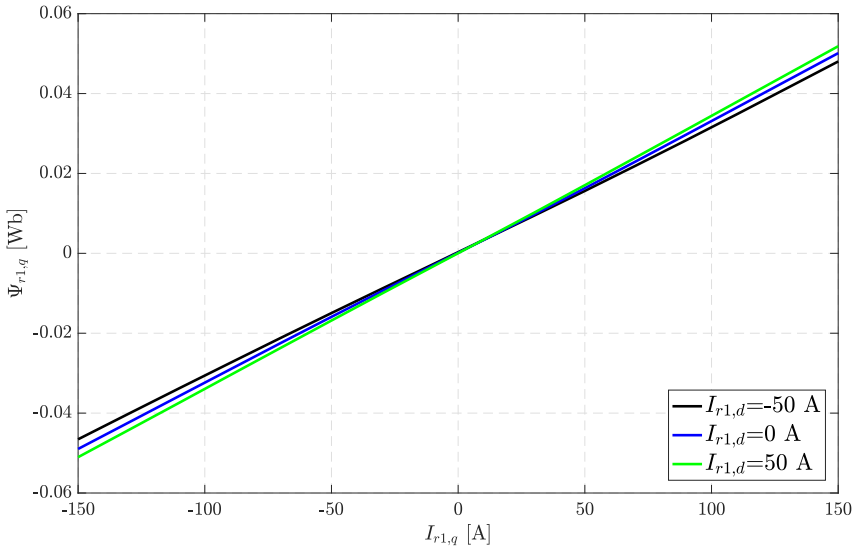

Figure 3.17: FEM calculations: the q-axis inner rotor flux $\Psi_{r1,q}$ as function of the q-axis inner rotor current $I_{r1,q}$ with parameter: the d-axis inner rotor current $I_{r1,d}$. No current is applied to the stator.

$I_{s,d}$ and thus also $I_{r2,d}$. A negative $I_{s,d}$ results in a stronger coupling between stator and outer rotor. This cause a higher saturation of the stator yoke such that $I_{s,q}$ will have almost no effect on $\Psi_{r1,q}$. From the moment that $I_{s,q}$ becomes very high, an impact can be noticed.

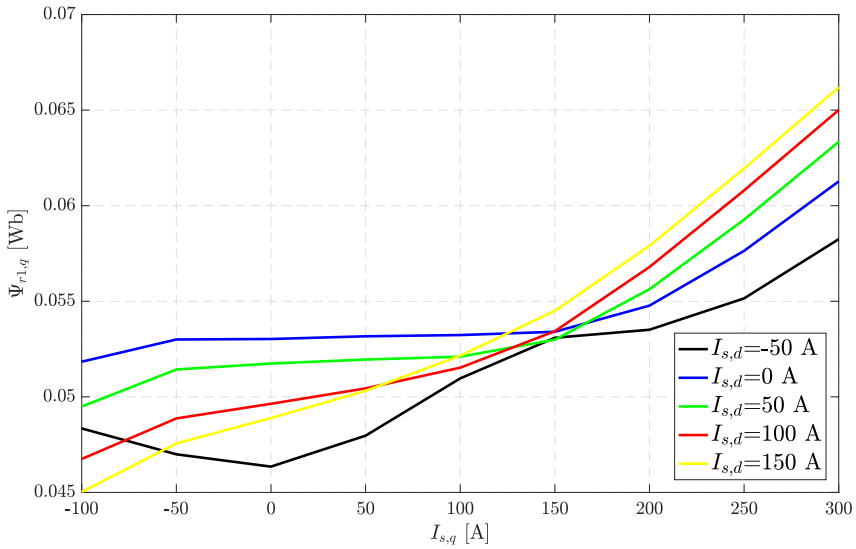

Figure 3.18: FEM calculations: the q-axis inner rotor flux $\Psi_{r1,q}$ as function of the q-axis stator current $I_{s,q}$ with parameter: the d-axis stator current $I_{s,d}$.The inner rotor q-axis current equals 150 A and the field current $I_{r2,d}$ equals -6 A.

Although the q-axis flux-linkage is low, the corresponding current determines the torque that will be transferred between both rotors. The effect of the other current components on $\Psi_{r1,q}$ is small. For more information concerning the impact of each current component on the q-axis inner rotor flux $\Psi_{s,q}$, please refer to A.4.

Chapter 4

Control Design

4.1 How to control?

The model described in the previous section can be controlled in various ways. Mostly, the user is only interested in the torque transfer to and speed at the output shaft. If an EVT is used in HEV, car manufacturers are interested in the rotational speed at the input shaft as well. This speed determines what e.g. the fuel consumption of the ICE will be at a certain wanted torque level [45, 43]. It is clear from the previous chapter that the value of current and flux is the key to control these parameters, see equation 3.19. Since the instant flux is determined by the type of PM's and the currents, see equation 3.16, controlling solely the current is sufficient. To do so, the switching states of the IGBT's, in both power electronic converters, are controlled. Also since there is no easy way measuring the flux, only the estimation of each flux component can be controlled. Look-up tables can be used for this. It is however more reliable to control something which is actually measurable.

An overview of the control principle is shown in figure 4.1. In this thesis, Finite set Model Predictive Control (FS-MPC) is used to control the currents in stator and inner rotor (r1). Based on speed and current measurements together with additional information of the complete electrical set-up, the controller must predict the best optimal switch configuration S_{stator} & S_{R1}. This is set on the IGBT's at a certain frequency. Using Field Oriented Control[35] or predefined mappings [9], torque set-points can be translated into a reference value. This for each current in the qd-reference frame of the stator and inner rotor. The system set-up, shown in figure 4.1, will be explained in this chapter. Note that a chopper is used to control the field-current in the outer rotor (R2). This will not be controlled here. A separate controller exists to do this.

As stated above, MPC requires a model. The model described in section 3.4.4 can't be implemented due to practical reasons. MPC requires a high-speed calculation device. A Field Programmable Gate Array (FPGA) is able to do this. The model described in section 3.4.4 requires a recursive interpolation-method because of the used discrete mappings of the flux (see equation 3.16). This slows the system enormously, making it impossible to implement this in practice. Simplifications will have to be made. Note other ways exist to control a current. A simple PI-controller should be sufficient as well. A comparison will be made in the next chapter.

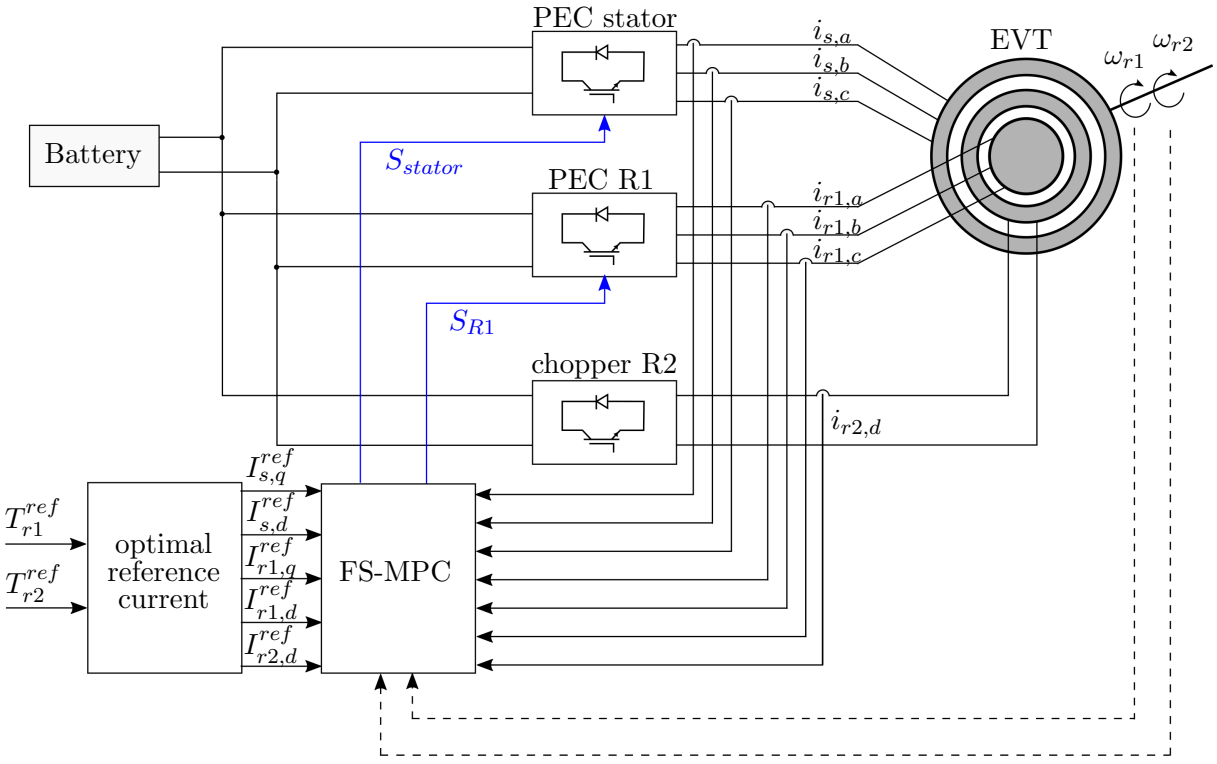

Figure 4.1: Control system overview

4.2 The Electrical set-up

The electrical set-up currently used, is shown in figure 4.2. Two basic two-level Voltage Source Inverters (2L-VSI) are used to feed the three phase windings of the stator and inner rotor.

Every inverter has three legs containing 2 IGBT's, each with an freewheel diode. One IGBT connects the output to the positive DC-bus($S_{y,x}$) and the other ($\overline{S}_{y,x}$) to the negative DC-bus, $x \in a, b, c$ & $y \in s, r1$. These switches work in a complementary way and determine the output of each leg. In the current set-up, the windings of the stator and inner rotor are in a star configuration. The output voltage of each leg is referred relative to the neutral clamp of the DC-bus. This point n, is shown on figure 4.2. The voltage between the outcome of one leg and this point is called the output phase voltage. In case $S_{y,x} = 1$ conducts (and thus $\overline{S}_{y,x} = 0$ not) the output phase voltage is one half of the positive DC-bus voltage. Vice versa, when $\overline{S}_{y,x} = 1$ conducts (and $S_{y,x} = 0$ is reverse biased), the output phase voltage is one half of the negative DC-bus voltage. For each leg there are 2 possibilities:

$$v_{y,xn} = -(\frac{1}{2} - S_{y,x})V_{dc} \qquad S_{y,x} \in [0, 1] \tag{4.1}$$

The IGBT's in one leg of an inverter must work in a complementary way. If this is not the case, the DC-bus would be short-circuited. This can destroy the battery and IGBT's completely. Therefore there must be some time between the complementary switching states.

To keep the currents in that stator and rotor at a certain reference values, the optimal switch-configuration is determined at a frequency of 10 kHz. This assures that the short-circuit condition will not occur.

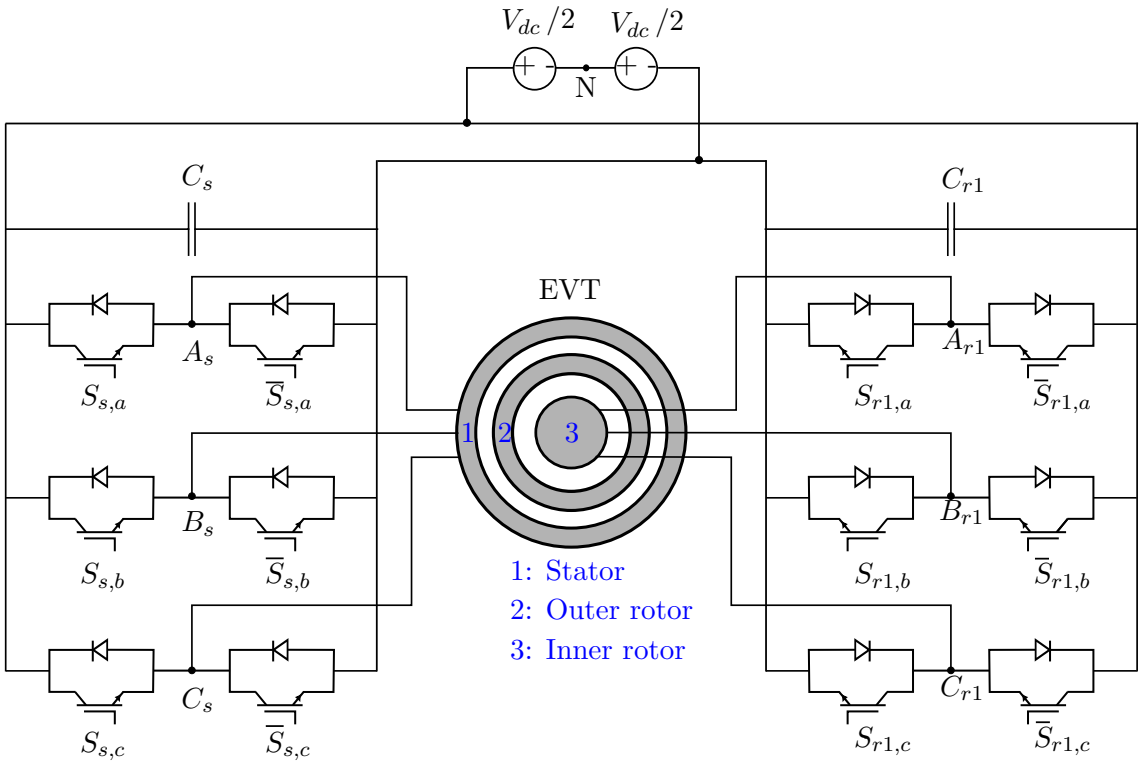

Figure 4.2: Setup of the inverters feeding the EVT.

Since for each leg 2 states are possible, one inverter has $2^3 = 8$ possible switch configurations. taking into account that there are 2 inverters, the total number of possible switch configurations becomes $8 \cdot 8 = 64$. Each configuration of a PEC can be translated into a space vector in the $\alpha\beta$-frame (see figure 4.3). The two vectors situated in the origin, represent the state where each leg is connected to the same DC-bus (positive or negative). In this case, the system applies only a zero sequence voltage to the machine, which has no active contribution to the creation of a rotating field in the EVT. These two vectors are called the *passive vectors*. the six remaining ones are called *active vectors*.

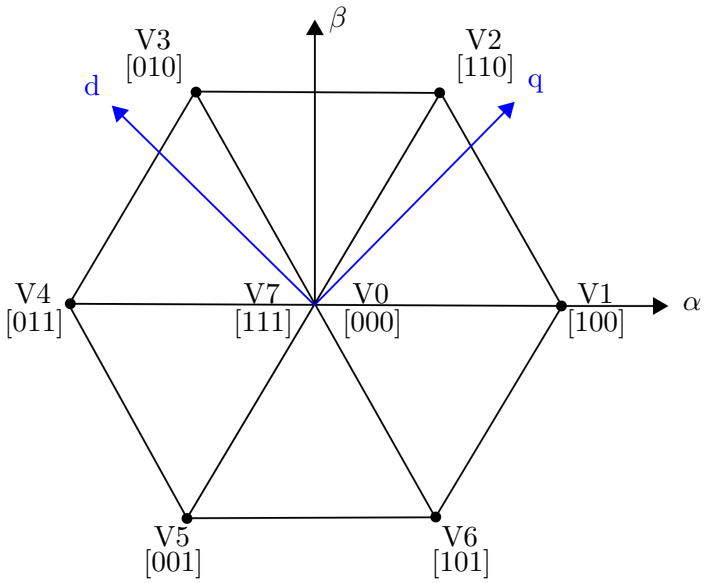

Figure 4.3: Space vector representation 2L-VSI [8]

Since the EVT is described in the qd-reference frame of the outer rotor, each vector must be rotated. The determination of the instantaneous position of this frame is based on rotational speed measurements of each rotor. The speed of this system, the pulsation of ω_{r2} of the PM-field, can be very high. The maximal outer rotor speed is 6000 rpm, resulting in a pulsation of 2513.27 rad/s. Since the switching frequency is set to 10 kHz, the outer rotor will rotate 4% of one revolution during each period. This must be taken into account when designing the controller

4.3 Implementation

In order to determine the optimal controller model, the whole electrical system must be implemented in a simulation environment, Simulink. The way in which the machine model described in the previous chapter will be implemented, has already been elaborated. The 2L-VSI must also be implemented. This can be done easily using expression 4.1. No dynamics of the inverter are concerned here. To model these 2L-VSI, some assumptions were made [10].

- The switching action occurs immediately
- No losses are concerned within the inverter
- The IGBT's are assumed to be ideal, so no parasitic capacitance or inductance.
- There is no voltage drop over the IGBT's or freewheel diodes
- No EMC-disturbances

Though this is a major simplification of reality, these assumptions can be justified since the switching-frequency of the IGBT's is chosen to be rather low, 10kHz. In that case, some extra time, so called dead time has been preserved for the switching actions to take place.

4.4 Torque vs. current

4.4.1 Field Oriented Control

In this master dissertation, two ways to determine the optimal reference values of the stator and inner rotor currents in the qd-frame will be discussed. In this reference frame all currents are DC-currents. The first one is called *Field oriented control (FOC)*. This section is based on the findings described in [35, 21]. The aim of FOC is to obtain a highly dynamic torque control.

In the previous chapter, the torque is written as function of four variables, see equation 3.19. In principle each of these variables can be chosen freely to obtain the desired values of the torque. For this PM-EVT, the PM-flux is oriented along the negative d-axis, see figure 3.6. This makes the q-axis flux almost zero. By varying only the q-axis current in the stator and inner rotor and keeping the d-axis current zero, the torque equations, see equation 3.19 are simplified.

$$\begin{cases} T_s = \frac{3}{2} N_p I_{s,q} \Psi_{s,d} \\ T_{r1} = \frac{3}{2} N_p I_{r1,q} \Psi_{r1,d} \end{cases} \tag{4.2}$$

The desired stator and inner rotor torque is thus only depended on three currents: the q-axis currents and the field-winding current$I_{r2,d}$. this latter current is not present in the equations above, but is has already been explained that a negative $i_{r2,d}$ increases the stator flux-linkage. Since there are only two equations, this system cannot be solved. $I_{r2,d}$ could be kept zero, but this would result in an inefficient operation. However, based on FEM-calculations it is possible to determine what the field current should be in order to minimize the copper and iron losses. In this way it is possible to solve this system. Though, it has been proven in literature that by keeping the d-axis current in the stator zero, no optimal minimization of copper and iron losses can be achieved [9]. Other ways exists, as will be explained in the next section.

4.4.2 Optimal Control

Field oriented control is an effective method to control the torque and speed of a motor [21]. It is however not the most energy efficient method. For this EVT, five current can be used to obtain a wanted stator and inner rotor torque. The global power managements system, determining the reference current values, can thus choose multiple combinations to obtain the same torque. In [9], an optimal control method is derived such that the controller can choose the optimal reference current vector $\boldsymbol{I^*}$, minimizing the total active power losses P_{loss}. This is also verified experimentally.

$$\begin{aligned} \boldsymbol{I^*} &= [I^*_{s,q}, I^*_{s,d}, I^*_{r2,d}, I^*_{r1,q}, I^*_{r1,d}] \\ &= argmin(P_{loss}(\boldsymbol{I}, \omega_{r1}, \omega_{r2})) \end{aligned} \tag{4.3}$$

such that:

$$\begin{aligned} T_s(\boldsymbol{I^*}) &= T_s^{set} \\ T_{r1}(\boldsymbol{I^*}) &= T_{r1}^{set} \end{aligned} \tag{4.4}$$

The total loss in active power, P_{loss} is a combination of copper losses P_{Cu} and iron losses P_{Fe} in the PM-EVT. Both terms are depended on the currents $\boldsymbol{I}$ and the speed of both rotors ω_{r1} & ω_{r2}. Assuming that the stator and inner rotor are decoupled, see section 3.2, the optimal current vector $\boldsymbol{I^*}$ is derived. This assumption implies that the optimal stator current is solely depended on the stator torque. Consequentially, the inner rotor current is then only depended on the desired inner rotor torque. Since the field current $I_{r2,d}$ has a big impact on the flux linkage between the stator and inner rotor, see section 3.5, this current determines the stator torque as well. In [9], the decoupling of both systems is proven to be reasonable.

In a first approach both rotors are assumed to be at a physical standstill. This implies that the iron losses are negligible since the PM-field is not alternating. In this case the optimal stator and field current as as a function of the desired stator torque is calculated, see figures 4.4a, 4.4b and 4.4c. The inner rotor current is assumed to be zero. There appear to be two local optima minimizing the copper losses. One is situated in the high flux (HF) and the other in the low flux (LF) region, see figure 3.10. The low flux region optimum is the global optimum for a low stator torque. Increasing this torque will cause the global optimum to shift to the high flux optimum.

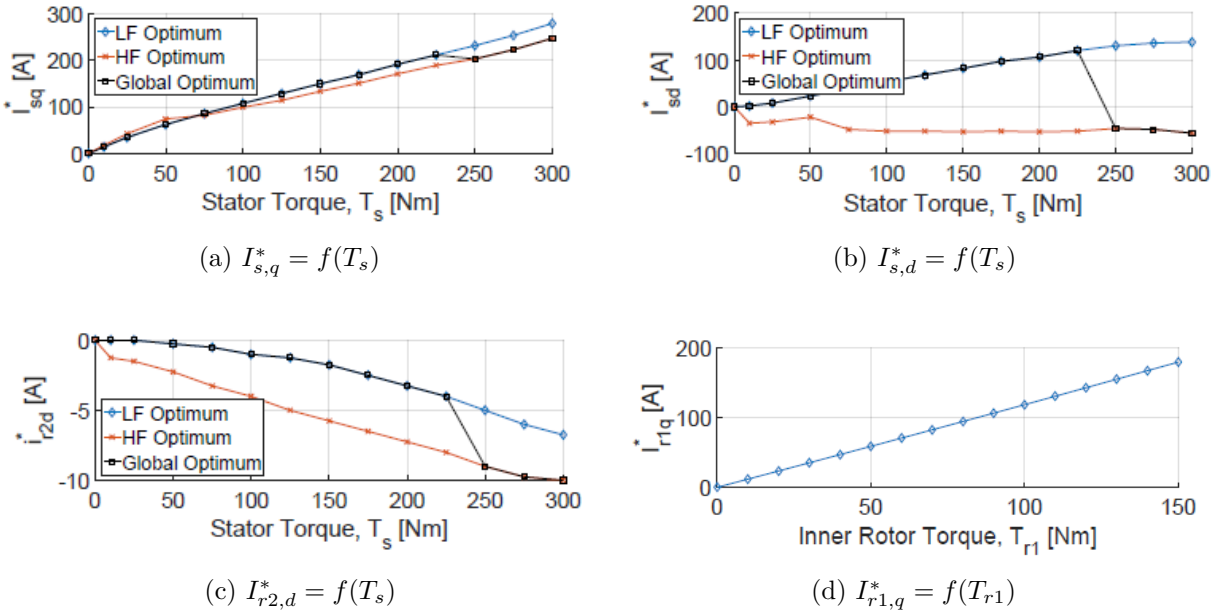

(a) $I^*_{s,q} = f(T_s)$

(b) $I^*_{s,d} = f(T_s)$

(c) $I^*_{r2,d} = f(T_s)$

(d) $I^*_{r1,q} = f(T_{r1})$

Figure 4.4: FEM-calculations: optimal current minimizing the copper losses in stator and inner rotor [9]

So far, the iron losses have been neglected. Increasing the rotational speed of both rotors will result in an rotating magnetic field. This causes iron losses having an impact on the global optimum. In [9] it is shown that the impact of the extra iron losses is only of practical importance for outer rotor speeds N_{r2} higher than 3000 rpm. This is true, especially for high stator torques, where the global optimum is situated within the high flux region. At higher speeds, this optimum will thus disappear such that only the low flux optimum remains.

Analogously, the optimal inner rotor current as a function of the desired inner rotor torque is determined. The d-axis inner rotor current $I_{s,d}$ is kept zero, independent of T^*_{r1}. This is done because the inner rotor has no saliency such that it has no effect on the inner rotor torque and thus only increases the copper losses. The optimum inner rotor current is then solely determined by it's q-axis component $I_{r1,q}$, see figure 4.4d. The determination of $I^*_{r1,q}$ is completely similar to the method described in the previous section.

In [9], the impact of the q-axis inner rotor current on the global optimum of $I_{s,q}, I_{s,d} and I_{r2,d}$is also calculated. The impact of $I_{r1,q}$ is elaborated in section 3.5. It changes the flux-linkage between the stator and outer rotor. The optimal stator d-axis current $I^*_{s,d}$ and field current $I^*_{r2,d}$ for different inner rotor currents is calculated, see figure 4.5. It can be seen that the impact is rather low for small stator torques. For a positive inner rotor current, the global optimum remains longer within the low flux region when increasing the stator torque. The impact of a negative inner rotor current is less prominent.

The description of the optimal current vector for different values of the stator and inner rotor torque, see equation 4.3, will be used to determine the optimal controller model. In fine, it is desired that the controller model works optimally for these optimal current vectors.

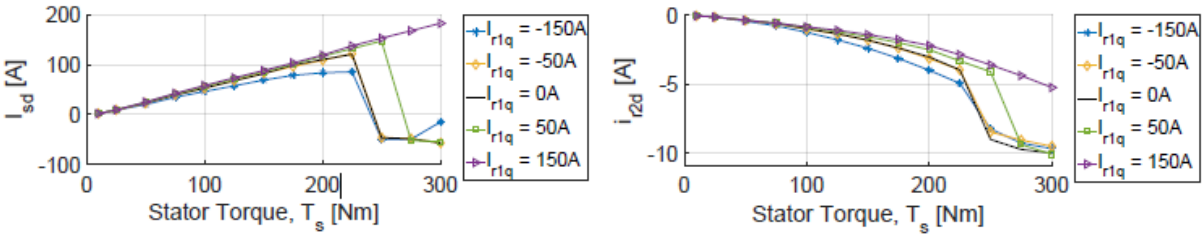

(a) $I_{s,d} = f(T_s, I_{r1,q})$ (b) $i_{r2,d} = f(T_s, I_{r1,q})$

Figure 4.5: FEM calculations: optimal field and d-axis stator current as a function of the q-axis inner rotor current $I_{r1,q}$

4.5 Model Based Predictive Control

After determining the optimal current values, the controller must be able to keep each current at it's desired value. To do this, *Finite Set-Model based predictive control (FS-MPC)* is used.

The MPC idea was suggested by Kalman in the early 1960's. It is an optimization based MIMO control technique that predicts optimal inputs for a system. The optimization is based on a cost-function specified by the designer. It was first successfully used in the petro-chemical industry and is used more and more in other industries. This non-linear control method has proven itself extensively for controlling electrical systems [46]. This is mainly due to the technological advancements in digital signal processors [47].

Nowadays, it is used to control renewable energy conversion systems such as wind [47] and solar PV [48]. To do this, the switch configuration of the PEC's is changed at certain frequency. A PEC only has a limited number of possible switching states, such that the controller only needs to predict the systems behaviour for these states. Each prediction is used to evaluate a cost-function. The prediction with minimum cost is then selected. This method is called Finite Set Model Predictive Control (FS-MPC). The same principle can be used to control the two PEC's controlling the current in the stator and inner rotor, see figure 4.2. The operation principle can be explained based on figure 4.6. This figure shows the principle if only one current component needs to be controlled. What is explained below minimizes the cost for 4 currents. The principle should be easier to understand by using this figure. It consists of three steps: estimation, prediction and optimization.

4.5.1 Estimation

At time-instant k, the measured currents $\boldsymbol{I}_m^k$ for both the stator and inner-rotor are known. Next to this, also the switch-configuration $\boldsymbol{S}^k$ is known. This results form the optimization of a cost-function at time-instant k-1.

$$\boldsymbol{I}_m^k = [i_{s,a}(k), i_{s,b}(k), i_{s,c}(k), i_{r1,a}(k), i_{r1,b}(k), i_{r1,c}(k)] \tag{4.5}$$

$$\boldsymbol{S}^k = [S_{s,a}^k, S_{s,b}^k, S_{s,c}^k, S_{r1,a}^k, S_{r1,b}^k, S_{r1,c}^k] \tag{4.6}$$

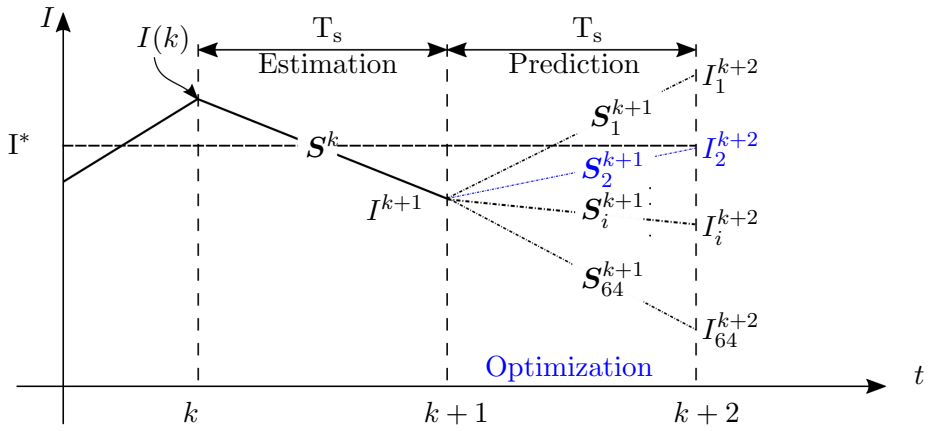

Figure 4.6: Overview working principle FS-MPC

Note that the switch-configuration only consists of 6 variables, while there are 12 IGBT's. Since the IGBT's of each leg work in a complementary way, the information contained in the switch-vector is sufficient to determine the whole switching-state. By using these data, it is possible to calculate the currents that should measured at time-instant k+1. This is done based on the model of the PM-EVT implemented in the controller. As described in section 4.2 the output phase voltage of each leg can be the positive halve DC-bus or the negative halve DC-bus voltage. In order for the model described in the previous chapter to be solvable, the voltage over the load must be known.

$$v_{x,yo}^k = v_{x,yn}^k - v_{x,on}^k \tag{4.7}$$

This is not the output phase voltage. $v_{x,yo}^k$ can be calculated by subtracting the voltage between the star point of the load and neutral clamp of the DC-bus from the output phase voltage. Since the load is three phase symmetrical, the second therm of equation 4.7 can be calculated as the average output phase voltage of each leg in an inverter.

$$v_{x,on}^k = \frac{1}{3}(v_{x,an}^k + v_{x,bn}^k + v_{x,cn}^k) \tag{4.8}$$

This is the exact definition of a homopolar voltage component. As already explained in section 3.4.2, an hompolar voltage component will not result in a zero current since it cannot flow. No power is thus associated with this zero-sequence component. Applying these voltages to the implemented controller model, with initial conditions the current $\boldsymbol{I}_{\mathrm{m}}^{\mathrm{k}}$, gives an estimate of the current at time instant k+1. Note that the model is derived in the qd-reference frame. The same holds for the desired values for the current in stator and inner rotor. Therefore the measured currents are first transformed to the qd-frame. To do so, the Clarke and Park transformation, see equations 3.10 and 3.12 are applied. Note that the instantaneous angle of this reference frame is needed. This can be easily estimated based on speed measurements. Afterwards the estimation is determined.

$$\boldsymbol{I}^{k+1} = [I_{s,q}^{k+1}, I_{s,d}^{k+1}, i_{r1,q}^{k+1}, i_{r1,d}^{k+1}] \tag{4.9}$$

4.5.2 Prediction

After the estimation-step comes the prediction-step. In this step the controller will determine what the current will be at the next time-instant k+2 when a certain switch-configuration is applied. As already said, there are 64 different configurations that can be set to the system. The effect of each switch-configuration will be calculated based on the implemented controller model. This occurs in a similar way as the estimation-step. Only now, the initial conditions are no actual measurements. They are the currents resulting from the estimation-step. The amount of steps that have to be predicted, the so called prediction horizon N, depends on the control system itself. Intuitively it is clear that increasing N mostly results in a better approximation of the desired values. It can also give less accurate predictions due to the use of a simplified model and other unknown disturbances. No predefined method to determine N exist. This should be tuned in simulation. The outcome of the prediction-step is 64 possible current-vectors I_z^{k+1+N} corresponding to a certain switch-configuration S_z .

$$\boldsymbol{I}_z^{k+1+N} = [I_{s,q}^{k+1+N}, I_{s,d}^{k+1+N}, I_{r1,q}^{k+1+N}, {}_{r1,d}^{k+1+N}]_{p,z} \; z \in \{0, 1, ..., 64\} \tag{4.10}$$

$$\boldsymbol{S}_z^{k+1} = [S_{s,a}^{k+1}, S_{s,b}^{k+1}, S_{s,c}^{k+1}, S_{r1,a}^{k+1}, S_{r1,b}^{k+1}, S_{r1,c}^{k+1}]_z \tag{4.11}$$

Note that there are some redundancies. This means that some switch states will have the same effect on the EVT according to the model in the controller and thus result in the same current. In figure 4.6 the prediction horizon is set to be one.

4.5.3 optimization

In the last step, all the predicted current-vectors are evaluated based on a certain cost-function. The vector corresponding to the lowest cost, will then be set at the next time-instant k+2. in principle, this cost-function can be anything. It can represent the weighted sum of squared differences between the reference value and the prediction of each element in one current vector. An extra therm can be added incorporating the joule losses that come with a certain switch configuration. Since the minimization of the joule losses has already been incorporated for determining the optimal reference values, it will not be considered here. The weight factors W are important for this performance of the controller and is something that should be tuned as well. The cost-function that will be used in this thesis is

$$\begin{aligned} J = \sum_{i=1}^{N} & \mathrm{W_{s,q}}(I_{s,q,ref}^{k+1+i} - I_{s,q}^{k+1+i})^2 + \mathrm{W_{s,d}}(I_{s,d,ref}^{k+1+i} - I_{s,d}^{k+1+i})^2 + \\ & \mathrm{W_{r1,q}}(I_{r1,q,ref}^{k+1+i} - I_{r1,q}^{k+1+i})^2 + \mathrm{W_{r1,d}}(I_{r1,d,ref}^{k+1+i} - I_{r1,d}^{k+1+i})^2 \end{aligned} \tag{4.12}$$

The big advantage of FS-MPC is that the cost-function can easily be evaluated for each current-vector. No complicated time-consuming minimization method must be used here.

4.5.4 Timing

This entire system is then implemented in a Matlab-Simulink environment. It is desired that this simulation comes as close as possible to the reality. Since a lot of calculations have to be

done simultaneously timing is very important here. Each of the steps discussed above must be executed in a time that is smaller then the sampling period T_s. In the figure below it is graphically shown how the timing of the controller is related to the real time.

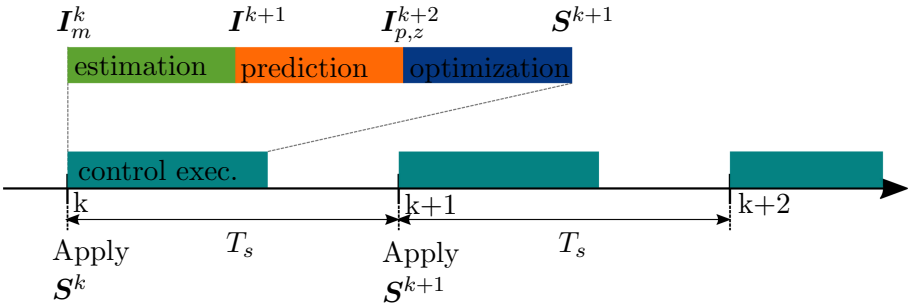

Figure 4.7: Overview working principle FS-MPC [10]

As mentioned above the switching frequency of the IGBT's will be set to 10 kHz. Consequentially, the controller should work at the same frequency. In section 4.2, it was shown that during each switching period, the PM-field of the rotor will rotate 4 % of one turn, which is significant. Therefore two sample frequencies will be used in the simulation. The machine-model described in the previous chapter will be sampled, and thus calculated, 10 times faster then the controller. The second sample frequency is then 100 kHz. There is a second reason for this. As described in section 4.1, that the controller requires measurements at each instant k. In order for the simulation to be realistic, the currents should be measured at an instant slightly before the controller calculations start. This can be done easily when two sample frequencies are used. Therefore, the current determined 1/10th before the actual switching instant is used as measurement input to the controller, see figure 4.8. using these measurements, the estimations and predictions are calculated. They become available somewhere in between the switching period. Timing is very important. This will be taken into account for future development of this control system.

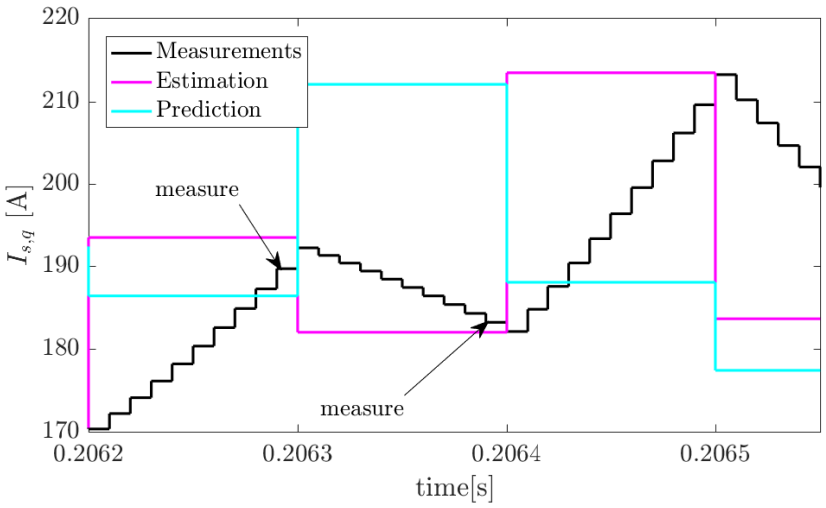

Figure 4.8: Measurement instant

4.6 The controller model

Until now, no information was given concerning the model that is used by the controller. The complex model, explained in the previous chapter, can not be implemented due to practical reasons. Simplifications will therefore have to be made. It is a matter of tuning in order to determine the optimal controller model giving the best results for every operation mode.

To do so, the electrical system in a Matlab-Simulink environment is used. Based on the desired torque quantities at the inner and outer rotor, reference values for the current are obtained by using the optimal control look-up tables described in section 4.4.2. These values are then presented to the predictive current controller described above. This controller drives the PEC's which are connected to the windings of the stator and inner rotor. The model of the PM-EVT described at the end of the previous chapter is used as a machine model. Since a high rotational speed at the outer rotor is desired in certain applications, the back-EMF of this machine can be high. This means that DC-bus voltage of 600 V is needed in order to be able to control the system. This will be taken into account during the development of the system.

Determining the optimal controller model, requires knowledge of the influence of each current on the flux-linkage. This is already elaborated in section 3.5. It can be concluded that the impact of some current components is smaller and will not contribute to a better estimation of each current component. A sensitivity study is executed to evaluate the importance of an extra current-component in the controller model. First, the ideal model was implemented in the controller of the EVT. The entire system is then subjected to different test cases, covering a big part of the operation modes of the PM-EVT, see section 3.3. These test cases are listed in table 4.1.

Case	T_s[Nm]	T_{r1}[Nm]	V_{dc}[V]	N_{r1}[rpm]	N_{r2}[rpm]	$I^*_{s,q}$[A]	$I^*_{s,d}$[A]	$I^*_{r2,d}$[A]	$I^*_{r1,q}$[A]
1	0	0	600	1500	2500	0	0	0	0
2	-50	0	600	1500	2500	62.33	23.01	-0.25	0
3	-100	0	600	1500	2500	107.52	53.01	-1.00	0
4	-150	0	600	1500	2500	149.73	82.001	-1.75	0
5	-200	0	600	1500	2500	191.39	106.01	-3.25	0
6	-250	0	600	1500	2000	231.39	-50	-9.1667	0
7	-300	0	650	1500	3000	278.83	138	-6.75	0
8	0	-150	600	1500	2500	0	0	0	199.29
9	0	-50	600	1500	2500	0	0	0	56.88
10	-50	-50	600	1500	2500	62.33	23.01	-0.25	56.88
11	-100	-100	600	1500	2500	107.52	53.01	-1.00	121.64
12	-250	-100	600	1500	2000	231.39	-50	-9.1667	121.64

Table 4.1: Test cases

For each test case the absolute bias, Mean Squared Error (MSE) between the measurement and desired value of each current haven been calculated. The results for the ideal controller model are then used as a benchmark. Some current components determining the estimation of a certain flux-linkage and thus also the derivative to each current component, see equation 3.17, can be

Model	$\Psi_{s,q}$	$\Psi_{s,d}$	$\Psi_{r1,q}$	$\Psi_{r1,d}$
a	$L_{s,q}I_{s,q}$	$L_{s,d}I_{s,d}$	$L_{r1,q}I_{r1,q}$	$L_{r1,d}I_{r1,d}$
b	$L_{s,q}I_{s,q}$	$\boldsymbol{f(I_{s,d}, I_{r2,d})}$	$L_{r1,q}I_{r1,q}$	$L_{r1,d}I_{r1,d}$
c	$L_{s,q}I_{s,q}$	$f(I_{s,d}, I_{r2,d})$	$\boldsymbol{f(I_{r1,q}, I_{s,q})}$	$L_{r1,d}I_{r1,d}$
d	$L_{s,q}I_{s,q}$	$f(I_{s,d}, I_{r2,d})$	$f(I_{r1,q}, I_{s,q})$	$\boldsymbol{f(I_{r1,d}, I_{s,d}, I_{r2,d})}$
e	$\boldsymbol{f(I_{s,q})}$	$f(I_{s,d}, I_{r2,d})$	$f(I_{r1,q}, I_{s,q})$	$f(I_{r1,d}, I_{s,d}, I_{r2,d})$
f	$\boldsymbol{f(I_{s,q}, I_{s,d}, I_{r2,d})}$	$f(I_{s,d}, I_{r2,d})$	$f(I_{r1,q}, I_{s,q})$	$f(I_{r1,d}, I_{s,d}, I_{r2,d})$
g	$f(I_{s,q}, I_{s,d}, I_{r2,d})$	$\boldsymbol{f(I_{s,q}, I_{s,d}, I_{r2,d})}$	$f(I_{r1,q}, I_{s,q})$	$f(I_{r1,d}, I_{s,d}, I_{r2,d})$

Table 4.2: Controller models

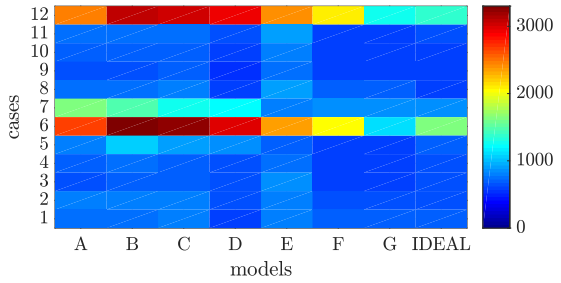

Figure 4.9: Average MSE

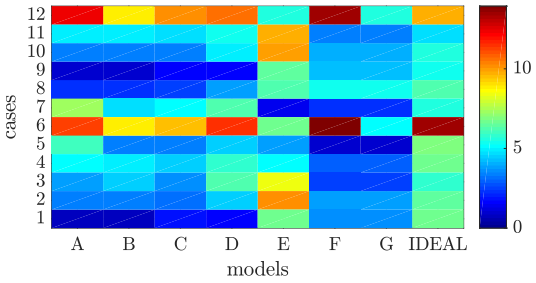

Figure 4.10: Average Absolute Bias

omitted. This can have an effect on performance of the controller. Quantifying this, allows us, to determine the optimal workable controller model.

Different controller models were implemented in the controller, an overview is given in table 4.2. In each model an extra parameter is added to estimate a certain flux-component. Only those currents for which a direct influence can be noticed will be incorporated. For example, The inner rotor current will have a minor impact on the stator flux linkage, see section 3.5. For more numerical information concerning these models, please refer to appendix B.

Each controller is then used for the case shown in table 4.1. At a certain inner and outer rotor speed, a torque step at inner and/or outer rotor is set. The results are shown in figures 4.13 -4.20 and will be discussed in the sequel of this section. Note that the colormap scale differs for some figures. Comparing them, must be given the necessary attention. however, the main purpose of these figures is to focus on the improvement of each current-component separately. In order to give a general view on the performance of the controller, the average MSE and absolute bias of all currents is also given in figures 4.10 and 4.9.

The MSE is caclulated based on the measurements used by the controller and the d- and q-axis reference currents at that time. If there are N measurements available of a current I, then the MSE is calculated according to this equation:

$$MSE = \frac{1}{\mathrm{N}} \sum_{k=1}^{\mathrm{N}} (I(k) - I_k^{ref})^2 \tag{4.13}$$

The MSE is a measure for the variance between the actual current and the desired value. A high MSE tells us that the ripple around the desired value is high. A high ripple results in more iron losses, noise. Therefore it is important to minimize this. The user also wants the average actual

current to be the same as the desired value. Every time the model becomes more detailed, the better the overall performance of the controller. The optimal controller is then model G, which is the most detailed.

A first thing to notice is that the controller model E-F encountered problems for case 6 and 12. In these cases, the desired d-axis stator current $I_{s,d}$ is negative as well as the field current $I_{r2,d}$. Since the desired stator torque is high in both cases, so is $I_{s,q}$. It was shown in section 3.5, that for a negative $I_{s,d}$ and high $I_{s,q}$ a serious impact can be notice on the stator flux in both axes, see figures 3.12 and 3.14. The partial derivative of the stator flux to the both currents is therefore significant. Also, because of the high DC-bus voltage, a high variance can be noticed for both currents, see figures 4.15 and 4.13. In appendix A.1, it can be seen that, for both operation points, a high variance of these currents also results in a rapid change of the partial derivatives. To overcome these issues, three adjustments were made to the controller model.

1. In model G, the entire model of the stator flux-linkages as a function of the stator current is incorporated, see figure 4.11 This is the most obvious solution.

2. Calculating the *Jacobian* for a measeasured current vector $\boldsymbol{I}$, will result in a bad approximation of the average Jacobian for the time between each control action. To overcome this problem discretized planes were used to describe the flux-linkage as a function of it's current components, see figure 4.11a. In this way, the partial derivative to each current component is automatically averaged.

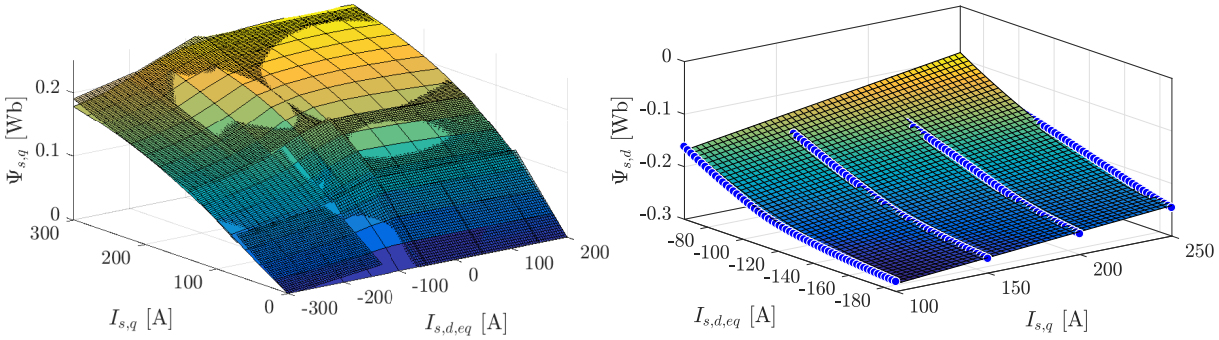

(a) $\Psi_{s,q} = f(I_{s,q}, I_{s,d,eq})$ (b) $\Psi_{s,d} = f(I_{s,q}, I_{s,d,eq})$

Figure 4.11: Matlab fit of the stator flux

3. The third and last adjustment is a consequence of the use of these discretized planes. This discretization improves the performance of the controller, as long as the current stays within the present discretized area. For example, consider **??**. At instant k, a d-axis stator current $I_{s,d}$ of -50 A is measured. In that case, the stator flux-linkage is highly saturated. The partial derivative $\partial\Psi_{s,d}/\partial I_{s,d}$ will be small. If now, due to variance, $I_{s,d}$ highly increases, the stator yoke can become magnetically linear. At k+1, a $I_{s,d}$ of 0 A is measured. In that case $\partial\Psi_{s,d}/\partial I_{s,d}$ will be much higher. The estimated $\partial\Psi_{s,d}/\partial I_{s,d}$ at instant k is thus not a correct measure for the average $\partial\Psi_{s,d}/\partial I_{s,d}$ of the time between both control actions. To overcome this problem the controller uses an averaged value. In a first step, an estimation of the flux $\Psi_{s,d}$ and it's partial derivatives to each current paramter is made, using the measured currents $\boldsymbol{I}$ at time-instant k. The same is done for the other currents. Using this, an estimation of the derivative of each flux-linkage to time,

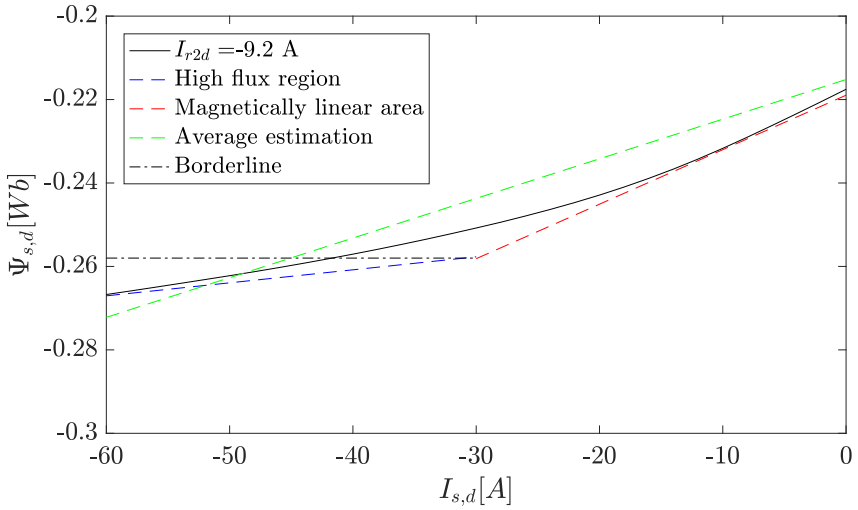

Figure 4.12: Issue when using discretized planes

can be made, see equation 3.17 and 3.18. Until now, the partial derivatives to time are not needed. Using this an accurate prediction of the flux-linkage at time-instant can be made. The borders between the high-flux and the magnetically linear region is more or less constant if the equivalent d-axis stator current is used. The controller can thus more or less know what the saturation state will be at time instant k+1. If ,indeed, the saturation state changed, the partial derivative of the d-axis stator flux, to the corresponding current will be adjusted as follows.

$$\frac{\partial \Psi_{s,d}}{\partial I_{s,d}}_{average} = 0.75 \frac{\partial \Psi_{s,d}}{\partial I_{s,d}}_{linear} + 0.25 \frac{\partial \Psi_{s,d}}{\partial I_{s,d}}_{initial} \tag{4.14}$$

These weight factors are tuned based on simulation. It could also be determined exactly iteratively, but thus will slow down the controller.

Only if those three adjustments were executed negative $I_{s,d}$ could be handled by the controller.

The second thing to notice is that model G performs even better then the ideal case which is used as a bench mark. This reason for this, again, due to those three adjustments described above. The ideal model calculates the Jacobian based on the measured currents at time instant k. This can give inaccurate estimations, as explained above.

A list thing to remark is the bad overall performance of model E. There are two reasons for this. First, the model describing the stator flux-linkage is still inaccurate. This results in bad estimations of the stator current. Consequentially, the MSE and absolute bias increase, except for case 5, 6, 7 and 12. For these states the the stator yoke is highly saturated. Models A-F use a constant chord-slope inductance as a measure for $\partial \Psi_{s,q}/\partial I_{s,q}$. This gives better result for low stator currents, since high variation of $\partial \Psi_{s,q}/\partial I_{s,q}$ can be noted there. If, however, the stator yoke is saturated, this is an inaccurate estimation. Model E takes this into account such that a better approximation can be made. The second reason is again related to the fact that discretized planes are used, as explained above.

Some improvements could be made to the performance of the controller. However, in order to detect faults, an accurate controller-model is required. Therefore, it was opted to use the model, giving the best results in therms of estimation and predictions.

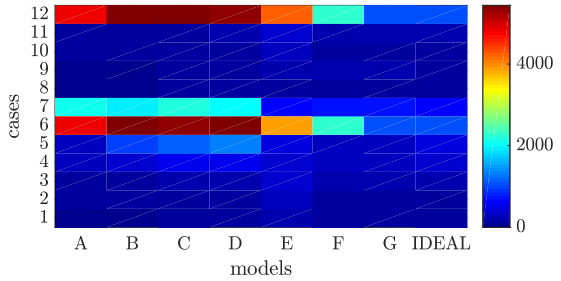

Figure 4.13: MSE $I_{s,q}$

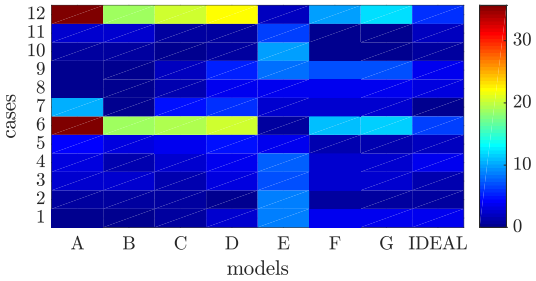

Figure 4.14: Absolute Bias $I_{s,q}$

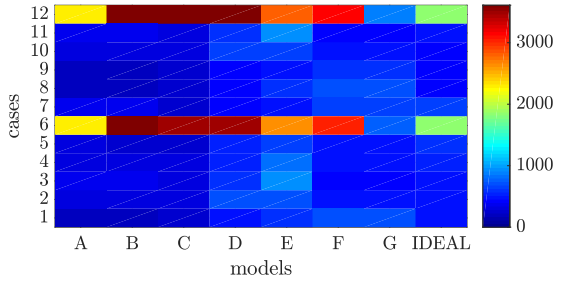

Figure 4.15: MSE $I_{s,d}$

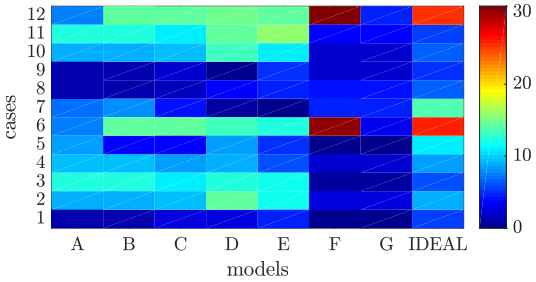

Figure 4.16: Absolute Bias $I_{s,d}$

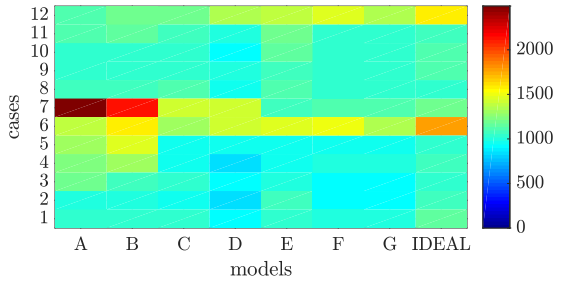

Figure 4.17: MSE $I_{R1,q}$

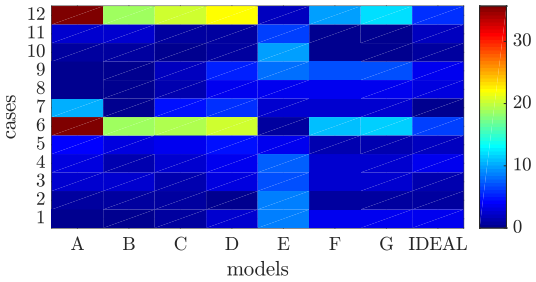

Figure 4.18: Absolute Bias $I_{R1,q}$

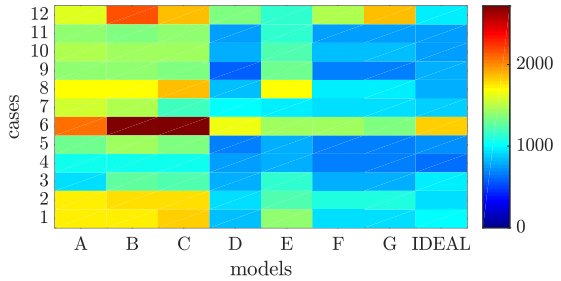

Figure 4.19: MSE $I_{R1,d}$

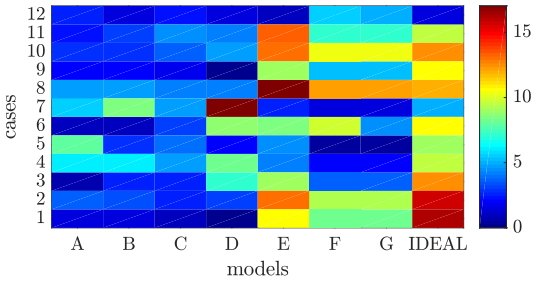

Figure 4.20: Absolute Bias $I_{R1,d}$

Chapter 5

Response Analysis

5.1 Introduction

Until now, simulation results are never depicted or discussed in detail. In this chapter two test cases will be subjected to the optimal controller. The operation conditions are shown in table 5.1. In order to approximate the real situation as close as possible, measurement errors and temperature variations will be taken into account. It is also important that the controller works under speed variations. Therefore, both test-cases will be executed in one simulation. In this way, the speed will be altered.

testcase	1	2
T_s[Nm]	-100	-250
T_{r1}[Nm]	-100	-100
T_{r2}[Nm]	200	350
V_{dc}[V]	600	600
N_{r1}[rpm]	1500	1500
N_{r2}[rpm]	2500	2000
$I^{ref}_{s,q}$[A]	107.52	231.39
$I^{ref}_{s,d}$[A]	53.008	-50
$I^{ref}_{r1,q}$[A]	121.64	121.64
$I^{ref}_{r1,d}$[A]	0	0
$I^{ref}_{r2,d}$[A]	-1	-9.1667

Table 5.1: Test cases torque step

5.2 Torque-step and speed variations

5.2.1 Impact of the temperature

Until now, it is assumed that temperature in the electrical machine is constant. However in reality, this is not the case. A temperature variation will result in a variation in the magnetic permeability of the iron on the machine. But more importantly this will affect the resistance of both the stator and inner rotor.

In the simplified machine model every resistance and inductance is assumed constant. This is of course not true. The resistance of the conductors is strongly temperature depended. If the temperature does not very too much, a linear approximation is typically used:

$$R(T) = R_0[1 + \alpha(T - T_0)] \tag{5.1}$$

where α is defined as the temperature coefficient of the resistance, R_0 and T_0 denote the reference values at aa certain reference temperature (mostly the ambient temperature). For copper, α equals $3.9 \cdot 10^{-3}/°C$. The resistance of each phase in both the stator and inner rotor is $\approx 0.02\Omega$ at a rated current of 30 Amps. Suppose now that the temperature of copper, for some random reason, increases 30 K. This will result in relative increase of $\approx 10\%$. Although this formula is an approximation of what happens in reality ($\alpha \sim T[°C]$), it gives an idea of resistance variation. This will be incorporated when simulating both test cases. In the following test-cases, the stator resistor will be increased with 0.1Ω.

5.2.2 Measurement error

It has been shown in the previous chapter that the controllers requires some measurements, in order to operate. All these measurements will have certain amount of error. When speaking about measurement errors (ME), an inaccuracy is in fact a statistical uncertainty between certain boundaries:

- Voltage measurement: ME $\sim 5\%$
- Current measurement: ME $\sim 1\%$
- speed measurement: ME $\sim 0.5\%$

This must also be taken into account.

5.2.3 Results

Both disturbances are included in the simulation model. Both test case are subjected to the controller in one simulation. The torque and speed at both rotors are shown in, respectively, figure 5.1 and 5.2. Note that the torque delivered to the outer rotor is not equal to 350 Nm, when the second test-case is applied. This is due to the fact that the controller only regulates the current. Based on equations 3.19, the torque is calculated.

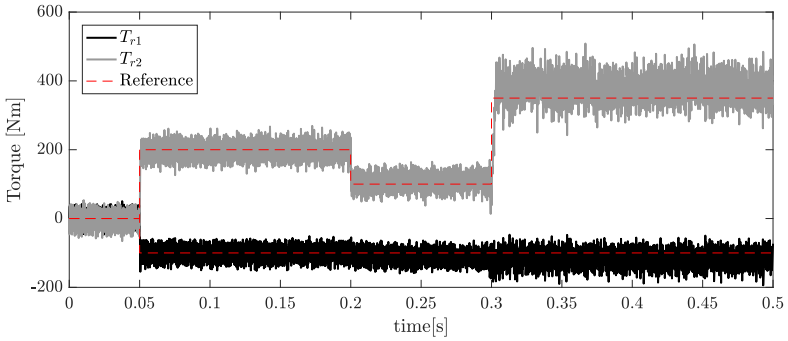

Figure 5.1: Torque delivered to both rotors

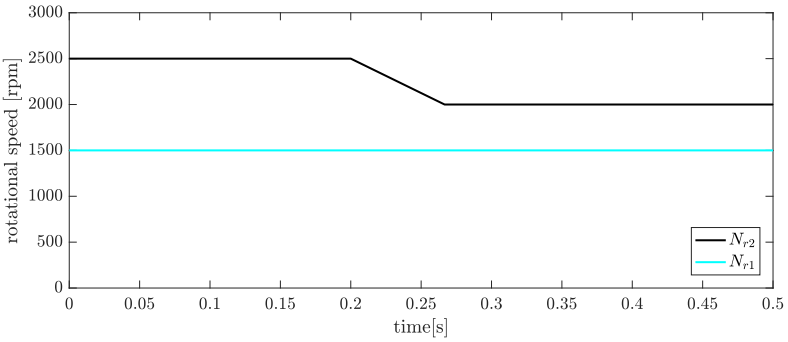

Figure 5.2: Speed of both rotors

It is more instructive to discuss the behaviour of the q- and d-axis current in both the stator and inner rotor. This is shown in figures 5.4-5.7. from this it can be seen that the controller succeeds in controlling the current in both the stator and rotor. Note the d-axis stator current measurements contain some negative peak values. This is a consequence of the sudden change in $\partial\Psi_{\mathrm{s,d}}/\partial I_{\mathrm{s,d}}$ when the $I_{\mathrm{s,d}}$ is fluctuating around -50 A. Altough some measures were taken to reduce these peak values, see section 4.6, this sudden variation does not disappear. In figure 5.3, the estimations and predictions made by the controller are shown. The time range is chosen in way such that the $I_{\mathrm{s,d}}^{\mathrm{ref}}$ is negative at that time. From this it can be seen that the controller indeed predicts the highly negative d-axis stator current. The behaviour is thus a characteristic of the PM-EVT itself.

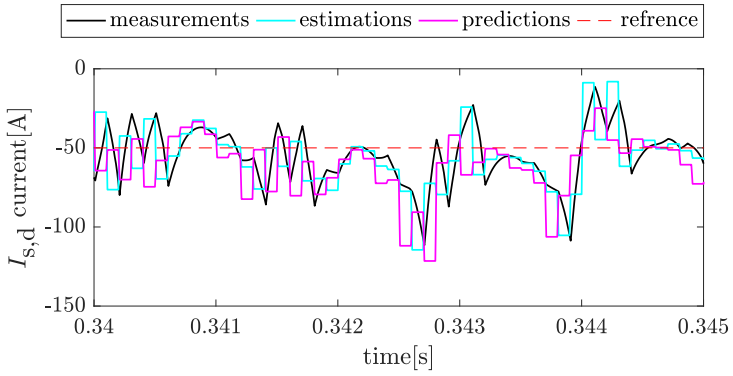

Figure 5.3: Simulation: predictions and estimations of the d-axis stator current

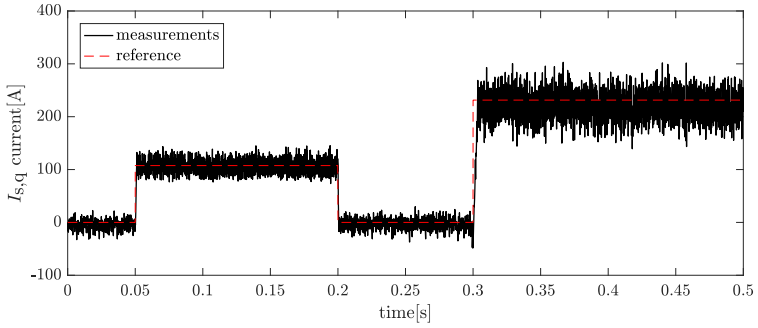

Figure 5.4: Simulation: q-axis stator current

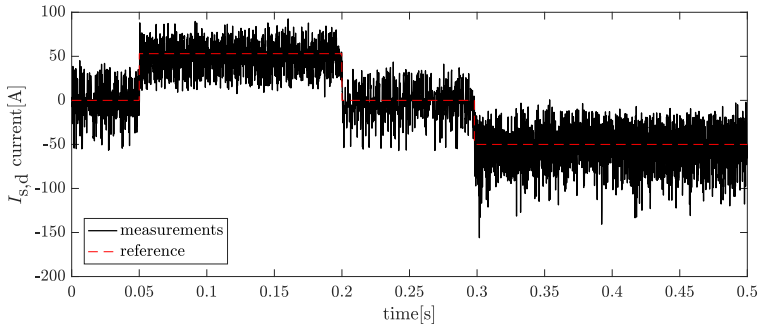

Figure 5.5: Simulation: d-axis stator current

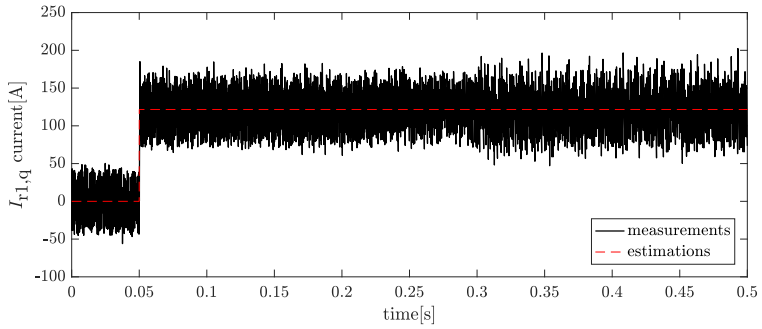

Figure 5.6: Simulation: q-axis inner rotor current

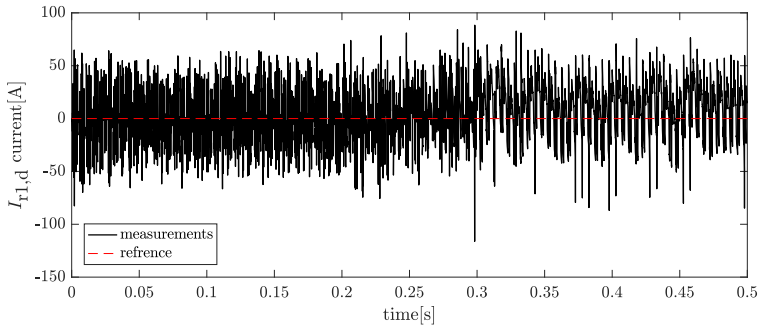

Figure 5.7: Simulation: d-axis outer rotor current

Table 5.2: Simulation: step characteristics case 1 and 2 (S.T.= Settling Time)

Cases	1				2			
	Isq	Isd	Ir1q	Ir1d	Isq	Isd	Ir1q	Ir1d
S.T. [s]	0.00582	0.00655	0.00543	0	0.0083	0.0093	/	/
Overshoot[%]	0	0	0	0	0	16.72	/	/
max SS [A]	145.27	92.464	184.65	64.261	302.87	0.6043	202.41	82.777
min SS [A]	73.476	3.901	61.976	-66.47	139.34	-140.58	47.167	-86.898
MSE	179.56	282.88	719.62	665.43	696.74	389.69	698.2	716.4
Bias [A]	-1.2634	-4.0078	-2.0931	-1.3057	-11.512	-2.1397	-2.6641	8.7058

It can also be seen that the system is capable to handle speed variations. Great attention is required when discussing the effect of the speed on the performance of the controller, this will be discussed in the last section of this chapter. In the table 5.2, the characteristics of the step response for both cases is shown. In order to determine the settling time and overshoot a moving averaged window is used. The MSE and bias is calculated as in section 4.6.

These values are in agreement with the values determined in the ideal case, i.e. without disturbances, see section 4.6. The MSE of the q-axis inner rotor current in case 1 is higher, in comparison to case 2. At first, this seems strange, since the minimum and maximum value in steady state (SS) for case 1 is significantly lower in comparison to those calculated in case 2. However, this is entirely correct. The reason for this is the fact that, in between the higher current peaks, see figure 5.6, the deviation from the desired current is significantly lower.

5.3 Comparison: PI-controller

In order to determine the advantages and disadvantages of the use of a FS-MPC -controller, a comparison will be made with the performance of a simple PI-controller. This PI-controller, used PWM-modulation to regulate the current. Both case were also subject to this system, the performance quantities are given in 5.3. These case have been tested separately. The regulation of the q- and d-axis current is shown in figures 5.8 and 5.9. Note that now, both cases are subjected separately. However, this should not make much of a difference.

Table 5.3: Simulation: step characteristics case 1 and 2 (S.T.= Settling Time)

Cases	1				2			
	Isq	Isd	Ir1q	Ir1d	Isq	Isd	Ir1q	Ir1d
S.T. [s]	0.0105	0.0125	0.00056	/	0.00289	0.0312	/	/
Overshoot[%]	8.8332	9.8388	1.5565	21.765	1.9465	75.43	/	/
undershoot[%]	7.1277	0	16.067	0	7.4995	0.95766	/	/
max SS [A]	113.78	56.22	122.53	3.3204	234.58	-47.87	123.51	2.0558
min SS [A]	107.08	50.682	120.77	-3.8493	229.44	-52.762	121.04	-3.4633
MSE	0.916	0.610	0.146	1.879	0.426	0.814	0.233	1.176
Bias [A]	0.449	0.183	0.259	0.379	-0.28914	-0.511	0.289	-0.045

A first thing to notice, is that the settling time for the stator current is significantly higher in comparison the the MPC-controller. For certain applications, such as weaving looms, this is desirable. Secondly, a bigger overshoot is present when a PI-controller is used. The current first has an opposite sign of the reference value, before it is regulated to this value. When A PI controller is used, there is a trade-off between the elimination of a steady state error and the overshoot. If a low steady state error is wanted, the PI-controller must be aggressive. This means that a high I-action must be present. This also results in a higher overshoot since just after the step is subjected to the controller, the error is very high. The stronger the P- and I-action, the steeper the current will rise initially. Consequentially, the overshoot will be higher as well. This can be seen in both figures 5.8 and 5.9. Also an undershoot appears now. This can be seen in the step response of the q-axis current in both the stator and inner rotor. This is a typical non-minimum phase behaviour and is disturbing from controller point of view [49]. the MPC-controller performance much better in these areas.

The main advantage of the use of a PI-controller is the smaller MSE and bias. Though, this is not exactly due to the use of a PI-controller. But rather due to the use of a PWM-modulation. When using this technique, the switching state can be altered much faster, 10 times, in comparison to the usage of a MPC-controller without this system. Naturally, this gives much lower MSE and bias. It also requires much lower computational power, in comparison to an FS-MBPC controller. The cost of a PI-controller is much lower then the a FS-MBPC controller. Also, the model derived in chapter 4, is specific for this type of PM-EVT. Although a similar model can be derived for other PM-EVT's. A lot of calculations have to be done beforehand, e.g. FEM-calculations. This requires a lot of resources for a company. Therefore, using a simple PI-controller can be sufficient in some situations.

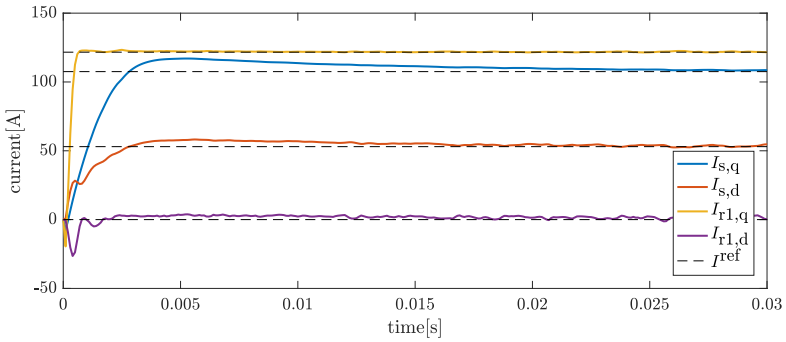

Figure 5.8: Simulation PI-controller case 1: qd-currents

Though, it is opted in this thesis to use FS-MBPC as a control-method. There are multiple reasons for this:

1. The parameters of a PI-controller are tuned based upon step-response or models. The P and I parameters are fixed. For linear systems this is fine, but when the system is higly non-linear the performance of the controller will be sub-optimal. This is not the case when a FS-MPC controller is used. When an accurate model is used, the performance of the controller is optimal for almost the entire operation range of the system. Since the PM-EVT is highly non-linear, an MPC-control method is desired.

2. When talking about fault-detection systems, a model is needed in order to sense that

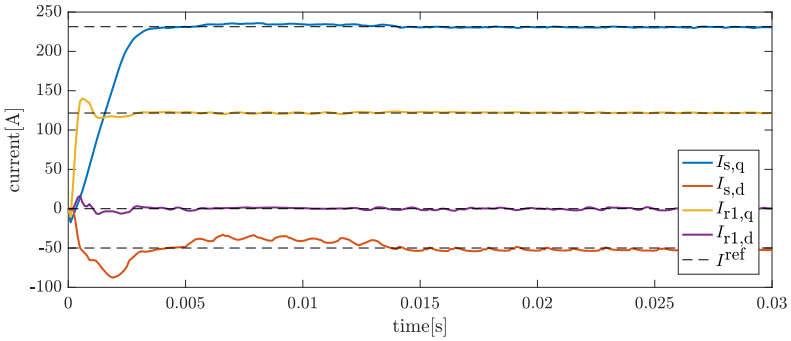

Figure 5.9: Simulation PI-controller case 2: qd-currents

something is wrong. Since In FS-MBPC a model is already at our disposal, again FS-MBPC is opted.

5.4 Speed vs. Torque

In order to be able to supply a symmetrical three phase load with a symmetrical sinusoidal three-phase voltage, i.e. being able to create a rotating field, a rotating vector V must exist, see figure 4.3. At each controller-instant, the controller decides which switch-configuration will be set, in order to approximate this rotating vector as close as possible. The maximum power deliverable to the system, is depending on the maximum amplitude of the voltage vector, the system is able to supply continuously. When Space Vector Modulation is used, this maximum average voltage deliverable to the system is the radius of the inscribed circle in the hexagon [19].

$$V_{max} = \frac{V_{dc}}{\sqrt{3}} \tag{5.2}$$

It has already been pointed out that the deliverable power depends on the rotational speed of both rotors. This is easy to understand, given that the this rotational speed determines the back-EMF. The maximum deliverable torque can be calculated theoretically, based on equations 3.13. If these equations are considered in steady state, they can be simplified to:

$$\begin{cases} V_{s,q} = R_s I_{s,q} - \omega_{r2} \Psi_{s,d} \\ V_{s,d} = R_s I_{s,d} + \omega_{r2} \Psi_{s,q} \end{cases} \tag{5.3a}$$

$$\begin{cases} V_{r1,q} = R_{r1} I_{r1,q} - (\omega_{r2} - \omega_{r1}) \Psi_{r1,d} \\ V_{r1,d} = R_{r1} I_{r1,d} + (\omega_{r2} - \omega_{r1}) \Psi_{r1,q} \end{cases} \tag{5.3b}$$

Based on the statements derived in 4.4.2, it is known what the currents in both the stator and inner rotor should be, in order to achieve a certain torque. In turn, these values determine the steady state flux-linkages, based on the look-up tables. It can thus be calculated, what the q- and d-axis voltage must be, in order to be able to supply this current. These values depend on the rotational speed of both rotors.

Knowing what the maximum deliverable voltage is, it is possible to determine if these currents can be supplied in a fault-tolerant mode or not. The qd-reference frame, rotating at the speed

of the rotating PM-field, will thus result in a rotating vector $\underline{V}$. It is this vector, that must be approximated by applying different switch-configurations at each control instant. The values of the q- and d-axis voltage, determine the amplitude of the rotating voltage vector.

$$|\underline{V}| = \sqrt{V_{y,q}^2 + V_{y,d}^2} \leq \mathrm{V_{max}} \tag{5.4}$$

This is calculated for both the stator and inner rotor and validated by simulation. The DC-voltage is set to be 600 V. The results for stator and inner rotor are respectively shown in figure 5.10a and 5.10b. when the torque reaches 250 Nm the maximum torque line is split. the lower part belongs to the high flux optimum and the upper line to the low flux optimum, see section 4.4.2. It can be seen that the maximum deliverable torque, is a bit lower in comparison to theoretical expectations. Especially for the stator. The reason for this, is the fact that the theoretical maximal torque is calculated in steady state. The derivative of the flux-linkage to time is fluctuating around zero and lowers the q- and d-axis voltage. This explains the offset.

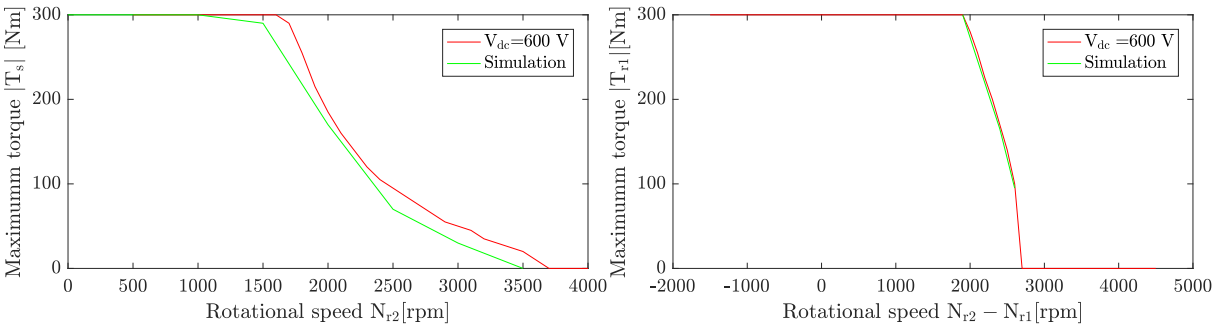

(a) Stator

(b) Rotor

Figure 5.10: Simulations: maximal deliverable torque in normal operation operation and at $\mathrm{V_{dc}} = 600$ V.

Chapter 6

Inverter-faults

6.1 Introduction

As described in chapter 2, one of the possible faults that can occur in the EVT-setup are those in the inverters, feeding the stator and inner rotor. Mostly these faults are caused by the failure of an IGBT or transistor. In this chapter, a method for the detection of these faults will be described. The IGBT responsible for this fault should be identified as soon as possible, such that the EVT is not exposed to an assymetric voltage supply for a long time. This can be hazardous for the EVT and elements connected to it. If, for example, an EVT is used in an Hybrid Electrical Vehicle (HEV) then such a fault is not only hazardous for the vehicle itself, but also for it's environment.

The detection of this fault-type is not only useful for this application. In every system where inverters are used to fed an electrical machine, an early detection and localisation of the broken switching-device can avoid extra damage (and costs) to the machine and inverter. In solar systems, for example, an inverter is used to transform the DC-voltage produced by a group of solar panels into an AC-voltage which can be fed to the grid. If one switch is broken, then the assymetry in the output voltage of the inverter will unbalance the grid. This is also undesirable.

In this chapter two topics will be discussed. Firstly, a detection-method based on the, already implemented, control principle FS-MBPC, will be discussed. The ideas behind FS-MBPC are already explained in chapter 4. This part of the chapter is based on the statements derived in the master-thesis of ir J. Druant [8]. Secondly, it has been shown in the introductory chapter that faults result in a long-therm downtime. however, for some faults, minor adjustments to the system are sufficient to ensure the operation of electrical machines in general. This is the second topic of this chapter.

6.2 Fault-detection

In this chapter, a broken IGBT means that the device does not want to turn into it's conduction state when a gate-pulse is applied. This can be caused by an internal failure in the IGBT itself or a fault in the driver. The other fault-type where the IGBT does not want to change into it's off-state is not considered here. If this fault-type occurs, the battery will be shorted anyway

and an external fuse should react and decouple the affected phase. When discussing the failure of an IGBT, it is always referred to this specific fault.

6.2.1 principle

The detection method is based on the method FS-MBPC which is also used in the controller. Figure 6.1 explains this detection principle. At any time instant k, the currents flowing through

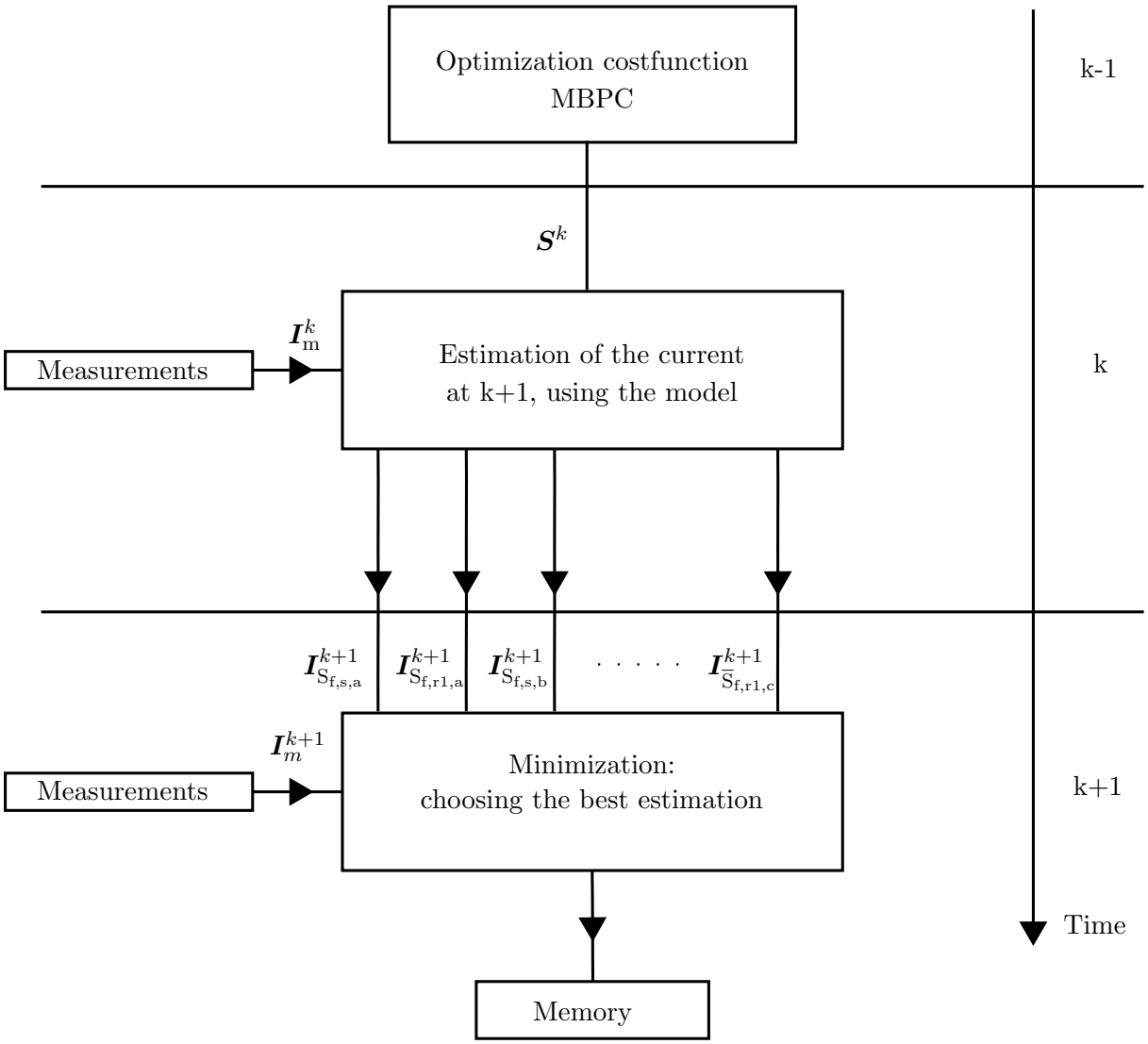

Figure 6.1: The principle of fault-detection

each phase in the stator (subscript s) and inner rotor (subscript r1) are measured. This is denoted as $\boldsymbol{I}^k_{\mathrm{m}}$.

$$\boldsymbol{I}^k_m = [i_{\mathrm{s,a}}(\mathrm{k}),\ i_{\mathrm{s,b}}(\mathrm{k}),\ i_{\mathrm{s,c}}(\mathrm{k}),\ i_{\mathrm{r1,a}}(\mathrm{k}),\ i_{\mathrm{r1,b}}(\mathrm{k}),\ i_{\mathrm{r1,c}}(\mathrm{k})] \tag{6.1}$$

Note that these measurements are transformed to the qd-reference frame, see chapter 4. For further notice, this transformed vector will be denoted as $\boldsymbol{I}^k_{\mathrm{m,qd}}$. Also, the switch-configuration $\boldsymbol{S}^k$ that will be set during time-interval $[k,\ k+1]$ is available. This is the outcome of the

FS-MBPC-algorithm at the previous time-step, as described in chapter 4.

$$\boldsymbol{S}^{\mathrm{k}} = [S_{\mathrm{s,a}}, S_{\mathrm{s,b}}, S_{\mathrm{s,c}}, S_{\mathrm{r1,a}}, S_{\mathrm{r1,b}}, S_{\mathrm{r1,c}}] \tag{6.2}$$

Using the measurements, switch-configuration and controller-model of the PM-EVT, see chapter 4, the currents $\boldsymbol{I}^{k+1}$ at time instant $k+1$ can be estimated. Note that nothing changed, in comparison to the original control-principle. Remark that every estimation is done in the qd-reference frame.

$$\boldsymbol{I}^{k+1} = [I^{k+1}_{\mathrm{s,q}}, I^{k+1}_{\mathrm{s,d}}, I^{k+1}_{\mathrm{r1,q}}, I^{k+1}_{\mathrm{r1,d}}] \tag{6.3}$$

If one switch is broken, the measured currents at $k+1$ are usually different in comparison to the faultless situation. In order to detect this fault, the controller should know what the stator and rotor current will be for each fault situation. In this way, it is possible to compare the currents at time instant $k+1$ with the real measurements, available at that time. During the estimation step at k, the faulty current vectors, that can occur at $k+1$, should be calculated as well. In this set-up, see figure 4.2, twelve IGBT's are used. It is explained in section 4.2, that, the IGBT's in one leg of an inverter, work in a complementary way. This means that 6 IGBT's can get a signal to close, at each control instant. There is no need to change the switching state of each pair of IGBT's, in one inverter leg, every control instant. Once a IGBT is closed, it is mostly for a longer period of time. Consequentially, this specific fault-type can occur in a maximum of 6 IGBT's.

Since the load is highly inductive, the current in a faulty phase cannot immediately drop to zero and another conduction trajectory will be formed. A faulty current-vector can thus be calculated for this specific fault-event. Six of these vectors can be assigned to each inverter, of which three correspond to the failure of the IGBT's ($S_{\mathrm{f},y,x}$), connecting a phase to the positive DC-bus. The other three correspond to the failure of the complementary IGBT's ($\overline{S}_{\mathrm{f},y,x}$).

$$\begin{aligned} \boldsymbol{I}^{k+1}_{\mathrm{S_{f,y,x}}} &= [I^{k+1}_{S_{\mathrm{f},y,x},\mathrm{s,q}}, I^{k+1}_{\mathrm{S_{f,y,x}},\mathrm{s,d}}, I^{k+1}_{\mathrm{S_{f,y,x}},\mathrm{r1,q}}, I^{k+1}_{\mathrm{S_{f,y,x}},\mathrm{r1,d}}] \\ \boldsymbol{I}^{k+1}_{\overline{\mathrm{S}}_{\mathrm{f},p,j}} &= [I^{k+1}_{\overline{\mathrm{S}}_{\mathrm{f},y,x},\mathrm{s,q}}, I^{k+1}_{\overline{\mathrm{S}}_{\mathrm{f},y,x},\mathrm{s,d}}, I^{k+1}_{\overline{\mathrm{S}}_{\mathrm{f},y,x},\mathrm{r1,q}}, I^{k+1}_{\overline{\mathrm{S}}_{\mathrm{f},y,x},\mathrm{r1,d}}] \end{aligned} \tag{6.4}$$

In each equation y denotes the stator s or inner rotor r1 and x indicates the phase a, b or c. These calculated currents can be compared with the actual currents $\boldsymbol{I}^{k+1}_{\mathrm{m,qd}}$ measured at time-instant $k+1$. This explains the usage of the memory block in figure 6.3. In case the model of the electrical system is a perfect replica of the real set-up, the measured current should match one of the calculated current-vectors (faulty **or** faultless). As stated in chapter 5, this is not the case. The controller must thus choose the best estimated current-vector, see figure 6.1, approaching the measurements available at that time. How this is done will be described in the sequel of this chapter. It can be concludeed that the controller will need some memory in order to detect and remember a broken switch.

6.2.2 Prediction of currents in case of a broken IGBT

In the previous section is stated that, the current in the different phases of the stator and rotor will change, in case of a failure of one IGBT. The current can be calculated using the optimal

controller model, described in chapter 4. To do so, the voltage over the load must be known. In a normal operation condition, the output phase voltage is fairly easy to determine, see equation 4.1. However, not the output phase voltage is important, it is the voltage across the load that must be known. This voltage can be calculated by subtracting the voltage between the start point of the load and the neutral clamp of the DC-bus, see equation 4.7. It has been shown that the latter therm is an exact definition of a homopolar voltage component. This can be omitted, see section 3.4.2.

An IGBT is an unidirectional device. It can conduct current only in one direction, unlike a transistor which is bidirectional. Therefore every IGBT is accompanied by a freewheel diode. The purpose of this freewheel diode will be explained in the following example.Suppose that the controller gives a closing signal to the IGBT $S_{s,a}$, while the current in phase a of the stator is negative. This IGBT connects phase a of the stator to the positive half DC-bus, see figure 4.2, and only conducts a current flowing from the positive half DC-bus to that phase. Consequentially, the IGBT will not start conducting in this example. Another path will be formed. The current will flow trough the freewheel diode connecting the phase to the positive DC-bus. This is the only possibility, since the complementary freewheel diode is reverse biased and $\overline{S}_{s,a}$ is in an off-state. Since the load is highly inductive, the current cannot immediately drop to zero. If the freewheel diode would not be present, the current would be interrupted abruptly, resulting in a very high voltage pulse. This mostly results in a complete breakdown of the electrical system.
From the example above, it can be concluded that the voltage over one phase of the load is solely depending on the switching-state, $S_{y,x}$ and the sign of the current, flowing in that phase. A similar event occurs in case an IGBT fails. The reasoning applied above will be used to model these failures.

If a failure of an IGBT occurs. Another path will be formed. Similar to the previous paragraph, this will only depend on the sign of the current and which IGBT is broken. This will be shown in the next two examples, see figure 6.2.

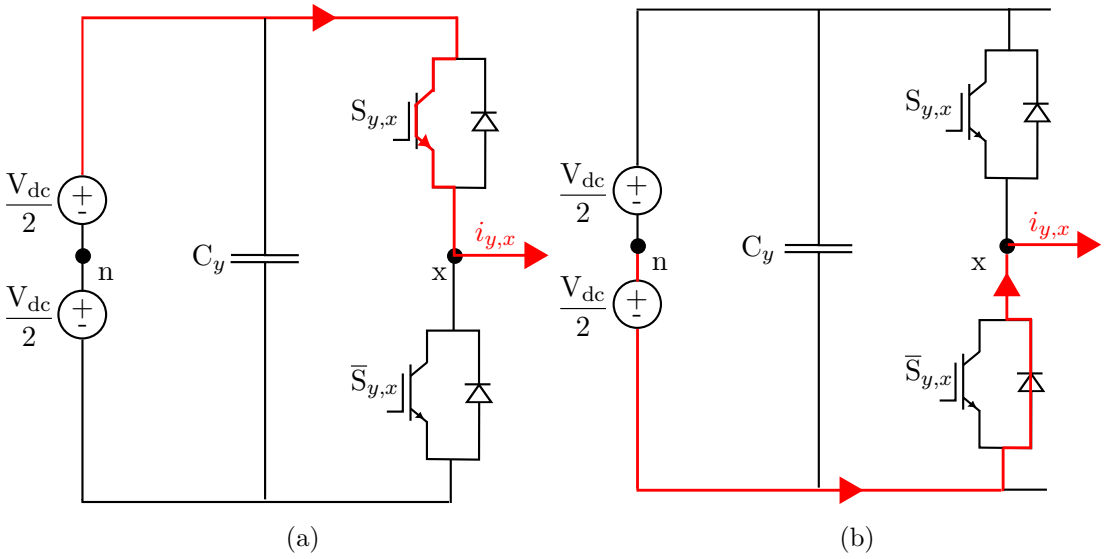

Figure 6.2: Determination of the output phase voltage in case of a broken IGBT

.

In the first case, the IGBT connecting a phase to the positive DC-bus fails while the current is

positive. The faultless situation is described in figure 6.2a. A current will always try to follow a path with minimal resistance. Therefore the current will flow trough the IGBT $S_{y,x}$. Now, in case this IGBT fails, the conduction path trough the affected IGBT cannot be formed. Since the load is highly inductive, the sign of the current cannot suddenly change. Given that the IGBT is an unidirectional device and $\overline{S}_{y,x}$ is in an off-state, the current is forced to flow along the freewheel diode connecting the phase to the negative DC-bus, see figure 6.2b. From this it can be concluded that the output phase voltage, in this situation, will be $-V_{dc}/2$.

A similar reasoning can be applied for the second example. Here it is assumed that the IGBT connecting a phase to the negative DC-bus fails, while the current $i_{y,x} > 0$. In the faultless situation, this current will flow trough the freewheel diode connecting the phase to the negative DC-bus, see figure 6.2b. This is easy to understand, given that the IGBT is an unidirectional device, allowing the current to flow only from collector to emitter. If now IGBT $\overline{S}_{y,x}$ fails, nothing will change. It can be concluded that the output phase voltage in this situation will remain $-V_{dc}/2$ **Remark**: it is assumed that when an internal fault occurs in an IGBT, the corresponding freewheel diode is not damaged and still works. If this would not be the case, then the current is interrupted abruptly resulting in a very high voltage pulse. This mostly results in a complete breakdown of the EVT and other IGBT's in the inverter. A transient surge protector should detect these faults and switch off the affected phase.

Two fault-situations, for one inverter leg feeding a phase, are already explained. Since each leg contains 2 IGBT's and the current can be either positive or negative, two other faults situations may occur. So there are four different fault-situations for one inverter leg:

1. $S_{y,x}$ is broken and $i_{y,x} > 0$.
2. $S_{y,x}$ is broken and $i_{y,x} < 0$.
3. $\overline{S}_{y,x}$ is broken and $i_{y,x} > 0$.
4. $\overline{S}_{y,x}$ is broken and $i_{y,x} < 0$.

Situation 1 and 3 are already described above. A similar reasoning can be applied for the remaining two. An overview of each fault situation is given in figure 6.3.

The output phase voltage in each fault-situation can perfectly be calculated off-line and subsequently stored in the controller as a look-up table. It can be seen from figure 6.3 that the output phase voltage in one leg of the inverter is solely determined by the sign of the current and can be written as

$$v^k_{y,xn} = S_{dc,y,x}\frac{V_{dc}}{2} \tag{6.5}$$

where $S_{dc,y,x}$ is

$$S_{dc,y,x} = sign(i_{y,x}) \tag{6.6}$$

This formula can easily be used in an FPGA. The only thing that needs to be explained, is what happens if zero crossing of the current takes place when a fault occurs. Consider situation 1 (fault in S_{pj} and $i_{pj} > 0$). Just before the zero crossing, the current will flow along the freewheel diode connecting the negative DC-bus to phase A. Next, at zero-crossing, the diode

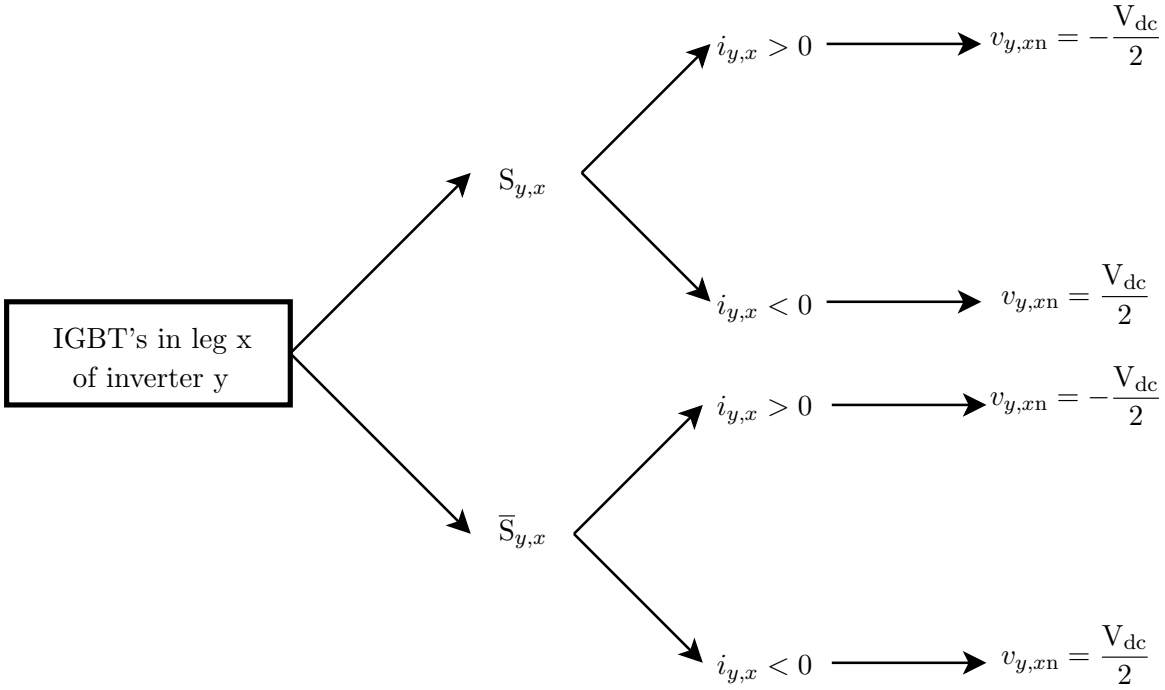

Figure 6.3: Overview: phase voltage when an IGBT fails.

will stop conducting the current. This means that the line is not connect to a DC-bus any more as the current cannot flow trough the corresponding IGBT. This means that the current will remain zero during the remaining part of the time-interval. This phenomenon will occur at every fault-situation where a zero-crossing of the current occurs.

6.2.3 Detection of a broken switch

In the previous section, a model of each specific fault-situation has been derived, allowing the controller to calculate the faulty current-vectors, see equation 6.4. These vectors are then stored within the memory, until the next measurement instant. In general: The estimations of the current at $k+1$ are calculated at k and stored in the memory under this form:

$$\boldsymbol{E} = \begin{bmatrix} I^{k+1}_{\mathrm{S_{f,s,a},s,q}} & I^{k+1}_{\mathrm{S_{f,s,a},s,d}} & I^{k+1}_{\mathrm{S_{f,s,a},r1,q}} & I^{k+1}_{\mathrm{S_{f,s,a},r1,d}} \\ I^{k+1}_{\mathrm{\overline{S}_{f,s,a},s,q}} & I^{k+1}_{\mathrm{\overline{S}_{f,s,a},s,d}} & I^{k+1}_{\mathrm{\overline{S}_{f,s,a},r1,q}} & I^{k+1}_{\mathrm{\overline{S}_{f,s,a},r1,d}} \\ I^{k+1}_{\mathrm{S_{f,s,b},s,q}} & I^{k+1}_{\mathrm{S_{f,s,b},s,d}} & I^{k+1}_{\mathrm{S_{f,s,b},r1,q}} & I^{k+1}_{\mathrm{S_{f,s,b},r1,d}} \\ \vdots & \vdots & \vdots & \vdots \\ I^{k+1}_{\mathrm{S_{f,r1,a},s,q}} & I^{k+1}_{\mathrm{S_{f,r1,a},s,d}} & I^{k+1}_{\mathrm{S_{f,r1,a},r1,q}} & I^{k+1}_{\mathrm{S_{f,r1,a},r1,d}} \\ \vdots & \vdots & \vdots & \vdots \\ I^{k+1}_{\mathrm{s,q}} & I^{k+1}_{\mathrm{s,d}} & I^{k+1}_{\mathrm{r1,q}} & I^{k+1}_{\mathrm{r1,d}} \end{bmatrix} \tag{6.7}$$

Each row of the matrix $\boldsymbol{E} \in \mathbb{R}^{13\times 6}$ contains the estimated current in each phase of the stator (column 1-3) and inner rotor (column 4-6). The first 12 rows contain the estimations in case of a broken IGBT (1-6: PEC s and 7-12: PEC r1). The last row contains the estimation in the faultless situation.

Based on a comparison between the estimated current vectors and the measured current vector $\boldsymbol{I}_{\mathrm{m}}^{k+1}$, the controller must detect whether or not a fault occurred. Since cross-effects and saturation are incorporated into the controller model, the failure of each IGBT will affect every current component in both the stator and inner rotor. In order to determine the best estimation, each component of the estimated current vector $\boldsymbol{I}^{k+1}$, determined at time k, must be compared with each component of the measurement vector $\boldsymbol{I}_{\mathrm{m,qd}}^{k+1}$ at $k+1$. Based on these differences, the best estimation must be chosen. This can be done by using the norm of the difference between these 2 vectors.

The norm-difference between each relevant estimation of the current-vector and the measured current-vector is defined as follows:

$$||\boldsymbol{E}_{i,*} - \boldsymbol{I}_{\mathrm{m,qd}}^{k+1}|| = \sqrt{|I_{\mathrm{S_{f,y,x}},s,q}^{k+1} - I_{\mathrm{s,q}}(k+1)|^2 + |I_{\mathrm{S_{f,y,x}},s,d}^{k+1} - I_{\mathrm{s,d}}(k+1)|^2 + |I_{\mathrm{S_{f,y,x}},r1,q}^{k+1} - I_{\mathrm{r1,q}}(k+1)|^2 + |I_{\mathrm{S_{f,y,x}},r1,d}^{k+1} - I_{\mathrm{r1,d}}(k+1)|^2} \tag{6.8}$$

Here, $\boldsymbol{E}_{i,*}$ denotes the i-th row of the matrix. In this way the information from all phases in the system is used, in order to choose the best estimation, which has the minimal norm-difference. As state above, not every fault-situation is of importance. Only those where the corresponding IGBT has received a pulse while in an off-state, meaning that it should create a conduction channel, have to be considered. Therefore the **irrelevant** fault-situations are not calculated at the previous time instant. The corresponding rows of the fault matrix $\boldsymbol{E}$ are empty. **Remark** that for certain fault-situations this norm-difference will not be different from the faultless case. This should be clear from the example described in the previous section, where $\overline{\mathrm{S}}_{y,x}$ was broken and $i_{y,x} > 0$. This must be taken into account when determining the best estimation.

This is simulated in Simulink. The existing model used to control the EVT has been extended with a fault-detection system based on the method described above. The rows in the matrix $\boldsymbol{E}$, containing irrelevant information, are filled with infinite current-values. On the base of the calculated norms, see equation 6.8, the best estimation can be chosen. The best one, being the smallest, corresponding to a certain situation, gets a penalty. The outcome of this minimization step is a vector $\boldsymbol{F}^k \in \mathbb{R}^{13\times 1}$ with 13 elements. The first 12 correspond to a fault occurring in each IGBT. The 13th element corresponds to the faultless case. All places in this vector are filled with zeros, except for the place corresponding to the best estimated situation. this place contains one. $\boldsymbol{F}^{\mathrm{k}}$ is then stored in the memory of te controller. The designation 'penalty' is a bit confusing, as in a faultless case the norm corresponding with this situation should get a penalty. In case the smallest norm-difference is the same for multiple situations, and the faultless situation is amongst them, then the faultless estimation will get the benefit of the doubt. Otherwise no penalty will be assigned.

To prove that this method is valid, two fault situations were simulated. The initial operation conditions are the same the first test case described in chapter 5.

1. The case where $S_{s,a}$ fails.
2. The case where $\overline{S}_{r1,b}$

The distributions of penalties assigned to each fault-situation over a certain time-period are shown in figure 6.4. The fault occurs after 0.15 seconds. It can be seen that the proceeding fault-situation are certainly noticed by the controller.

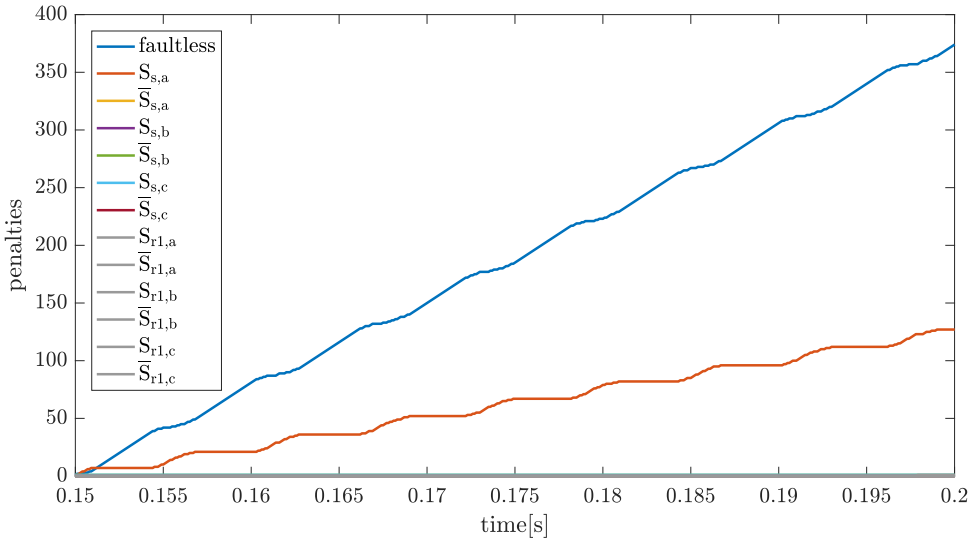

(a) fault on $S_{s,a}$

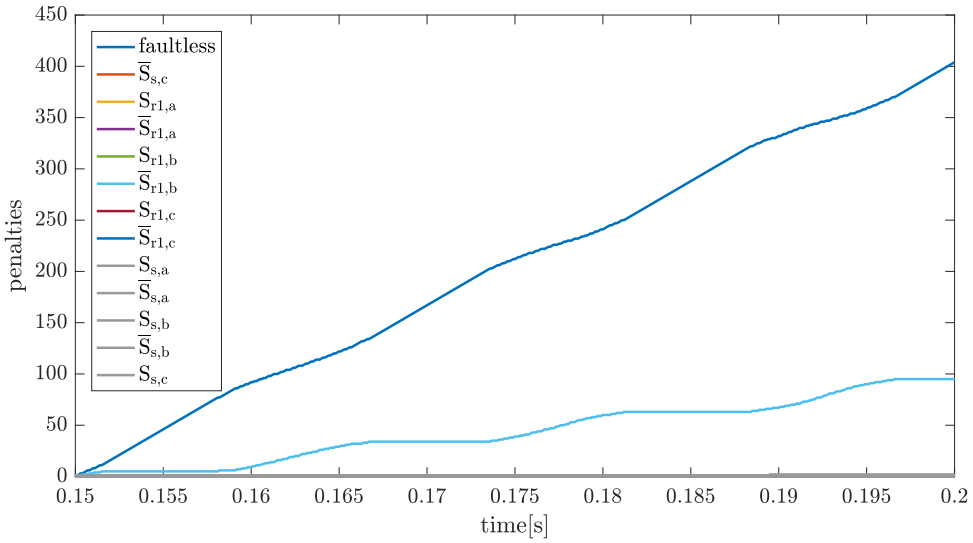

(b) fault on $\overline{S}_{r1,b}$

Figure 6.4: Distribution penalties per IGBT, fault simulated from 0.1s

The built-up of penalties is similar for both faults. There is a sequence of an increase in the number of penalties followed by a period where no penalties are assigned to the fault-situation. This can be explained using figure 6.5, where the stator current in the first fault-situation is shown.

It can be seen that the electrical system has difficulties conducting a positive current $i_{s,a}$ in phase a if $S_{s,a}$ fails. When $i_{s,a} > 0$ and $S_{s,a}$ is broken, a positive output phase voltage cannot be applied to this system, see figure 6.2. Therefore $i_{s,a}$ cannot increase. Unlike the case where the current

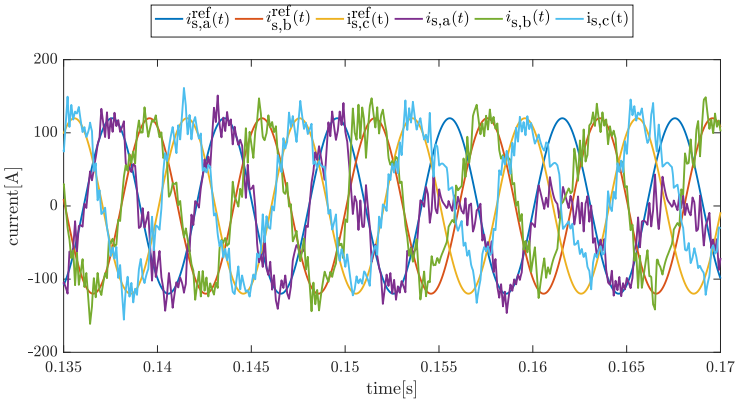

Figure 6.5: Phase currents in the stator when $S_{s,a}$ fails

$i_{s,a} < 0$. then, the broken IGBT $S_{s,a}$ cannot be used, since this device is unidirectional. The current would flow trough the freewheel diode, which is assumed not to broken. No difference can thus be noticed between the fault- and faultless situation. In these cases the controller always gives the advantage the faultless situation. This explains the sequencing of the increase in penalties. Note that the period of each part of the sequence is the same. The total period, in figure 6.4a, approximately equals 0.006 s, which is also the period of the rotational speed of the air gap field seen from the stator. The total period, in figure 6.4b equals 0.015 s , which is the period of the rotational speed of the air gap field, seen from the rotor. In this example, the latter period is the largest since the rotational speed of the air-gap field seen from the inner rotor , being $(2500-1500)N_p$ rpm, is lower then the rotational speed seen from the stator, which is $2500N_p$ rpm.

6.2.4 Making a decision

Now the controller is able to detect a faulty situation, it is able to make a decision. Close attention is required for this last step. In the previous chapter, a controller-model has been derived. Although, this model is more detailed then classic models, this is still an approximation of the real model. The temperature impact, for example, has not been taken into account. This has already been described in section 5.2.1. In addition, the inaccuracy of measurements itself will affect the estimation in a similar way and also leads to a bigger deviation between the estimations and measurements, see section 5.2.2.

Although this detection method works fine in the ideal simulation, in reality this will not be the cases. Decide that a switch is broken, based on one penalty assignment to a faulty situation, is very unwise. Therefore some measures will be taken such that a fault-situation is not mistakenly detected.

First, the accuracy range of the measurements must be taken into account. In the description of this detection-method, it is already stated that current-vectors in different fault situations don't differ much from each other. This will result in almost the same norm-difference. It seems dull to choose the best out of these two estimates if their norm-difference is smaller then the accuracy range of the measurements. In this case a conclusion will not be made. Provisionally it will be assumed that:

- If the faultless situation is among this group of norm-differences, the advantage will be given to the faultless situation.

- If the faultless situation is not among this group of norm-differences, no detection can occur and no penalty will be assigned to any situation.

In the simulations done in SIMULINK, it is assumed that the accuracy range of the current measurements is up to one decimal place, meaning that the minimal difference should be higher then 0.1.

Next there will be dealt with the measurement errors, see section 5.2.2, and the use of a simplified model. Inaccuracies measuring voltage, current and rotational speed will have an influence on the estimations of the current at the next time instant. Also, the controller model is still an approximation of the real system. For example, temperature variations aren't taken into account, see section 5.2.1. This can also have an impact on the reliability of the estimations. it follows that it can occur that an erroneous penalty is assigned to a faulty situation. Therefore the controller will only decide that a fault-situation occurred when multiple penalties are assigned to the proceeding fault-situation.

It was opted in [8], to do this by introducing a moving average and a threshold. A Moving Average MA takes into account the previous penalties assigned to each fault situation. Figure 6.6 explains this principle.

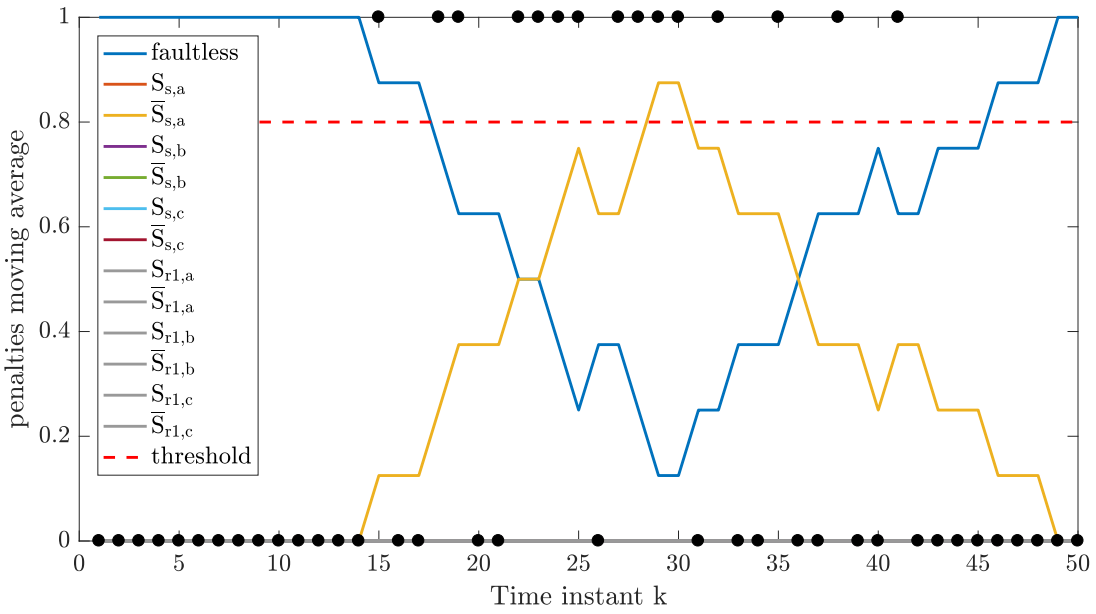

Figure 6.6: Fault-detection using moving average and threshold

Here a fault in IGBT $\overline{S}_{s,a}$ at time-instant k=0 is introduced. It is created using the simulation model. The initial operation conditions are the same as the first test case, described in chapter 5. The outcome of each minimization step is a vector $\boldsymbol{F}^{k}$. The previous vectors $\boldsymbol{F}^{k-i}$ are also available in the memory of the controller. When a moving average with a window size n is used, the controller will take into account the $n-1$ previous penalty vectors.

$$\boldsymbol{F}^{k}_{\mathrm{MA},n} = \frac{1}{n}\sum_{i=0}^{n\text{-}1} \boldsymbol{F}^{\mathrm{k\text{-}i}} \tag{6.9}$$

Each element of $\boldsymbol{F}^{k}_{\mathrm{MA},n}$ contains a averaged penalty point,between 0 and 1, corresponding to each fault situation. This is calculated at every control instant, see figure 6.6. In this figure, the window size is set to be 8. Only if the averaged penalty reaches a certain threshold value, the controller will decide that a certain IGBT is broken. The black dots, in figure 6.6 represent the penalties assigned to the real fault situation at each time instant.

The question remains what should be chosen for the threshold and window of the MA. It is desired that the fault-decision system works in every operation condition. It can be seen from figure 6.4, that the period, over which penalties are assigned to a certain fault-situation, depends on the rotational speed of the air gap field. If the EVT outer rotor speed is low, the period over which penalties are assigned to the proceeding fault-situation in the stator, is longer. This makes it much easier for the controller to make a decision. For high speeds, the period will be much smaller, making it more difficult. A similar reasoning can be applied for the detection of a fault at the inner rotor. The moving average window and the threshold value should be fine-tuned such that a fault-decision system works at any speed. It is also important that a fault can be detected when the EVT works in every operation condition. This requires a good model and has already been discussed in chapter 4.

Based on simulations, the optimal values of the moving average window and the threshold are determined. As a test case, the first case described in chapter 5 is used. Only now the outer rotor speed will be varied from 500 rpm tot 4500 rpm. The failure of IGBT $\overline{\mathrm{S}}_{\mathrm{s,a}}$ is introduced at 0.15 s. Depending on the window size and the outer rotor speed, the MA penalty point and the first time this happens will change. This was tested for a window size varying from 2 to 20 in steps of 1. The results are given in the figure 6.7.

It can be seen from figure 6.7a, that the first time a maximum MA penalty point occurred, approximately equals 0.035 seconds, no variations can be noticed there. Based on figure 6.7b, it can be deduced that the maximum averaged penalty point is much lower for higher speeds. Setting the threshold value low, can be a solution. However lowering the threshold value, causes an increase in the chance that, the controller mistakenly decides that a faulty situation occurred. Another solution would be lowering the moving average window. But this results in the same disadvantage. These two values cannot be chose independently from each other. The MA window and threshold should be high enough, such that a reliable decision-system is created. It can be seen in figure 6.7b that for a MA window between 6 and 8, a smaller variation in the maximum averaged penalty, can be noticed. A minimal variation is determined for a MA window size 7. In that case, the minimal averaged penalty point equals 0.7143

Note that this theoretical analysis. A further fine-tuning must happen, based on actual measurements. In this master dissertation, it is opted to use a MA window of 7 and a threshold value of 0.67. The threshold value is lowered, since in reality, other disturbances can decrease the accuracy of this system.

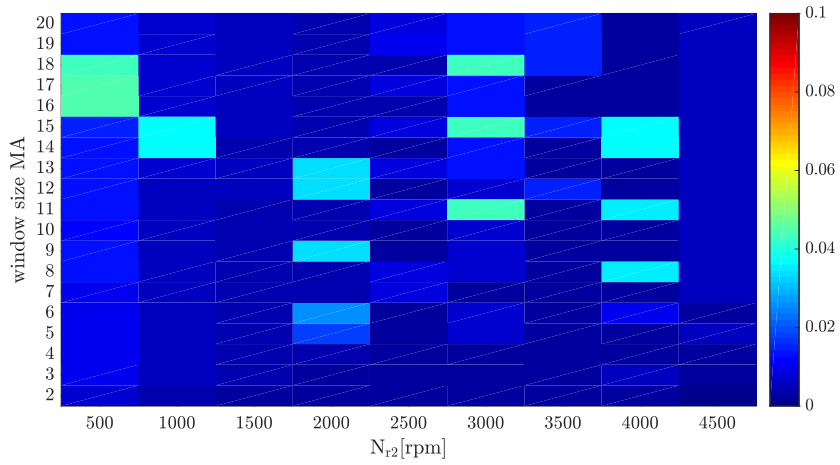

(a) Decision time

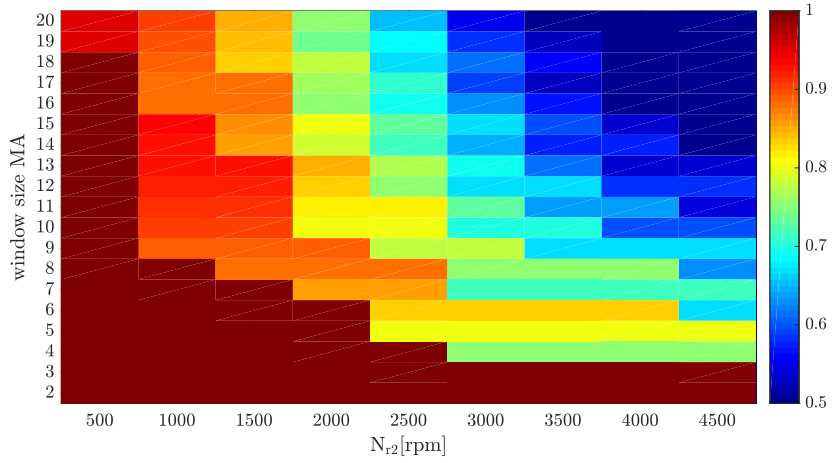

(b) maximum averaged penalty point

Figure 6.7: Simulation: determination of the optimal MA window size and threshold value

6.2.5 Distributed assignment

It was shown in section 6.2.2 that multiple fault-situations can result in the same estimated current-vector. When the detection method described section 6.2.3 is used, there is one case where no detection could be done by the controller. This occurs when two norm-differences, corresponding with a certain fault-situation, deviate less then the accuracy range of the measurements from each other. A lot of information can get lost then. This can be solved by using a distributed assignment method. The principle is as follows:

- If n fault-situations result in a norm-difference smaller then the accuracy range of the current measurements and the faultless situation is not included, then each fault-situation will be assigned a penalty value of 1/n.

- If the same situation occurs and the faultless situation is included, then the faultless situation will get more credibility. A penalty of 0.5 will be assigned to the faultless situation and 0.5/(n-1) will be assigned to the other (fault) situations.

In this way, more information is extracted from the measurement. This is added to the detection-algorithm described in the previous section. This was again simulated for the same fault-situation as before. The result is shown in figure 6.8.

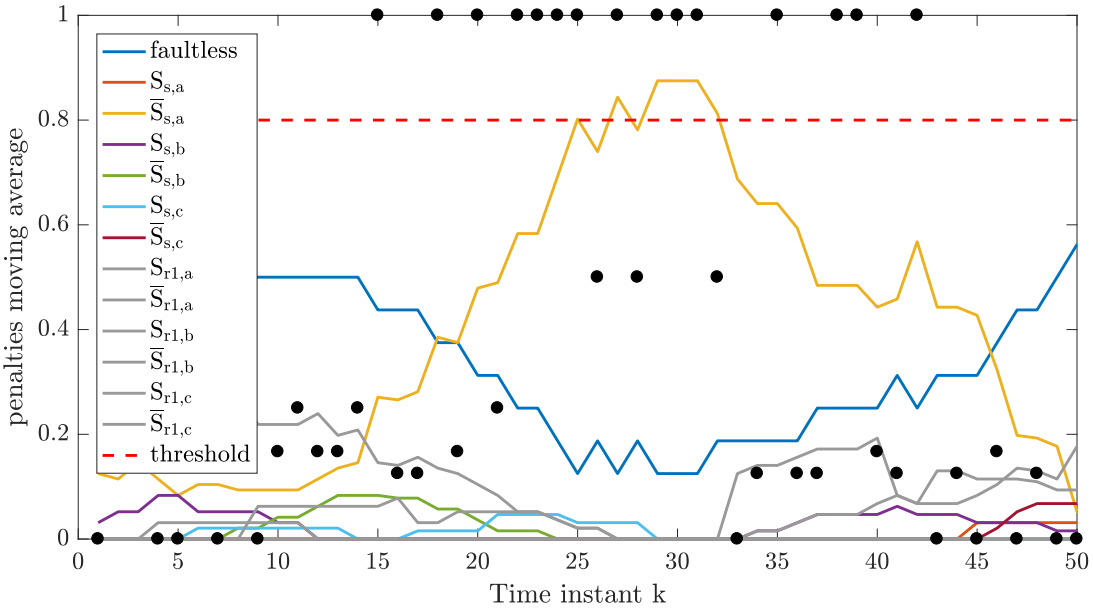

Figure 6.8: Fault-detection using moving average, threshold and distributed assignment

From this figure it is clear that including this distributed assignment has a positive influence on the decision method. In the previous case (see figure 6.6), there were some cases in which no fault was detected. This is not wrong, but since the estimation in the fault-situation and faultless case are the same, no point is assigned to the faultless case. Using distributed assignment, this is not the case. Half a point is assigned to the faulty-situation when k=26. The controller knows that something could be wrong with the IGBT $\overline{S}_{s,a}$. This will result in a more robust fault-detection. Note that the averaged penalty assigned to the fault-less case is now only 0.5. The reason for this is that, there are always multiple fault-situations rseulting in the same estimated current vector.

The same question also rises here: what is the optimal MA window and threshold value? This is again determined based on the simulations executed in the previous section. When distributed assignment is used, the number of possible values for the averaged penalty point highly increases. At every time-instant, a penalty point between 0 and 1 can be assigned to a situation. However, in the previous case, there where only 2 possibilities: 0 or 1. In order to make it possible to compare both decision methods, the averaged penalty points are distributed among classes with an accuracy of 0.05. For example, suppose the following averaged penalty points are measured: [0.56 0.61 0.58 0.535 0.58]. These are then classified as follows:

The first time is then chosen to be the earliest time that a number within a certain class occurred. The results are shown in figure 6.9. The averaged first time,the maximum averaged penalty point is detected, equals approximately 0.035 s. this more or less constant. Similar conclusions, as in section 6.2.4, can be derived from this figure. Only now, the variation for the maximum averaged penalty point is lower for a MA widwow between 6-9. A minimum variation can be noticed for a MA window of 8. In this case the minimal averaged penalty point equals 0.7858. This is significantly higher in comparison to the previous section. Based on these simulations,

class	values	occurrence	average
$[0.5 - 0.55]$	$[0.535]$	$[1]$	0.535
$[0.55 - 0.6]$	$[0.56\ 0.58]$	$[1\ 2]$	$\frac{0.56 + 0.58 \cdot 2}{3} = 0.573$
$[0.6 - 0.65]$	$[0.61]$	$[1]$	0.61

Table 6.1: Classification of averaged penalty point.

the optimal MA-window an threshold value is chosen to be, respectively, 8 and 0.695.

This proves that distributed assignment significantly improves the decision-method. the MA-window and threshold value, can be increased. In this way, the chance that the controller decides a false fault-situation occurred, decreases. Again, remark that this is only a theoretical analysis. A further fine-tuning must happen, based on actual measurements.

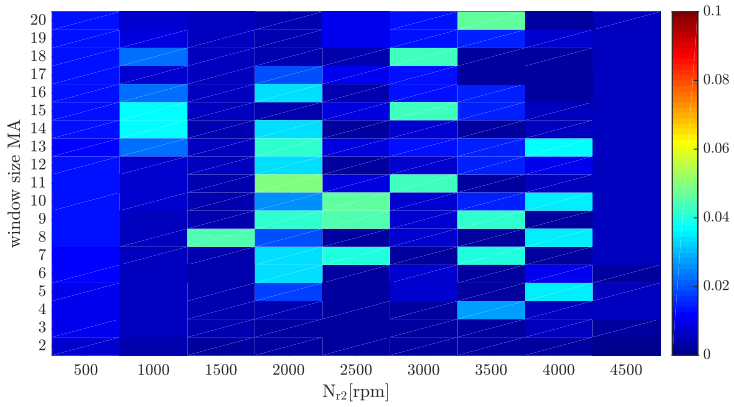

(a) Decision time

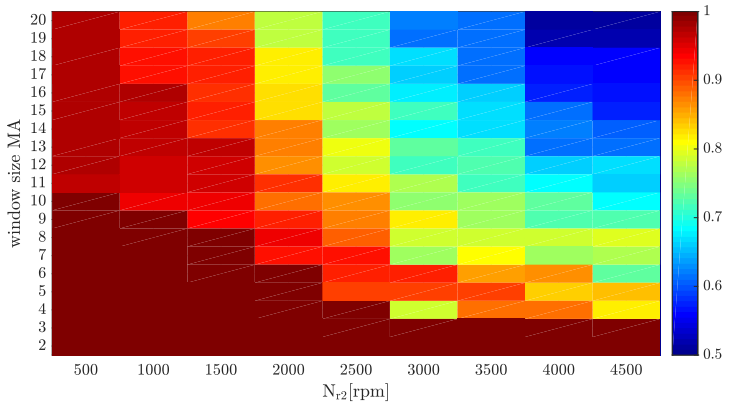

(b) maximum averaged penalty point

Figure 6.9: Simulation: determination of the optimal MA window size and threshold value when distributed assignment is used.

6.3 Fault-tolerant operation mode

In the previous section a detection/decision-method was derived. However, the decision only is not enough. As stated in the introdcution, minor adjustments to the electrical system, ensure the operation of the system when this typical fault occured. This will be derived in general, for any three phase system, supplied by a 2L-VSI . There are 4 options:

1. Connect the phase, fed by the inverter-leg in which the fault occurred, to the positive DC-bus. This can be done by closing the complementary IGBT continuously.
2. Connect the phase, fed by the inverter-leg in which the fault occurred, to the negative DC-bus. This can be done by closing the complementary IGBT continuously
3. Connect the phase fed, by the inverter-leg, in which the fault occurred to the center tap of the source. This point is in reality a fictive point. but by using 2 capacitors, it can be created. Note that the capacity voltage should remain constant here in order to guarantee that this is really the center tap. It is also possible to use 2 identical batteries. In a HEV, this is fairly easy as the battery exists of several layers which can be separated easily. In order to do this, extra switching elements must be installed between each inverter-leg and this point.
4. Decouple the corresponding phase and continue the operation with only 2 phases.

This last option is, of course, in extremity, but can be used in the case where the freewheel diode is damaged as well. The first 3 cases will be investigated. In order to say something about these solutions a space vector representation will be used. Each switching combination, with the corresponding output phase voltage of each phase, is then represented by one space vector. From this single vector, the instantaneous output phase voltages corresponding to this switch-configuration can be derived. In a faultless situation, the space vector representation of each switching-state, corresponding to one of the used inverters, is shown in figure 6.10. This is already partially explained in section 4.2 an 5.4. Note that there are 2 zero space-vectors, named passive vectors. These vectors represent the case where all phases are connected to either the positive or negative DC-bus. In order to be able to supply a symmetrical three phase load with a symmetrical sinusoidal three-phase voltage, i.e. being able to create a rotating field, a rotating vector V must exist, see figure 6.10. At each controller-instant, the controller decides wich switch-configuration will be set, in order to approximate this rotating vector as close as possible. The maximum power deliverable to the system, is depending on the maximum voltage vector, the system is able to supply continuously. When Space Vector Modulation is used, this maximum average voltage deliverable to the system is the radius of the inscribed circle in the hexagon [19].

$$\underline{V}_{max} = \frac{V_{dc}}{\sqrt{3}} \tag{6.10}$$

This can be increased slightly if harmonics are considered as well. The same maximum value can be reached by a FS-MBPC-controller, if the switching frequency is chosen to be high.

In case the faulty phase is connected to either the positive or negative DC-bus, the number of space-vectors will be reduced to three space vectors. In that case the output phase voltage of one inverter leg is fixed, such that half of the possible space vectors, shown in figure 6.10, disappear. In that case the rotating reference vector cannot be followed by the controller, since the voltage

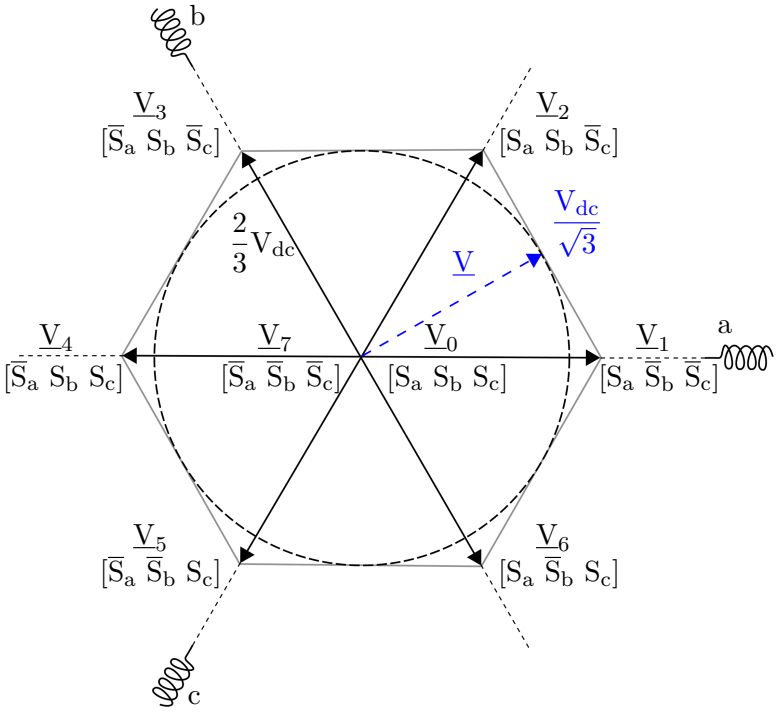

Figure 6.10: Space Vector Representation: faultless situation

in one phase is either continuously positive or negative. It is thus impossible to create a rotating field. Neither of these proposals is a good solution.

Last the connection to the center-tap will be discussed. A connection of one inverter-leg to the center-tap means that output phase voltage of this leg equals zero **but** this does not mean that the voltage over the corresponding winding equals zero. It is explained in section 4.2 that, the voltage between the star point of the stator (or inner rotor) and the neutral clamp (= center tap) of the DC-bus is equal to the average of the three output phase voltages of each inverter. If now, an inverter leg is connected to the center-tap, the voltage across the corresponding winding will be equal to the average output phase voltages of each inverter-leg. Since the two IGBT's of the affected IGBT are not used any more, only 4 different switching states remain. These switching states are listed in table 6.2, when the inverter-leg feeding phase a of the load is broken. The voltage over the load and voltage between the startpoint of the load and the center tap, are calculated based on respectively equations 4.7 and 4.8.

S_a	S_b	S_c	v_{an}	v_{bn}	v_{cn}	v_{on}	v_{ao}	v_{bo}	v_{co}
CT	0	0	0	$\frac{-V_{dc}}{2}$	$\frac{-V_{dc}}{2}$	$\frac{-V_{dc}}{3}$	$\frac{V_{dc}}{3}$	$\frac{-V_{dc}}{6}$	$\frac{-V_{dc}}{6}$
CT	1	0	0	$\frac{V_{dc}}{2}$	$\frac{-V_{dc}}{2}$	0	0	$\frac{V_{dc}}{2}$	$\frac{-V_{dc}}{2}$
CT	0	1	0	$\frac{-V_{dc}}{2}$	$\frac{V_{dc}}{2}$	0	0	$\frac{-V_{dc}}{2}$	$\frac{V_{dc}}{2}$
CT	1	1	0	$\frac{V_{dc}}{2}$	$\frac{V_{dc}}{2}$	$\frac{V_{dc}}{3}$	$\frac{-V_{dc}}{3}$	$\frac{V_{dc}}{6}$	$\frac{V_{dc}}{6}$

Table 6.2: Voltage in case of a failure of an IGBT in leg a of the inverter

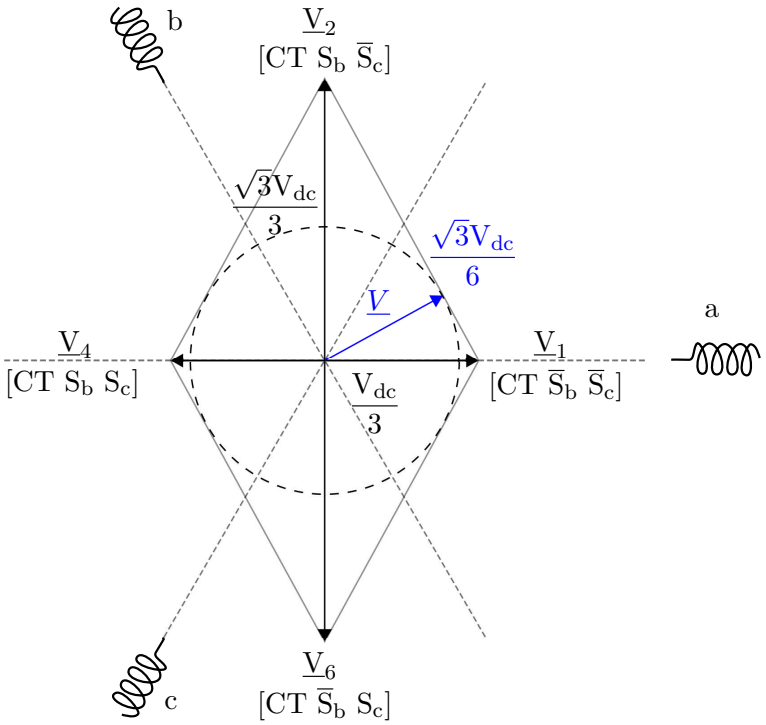

Figure 6.11: Space Vector Representation: faultless situation

The space vector representation in case of a connection of phase A to the center-tap is shown in figure 6.11. From this it can be derived that a fault-tolerant operation is possible when connecting the affected phase to the center-tap. The 4 remaining space vectors are oriented in such a way that a rotating field can be created. The hexagon indicating the maximum voltage vector at each orientation, is now a rhombus. The maximum amplitude of the rotating space vector is limited to the radius of the inscribed circle of the rhombus. The inradius of a rhombus with diagonal p and q can be calculated as follows:

$$V_{max} = \frac{p \cdot q}{2\sqrt{p^2 + q^2}} = \frac{\frac{2}{3}V_{dc}\frac{2\sqrt{3}}{3}V_{dc}}{2\sqrt{(\frac{2}{3}V_{dc})^2 = (\frac{2\sqrt{3}}{3}V_{dc})^2}} = \frac{\sqrt{3}}{6}V_{dc} \tag{6.11}$$

This is significantly lower then in the faultless case. So, depending on the speed of the rotor, the maximum power, or torque, will be significantly lower in comparison to the faultless case. Note, there are no passive vectors now. If the desired reference voltage vector has an amplitude, lower then V_{max}, the inverter will try to achieve this, by only using these 4 space vectors. This will result in a higher MSE.

A similar derivation can be executed for the failure of an IGBT in an inverter leg, feeding phase b or c. THe result is just a rotated version of the space vector diagram, depicted in figure 6.11.

It is stated before that the maximum deliverable torque will decrease, depending on the rotational speed of the rotor, or in this case, of both rotors. Similarly as in section 5.4, the maximum deliverable torque can be determined theoretically. This is then validated by simulation. The results for the stator and rotor torque, are shown in, respectively, figure 6.12a and 6.12b

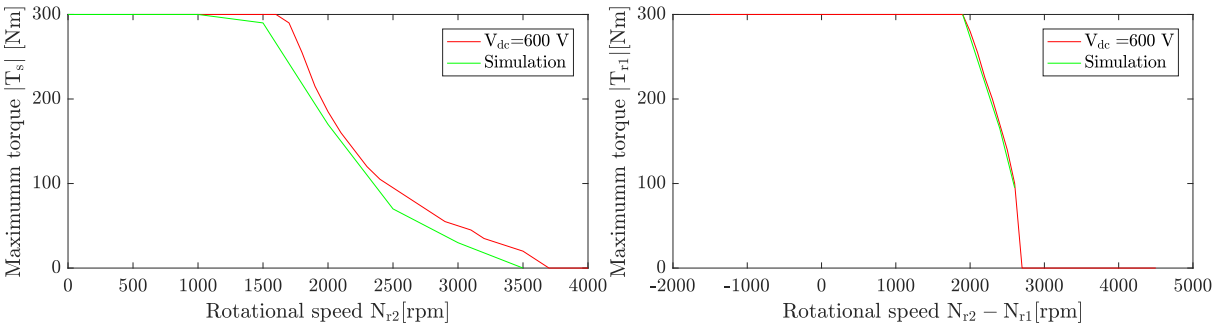

(a) Stator (b) Rotor

Figure 6.12: Simulations: maximal deliverable torque in fault tolerant operation.

6.4 Simulation

The fault-detection, -decision system and fault tolerant mode are now brought together. If a fault occurs, the fault-detection system, using distributed assignment, will assign penalties to the proceeding fault-situation. If the MA penalty increases above 0.695 the controller will decide that a fault occurred. The controller then gives a close signal to the switch between the infected inverter-leg and the center-tap of the source. In this way a fault tolerant mode is activated. In order to test this controller, the system is completely implemented in matlab. To ensure that this simulation approximates the reality as close as possible, measurement errors and resistor variations are included as well. The first testcase described in chapter 5 is used again. First a fault will be simulated in the stator. More specific in $S_{s,b}$. This fault occurs at 0.15 seconds. Since the current is controlled, the q- and d-axis current will be shown, see figure 6.15a and 6.15b. The estimations and predictions done by the controller, are also shown.

In figure 6.13, the MA penalty, assigned to each fault situation, is shown from the moment $S_{s,b}$ breaks down. Only 0.002 seconds later, the controller decides a fault occurred in $S_{s,b}$. This very fast. The time over which an unbalanced current is supplied to the PM-EVT is then minimized, see figure 6.14. Afterwards, the controller signals the switch, between the center-tap and inverter-leg b of the PEC s, to close. A fault tolerant operation mode is activated. The controller knows this. From figures 6.15a and 6.15b, it can be seen that the controller is still able to make correct estimations of the q- and d-axis current. However, the reference value cannot be approximated any more. This can also be noted when examining the abc-currents, see figure 6.14. The current in phase b cannot drop to -120 A, but is stuck at -95 A. This is due to the fact that the desired stator torque, being 100 Nm, is larger then the maximum torque deliverable at this speed, in fault tolerant mode, see figure 6.12a. Therefore, the wanted stator torque is lowered to 60 Nm. In that case, the controller is able to approximate the reference current value. This proves that the statements, derived above, are valid.

Until now, nothing is mentioned concerning a fault in the rotor. However, this entire system should be able to detect a fault in the PEC feeding the inner rotor. To prove this, a fault will be simulated at $\overline{S}_{r1,b}$. The same test case is used.

It can be seen from figure 6.16, that the controller now takes much longer to decide whether or not a the proceeding fault situation occurred. Only after 0.045s, the controller decides that IGBT $\overline{S}_{r1,b}$ failed. Note that the controller senses that something is wrong. The moving averaged

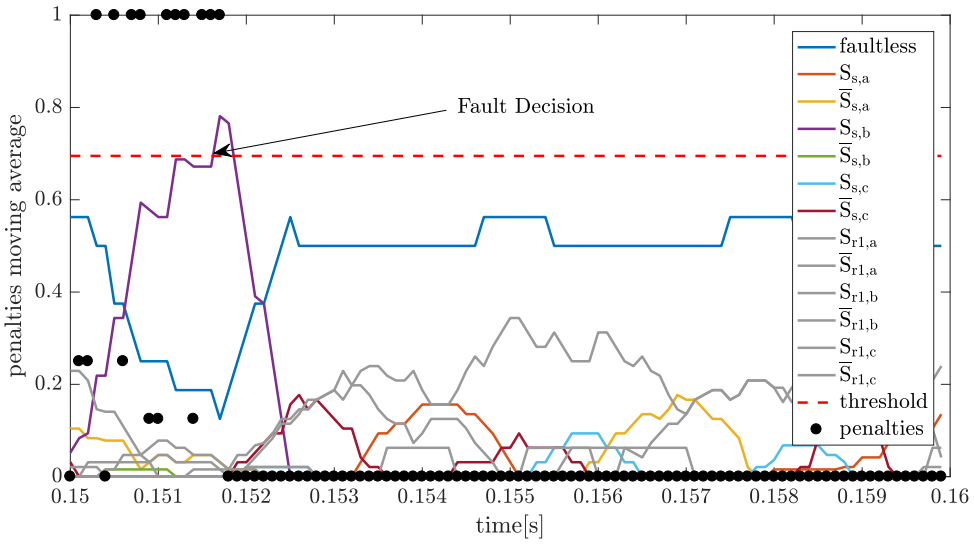

Figure 6.13: Penalty assignment: fault in stator $S_{s,b}$

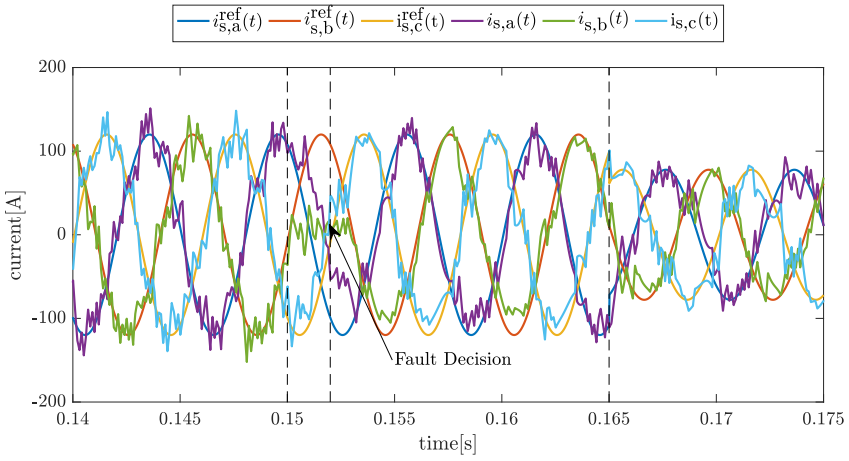

Figure 6.14: abc-currents: fault in stator $S_{s,b}$

penalty point assigned to th proceeding faul-situation remains on average 0.5 . The reason for this is the high ripple present on the current, see figure 6.17. It has been shown in section 6.2.3 that, a faulty situation can result in the same prediction as for the faultless situation. Due to the high ripple, the current in phase b will fluctuate around zero, if the reference current in that phase is negative. So, depending on the current sign, no difference will be noted between the faulty and faultless situation. Therefore the controller will assign less penalties to the faulty situation, this can also be seen from figures 6.18a and 6.18a. These figures show the measured q- and d-axis current in the inner rotor and, how it is estimated and predicted by the controller. The time-window of both figures is set, such that the reference value of the current in the affected phase is negative. The controller doesn't know yet that a fault occurred. From these figures, it can be seen that controller makes accurate estimations about half of the time. This will result in a lower moving averaged penalty assigned to the proceeding fault-situation. Note that if distributed assignment were not used, the moving averaged penalty would be much lower, since most of the time the controller will give advantage to the faultless situation. If the controller indeed decides that a fault occurred, the system will change to a fault tolerant operation mode,

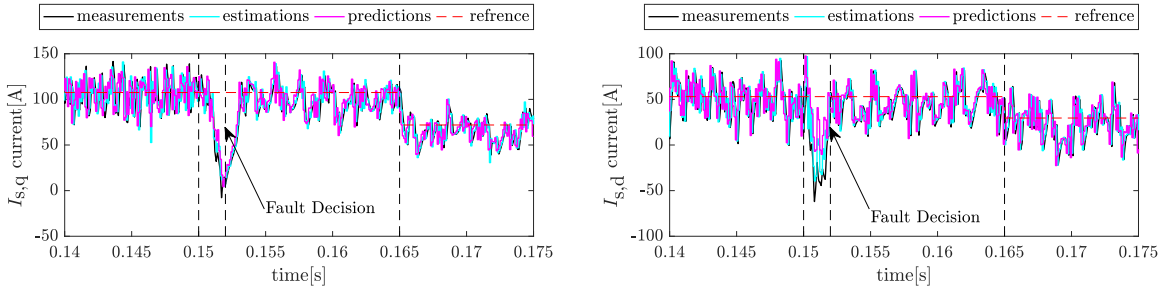

(a) q-axis stator current

(b) d-axis stator current

Figure 6.15: Simulations: qd-current

to ensure continuous operation. The controller has no problem to regulate the currents at the desired value, see figure 6.17. This because the desired inner rotor torque is lower then the maximum deliverable torque at the current speed difference between both rotor.

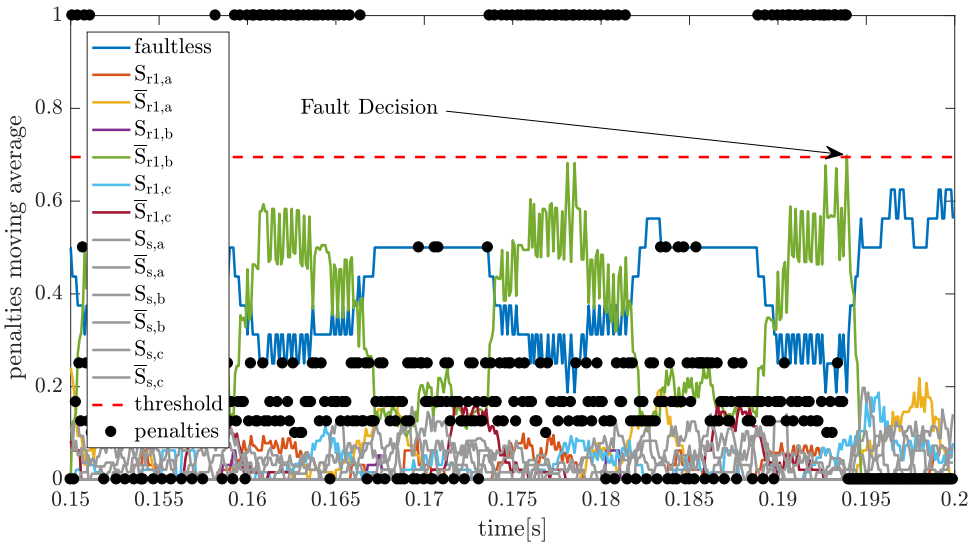

Figure 6.16: Penalty assignment: fault in rotor $\overline{S}_{r1,b}$

The cause of this high ripple in the current is dual. Firstly, the inner rotor yoke is mostly saturated. Therefore, the inductance parameters will be lower in comparison to those in the stator. Due to the high DC-bus voltage, this will result in a higher ripple. Secondly, the inner rotor back-emf is much lower, since the rotational speed of the air gap field is determined by the speed difference between both rotors. Again, due to the high DC-bus voltage, this will result in an even higher ripple. A possible solution would be to lower the DC-bus voltage, in that case the ripple will be lower. This has also been simulated. the same fault at $\overline{S}_{r1,b}$ was introduced under the same operation conditions, only now the DC-bus voltage is 500 V in stead of 600 V. The moving averaged penalty over time and the abc-current in the inner rotor is shown in respectively figures 6.19 and 6.20. the ripple on the current is significantly lower then the case where the DC-bus-voltage is 600V, see figure 6.17. After 0.013 seconds, the controller decides that a $\overline{S}_{r1,b}$ failed. This is much lower then the case where the DC-bus-voltage is 600V, see figure 6.16. This proves the statements derived above and the functioning of the entire fault-decision system.

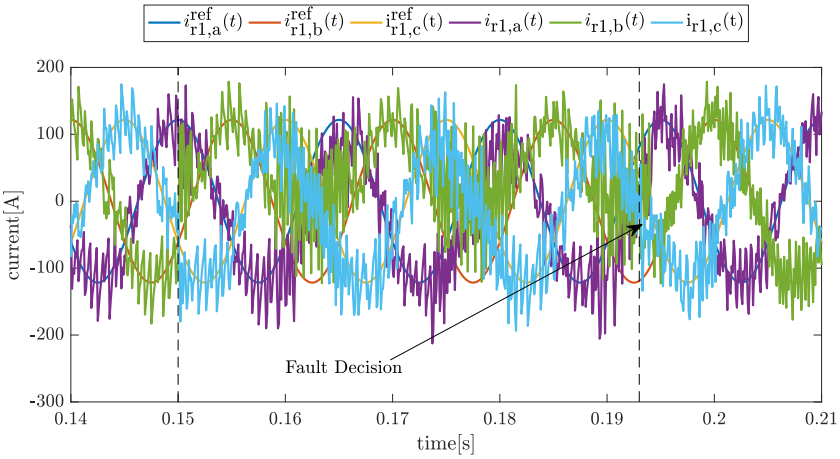

Figure 6.17: abc-currents: fault in rotor $\overline{S}_{r1,b}$

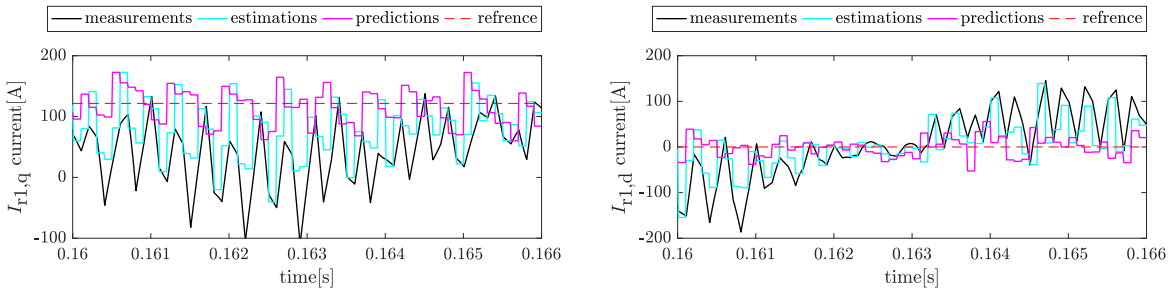

(a) q-axis inner rotor current

(b) d-axis inner rotor current

Figure 6.18: Simulations: maximal deliverable torque in fault tolerant operation.

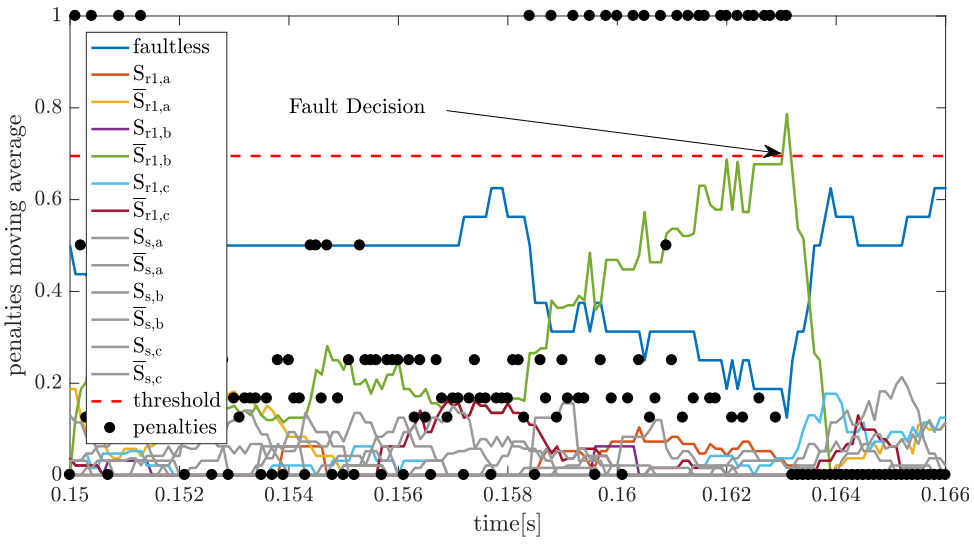

Figure 6.19: Penalty assignment: fault in rotor $\overline{S}_{r1,b}$

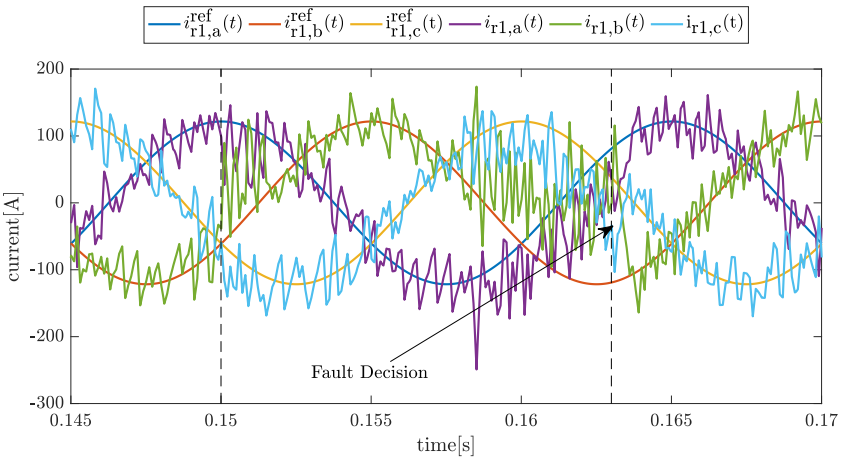

Figure 6.20: abc-currents: fault in rotor $\overline{S}_{r1,b}$

Chapter 7

conclusion

In this master dissertation, different faults have been discussed and analysed. It has been shown that a model based fault-detection is the most promising method. However, a model based fault diagnosis also requires an accurate model. Based on FEM-calculations a detailed model is derived. Though, due to practical reasons, this model cannot be used as a controller model. The model is simplified and discretized in such a way that an optimal performance is obtained for every operation state. This was done having in mind that the model had to be implementable in a FPGA. A response analysis has been executed and the performance of the MBPC-controller is compared with a PI-controller. It has also been shown that speed of both rotors determines the maximum stator and inner rotor torque.

Next, a fault-diagnosis system has been derived for open-switch failures. The presented method uses distributed assignment, in order to extract more information from the measurements. The controller will only decide that a fault occurred after multiple penalty assignments. To this end, a MA and threshold are used. The optimal values are determined such that the diagnosis system works in every operation point. This was done based on simulations. It has been shown that the detection method works fine for stator faults. Due to the high DC-bus voltage, inner rotor faults are more difficult to detect. Since the inner rotor back-EMF is lower, there is no need for such a high DC-bus voltage. It is opted to install a chopper between the battery and PEC connected to the inner rotor sliprings.

Last, a fault-tolerant operation mode has been derived for this specific fault-type. By connecting the affected inverter leg to the neutral clamp of the DC-bus, it is possible to create a rotating field. In this way, a continuous operation has been preserved

Future work

Experimental verification

It is mentioned multiple times that these theoretical calculations need experimental validations. Although some measures haven been taken to make the simulation approximating reality, experimental verification is needed. The parameters of the controller-model can be further fine-tuned. the same holds for the fault diagnosis system. However, the MA window and the threshold value

are '*only*' determined based on simulations. Remark that it has been taken into account that the controller and fault-diagnosis system is implementable in an FPGA. It is therefore perfectly possible to do the experiments.

Cost-function optimization

A controller model able to make an accurate estimation of the current has been derived. However, the cost-function is not optimized. The performance of the controller may be increased in this way.

Fault-detection

It has been shown in chapter 2, that their are still other faults that may occur in the system. For many of these faults, model based detection methods already exist. These methods are perfectly applicable here as well and can be used to improve the reliability of the PM-EVT.

Appendix A

Flux linkage and Cross-effects

A.1 $\Psi_{s,d} = f(I_{s,q}, I_{s,d}, I_{r2,d}, I_{r1,q}, I_{r1,d})$

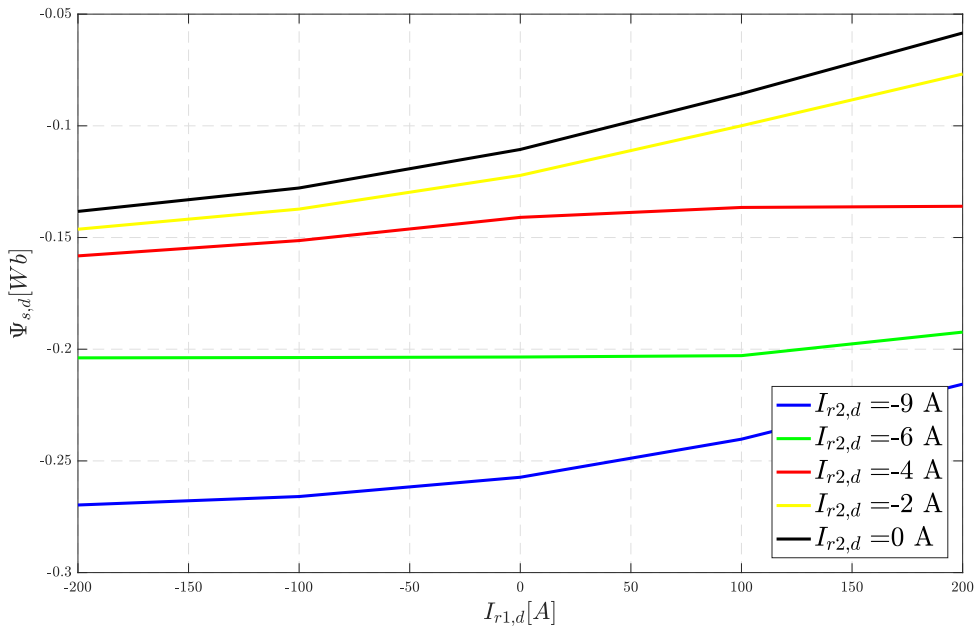

Figure A.1: FEM-calculations: the d-axis stator flux $\Psi_{s,d}$ as a function of the d-axis inner rotor current $I_{r1,d}$ with parameter: the field current $I_{r2,d}$

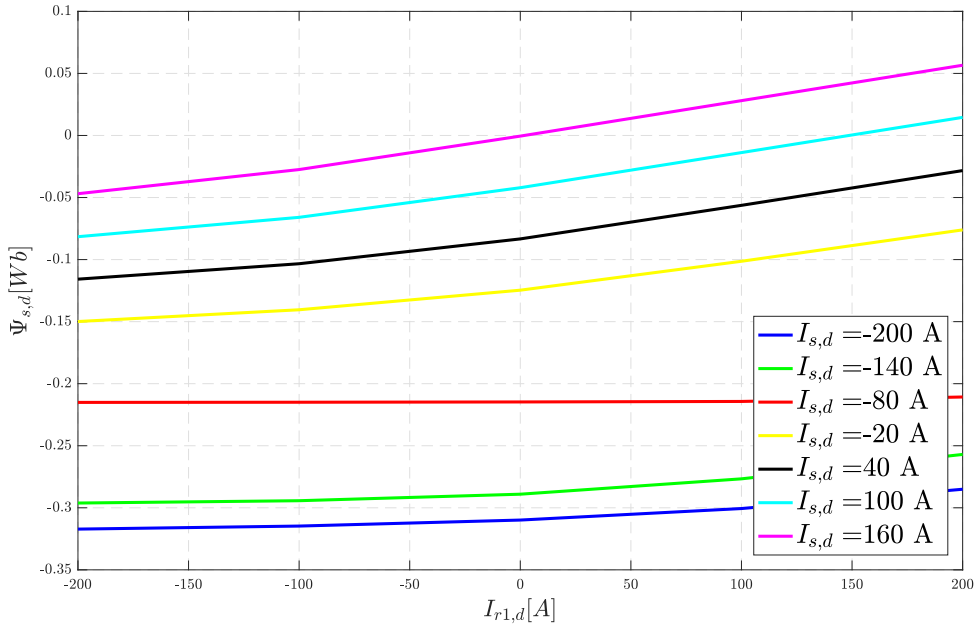

Figure A.2: FEM-calculations: the d-axis stator flux $\Psi_{s,d}$ as a function of the d-axis inner rotor current $I_{r1,d}$ with parameter: the d-axis stator current $I_{s,d}$

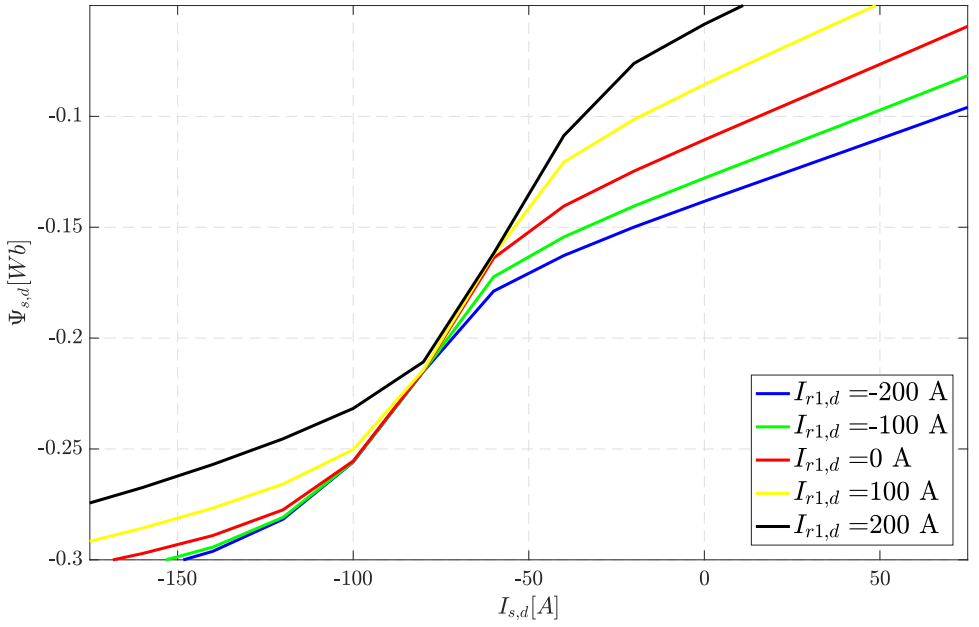

Figure A.3: FEM-calculations: the d-axis stator flux $\Psi_{s,d}$ as a function of the d-axis inner rotor current $I_{s,d}$ with parameter: the d-axis stator current $I_{r1,d}$

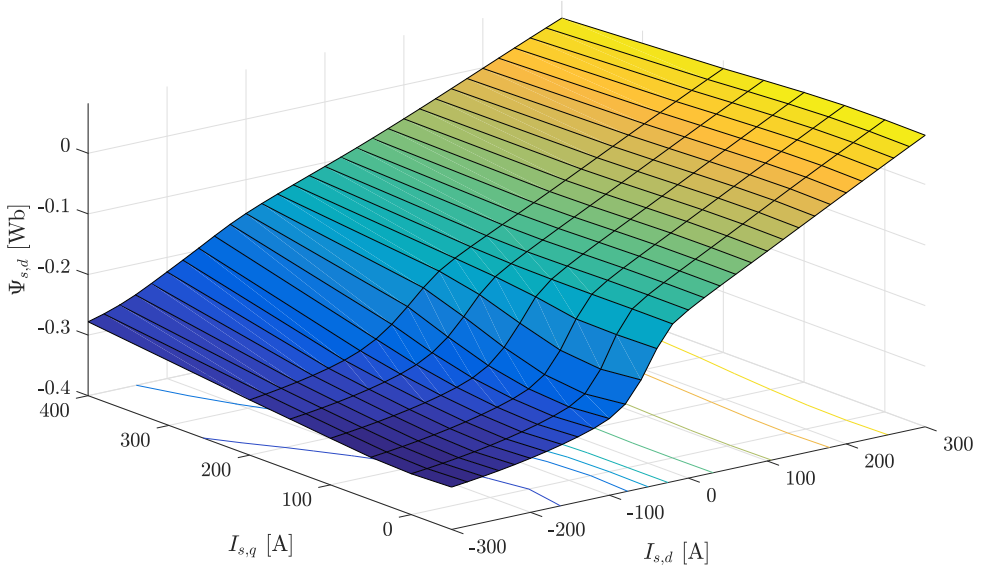

Figure A.4: FEM calculations: the d-axis stator flux $\Psi_{s,d}$ as a function of the stator current $I_{s,d}$ & $I_{s,q}$. The field current $I_{r1,d}$ equals -2 A and there is no inner rotor current.

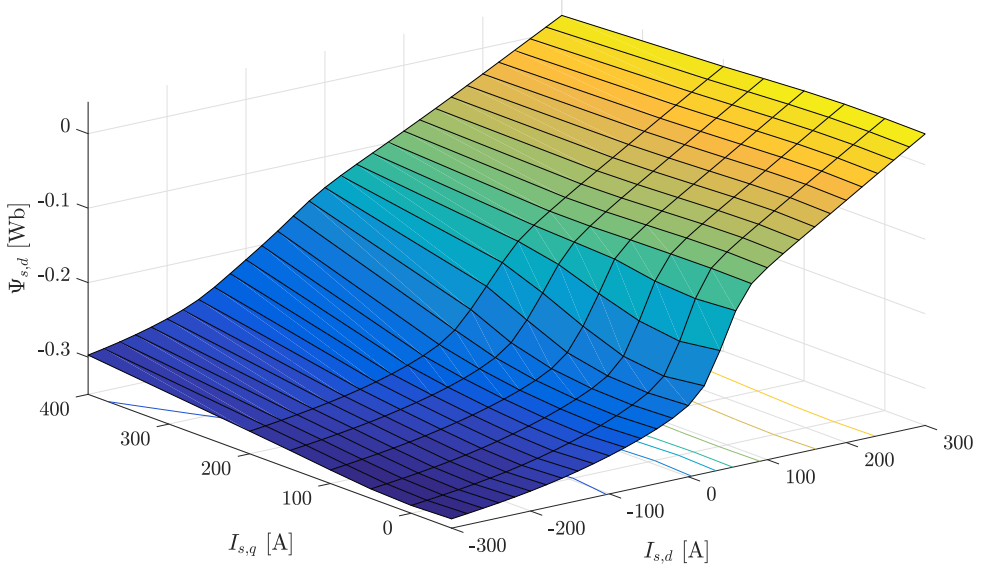

Figure A.5: FEM calculations: the d-axis stator flux $\Psi_{s,d}$ as a function of the stator current $I_{s,d}$ & $I_{s,q}$. The field current $I_{r1,d}$ equals -9 A and there is no inner rotor current.

A.2 $\Psi_{s,q} = f(I_{s,q}, I_{s,d}, I_{r2,d}, I_{r1,q}, I_{r1,d})$

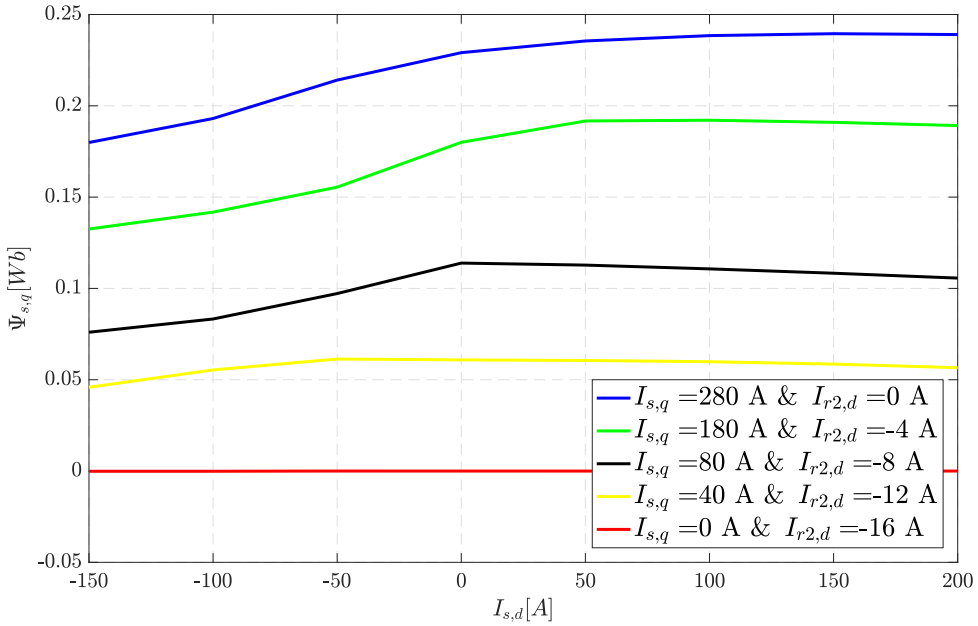

Figure A.6: FEM calculations: the q-axis stator flux $\Psi_{s,q}$ as a function of the d-axis stator current $I_{s,d}$ with parameters: the q-axis stator current $I_{s,q}$ and the field current $I_{r2,d}$

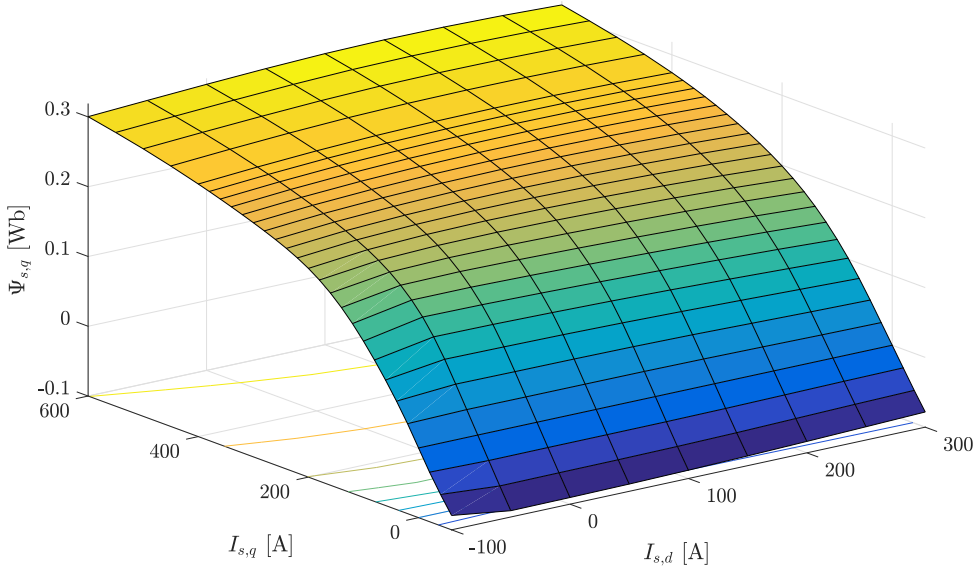

Figure A.7: FEM calculations: the q-axis stator flux $\Psi_{s,q}$ as a function of the stator current $I_{s,d}$ & $I_{s,q}$. The field current $I_{r2,d}$ equals 0 A and there is no inner rotor current.

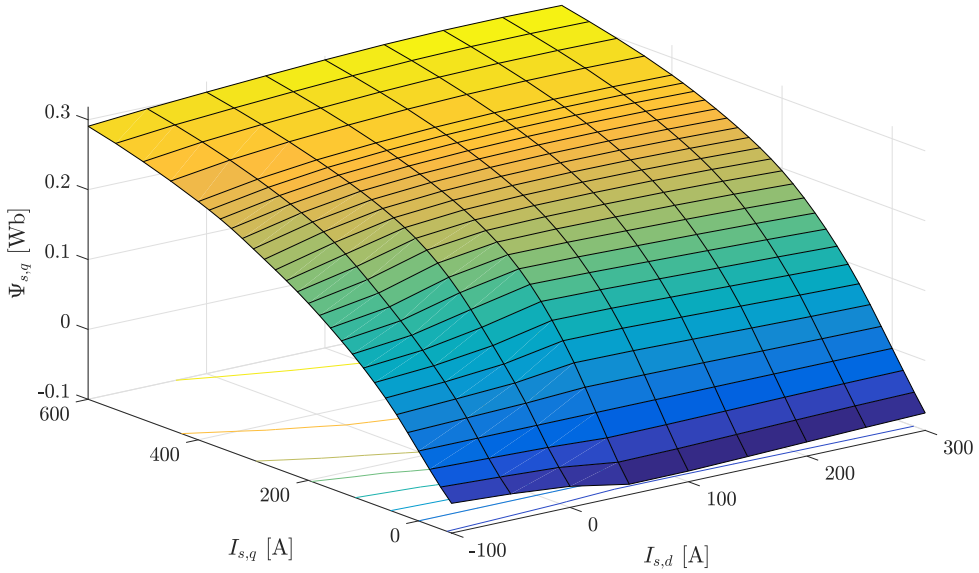

Figure A.8: FEM calculations: the q-axis stator flux $\Psi_{s,q}$ as a function of the stator current $I_{s,d}$ & $I_{s,q}$. The field current $I_{r2,d}$ equals -8 A and there is no inner rotor current.

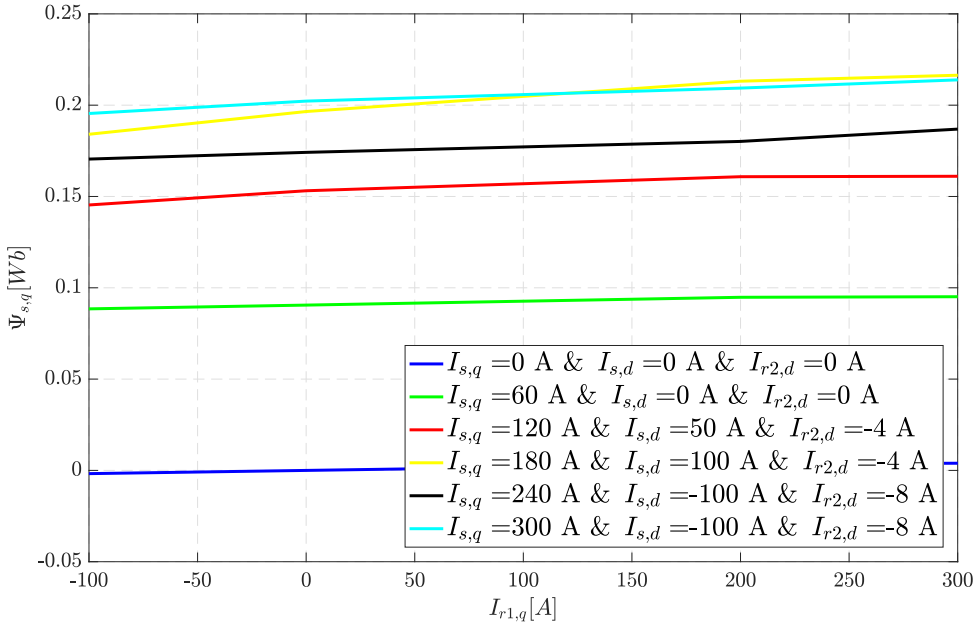

Figure A.9: FEM calculations: the q-axis stator flux $\Psi_{s,q}$ as a function of the q-axis inner rotor current $I_{r1,q}$ with parameters: the stator current $I_{s,q}$ & $I_{s,d}$ and the field current $I_{r2,d}$

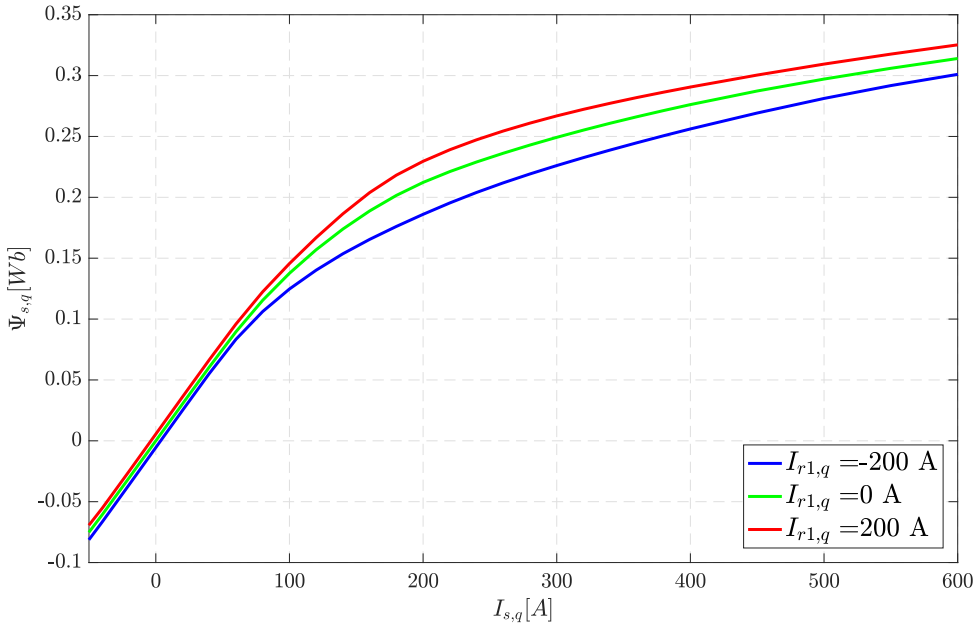

Figure A.10: FEM calculations: the q-axis stator flux $\Psi_{s,q}$ as a function of the q-axis stator current $I_{s,q}$ with parameter: the q-axis inner rotor current $I_{r1,q}$. All the other current components are zero.

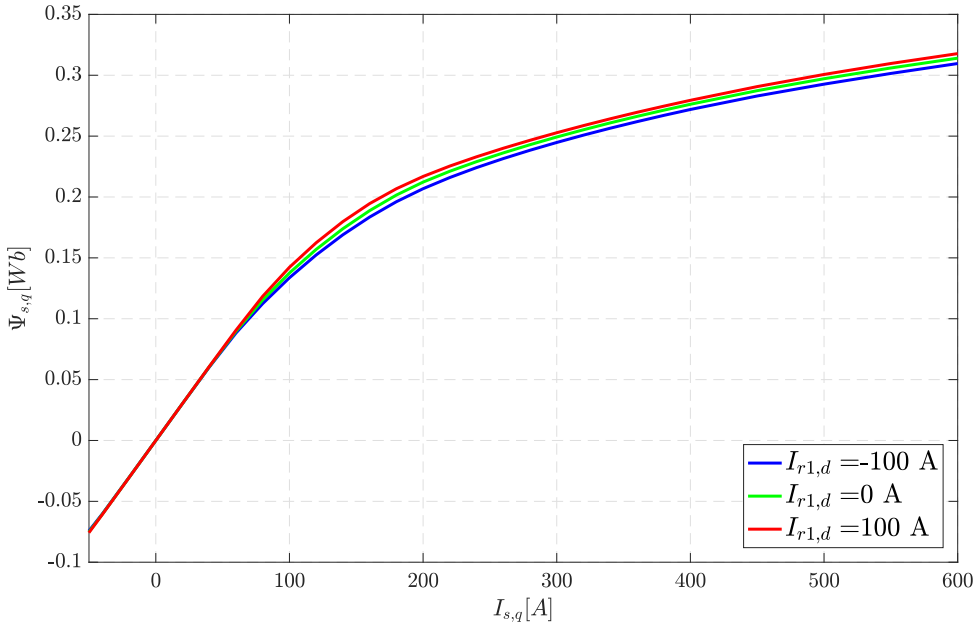

Figure A.11: FEM calculations: the q-axis stator flux $\Psi_{s,q}$ as a function of the d-axis stator current $I_{s,q}$ with parameters: the d-axis inner rotor current $I_{r1,d}$. All the other current components are zero.

A.3 $\Psi_{r1,d} = f(I_{s,q}, I_{s,d}, I_{r2,d}, I_{r1,q}, I_{r1,d})$

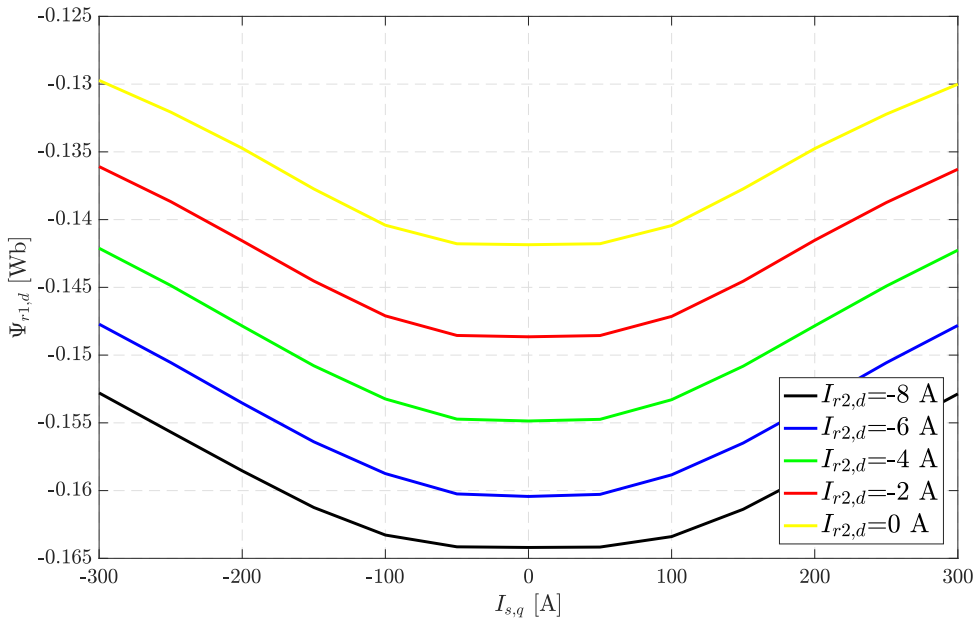

Figure A.12: FEM calculations: the d-axis inner rotor flux $\Psi_{r1,d}$ as function of the q-axis inner rotor current $I_{r1,q}$ with parameter: the field current $I_{r2,d}$. The d-axis stator current $I_{s,d}$ equals 50 A and the inner rotor current $I_{r1,}$.is zero.

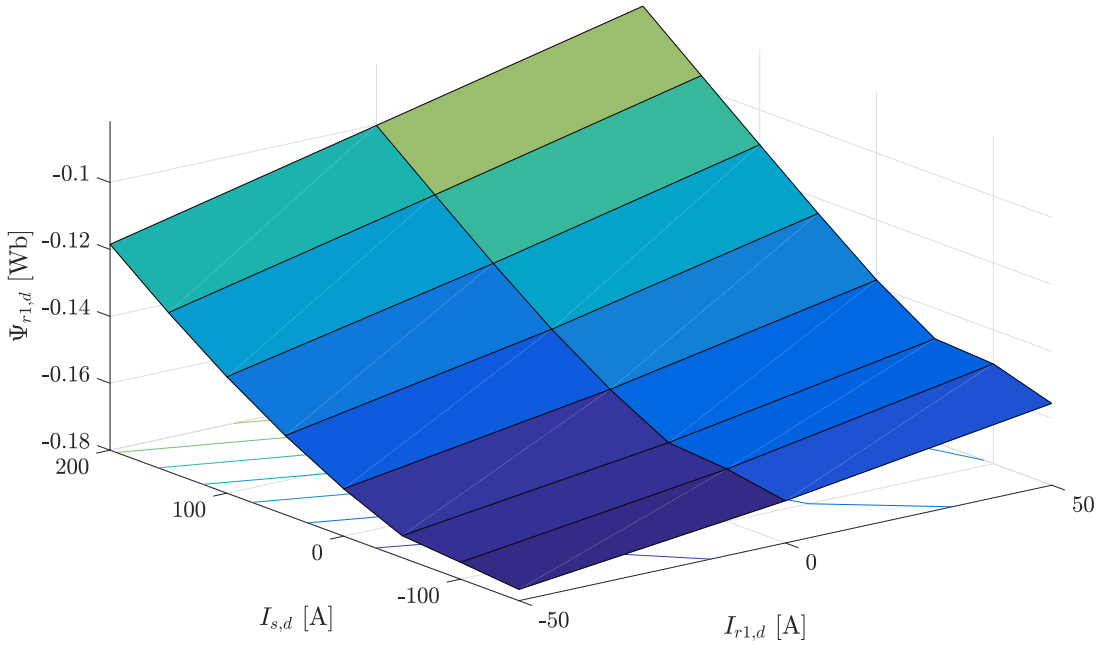

Figure A.13: FEM calculations: the d-axis inner rotor flux $\Psi_{r1,d}$ as function of the d-axis inner rotor current $I_{r1,d}$ and d-axis stator current $I_{s,d}$. All the other current components are zero.

A.4 $\Psi_{r1,q} = f(I_{s,q}, I_{s,d}, I_{r2,d}, I_{r1,q}, I_{r1,d})$

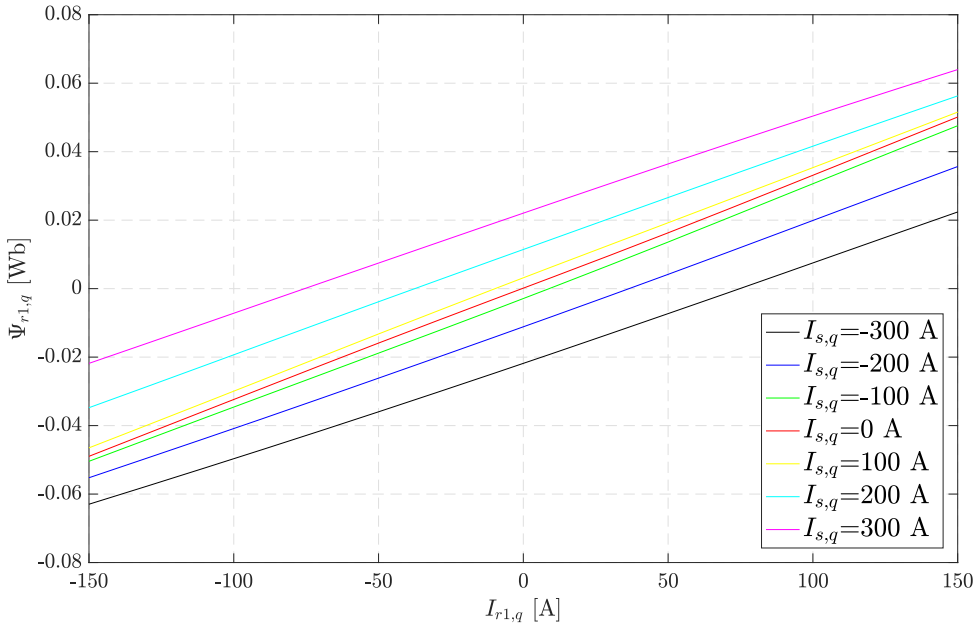

Figure A.14: FEM calculations: the q-axis inner rotor flux $\Psi_{r1,q}$ as function of the q-axis inner rotor current $I_{r1,q}$ with parameter: the q-axis stator current $I_{s,q}$. All other current components are zero.

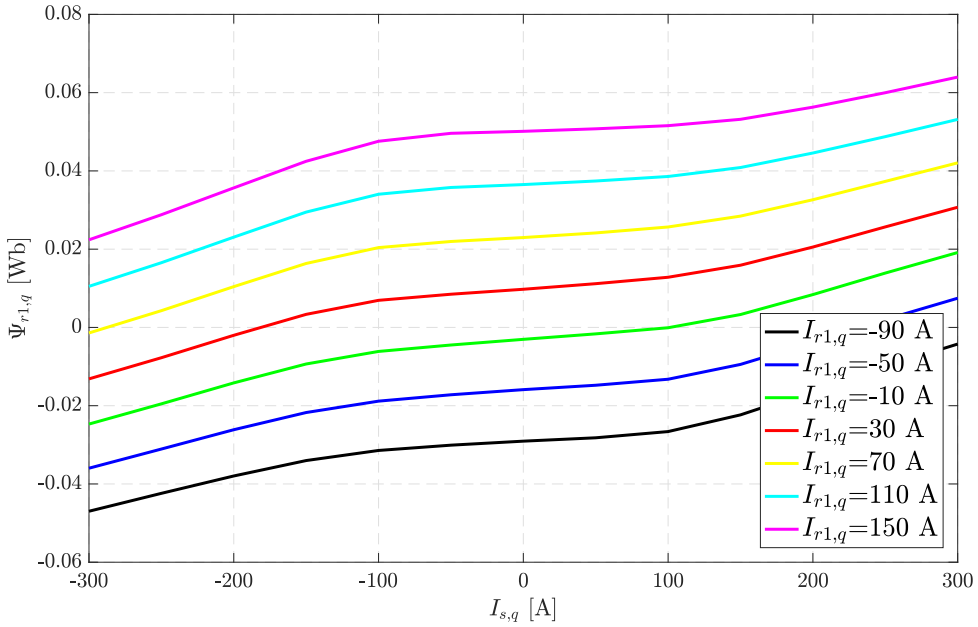

Figure A.15: FEM calculations: the q-axis inner rotor flux $\Psi_{r1,q}$ as function of the q-axis stator current $I_{s,q}$ with parameter: the q-axis inner rotor current $I_{r1,q}$. All other current components are zero.

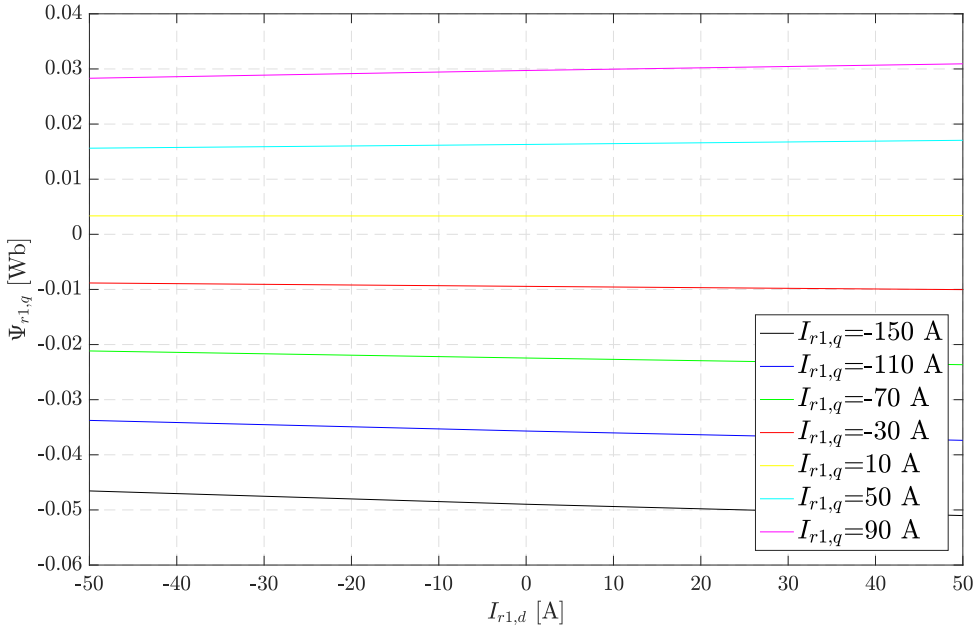

Figure A.16: FEM calculations: the q-axis inner rotor flux $\Psi_{r1,q}$ as function of the d-axis inner rotor current $I_{r1,d}$ with parameter: the q-axis inner rotor current $I_{r1,q}$. All other current components are zero.

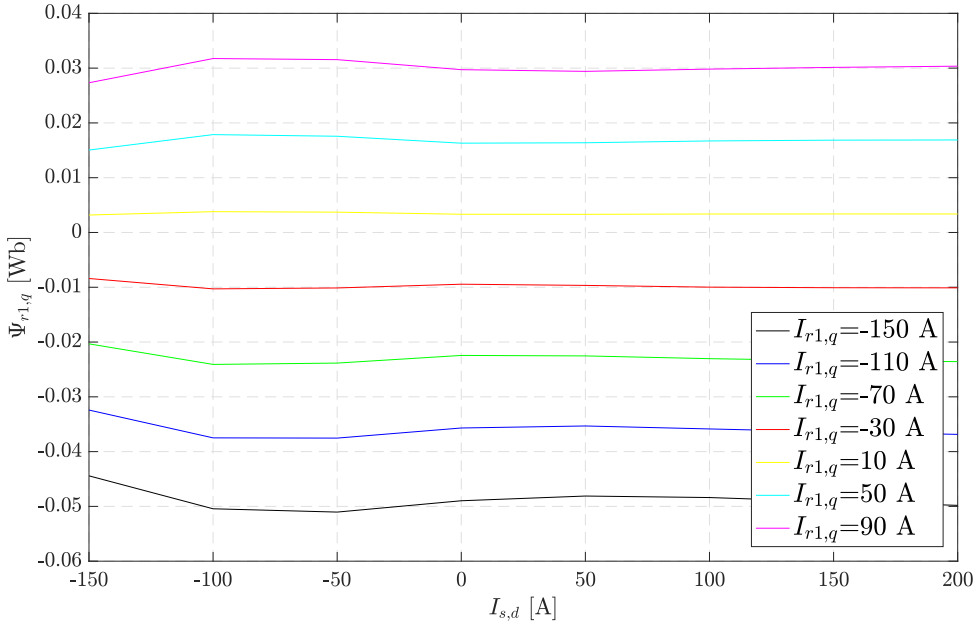

Figure A.17: FEM calculations: the q-axis inner rotor flux $\Psi_{r1,q}$ as function of the d-axis stator current $I_{s,d}$ with parameter: the q-axis inner rotor current $I_{r1,q}$. All other current components are zero.

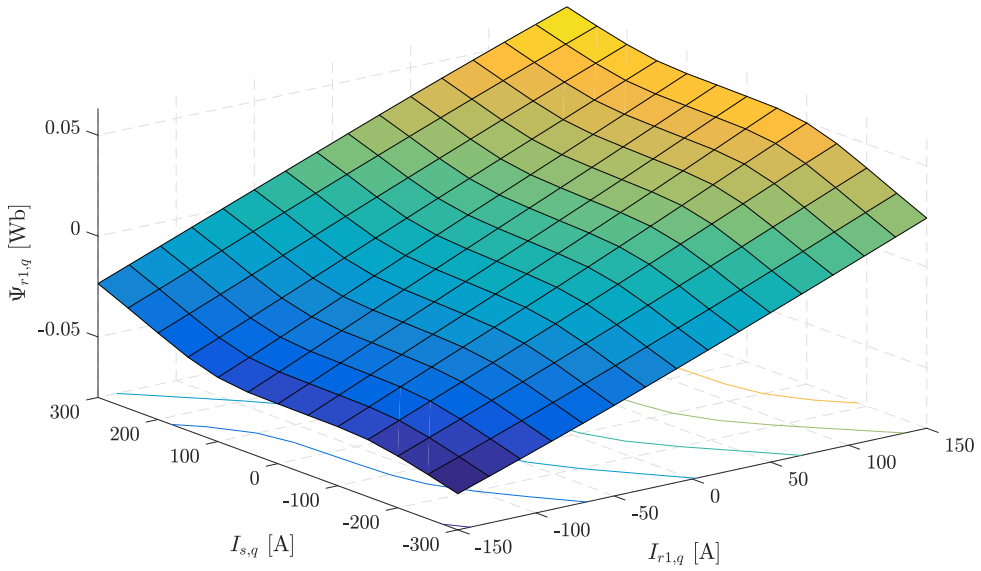

Figure A.18: FEM calculations: the q-axis inner rotor flux $\Psi_{r1,q}$ as function of the q-axis stator current $I_{s,q}$ and q-axis inner rotor current $I_{r1,q}$. The d-axis stator current equals 50 A and the field current equals -2 A.

Appendix B

Controller models

B.1 $\Psi_{s,d} = f(I_{s,d}, I_{r2,d})$

Depending on the stator q-axis current, behaviour of the d-axis stator-flux as a function of the d-axis stator current $I_{s,d}$ and the field current $i_{r2,d}$ is different. Taking in mind the optimal control reference currents, see section 4.4.2, a model for $|I_{s,q}| > 100A$ and $|I_{s,q}| < 100A$ has been derived. This can be seen in figure B.1. This flux-linkage can be described as a function of the equivalent d-axis stator current $I_{s,d,eq}$, see equation 3.21.

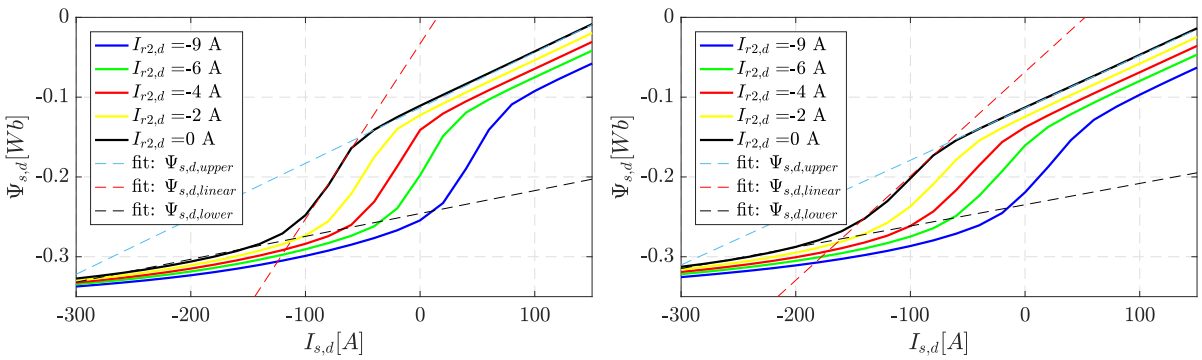

(a) $I_{s,q} = 50A$ (b) $I_{s,q} = 150A$

Figure B.1: Model of $\Psi_{s,d}$ as a function of $I_{s,d}$ and $I_{r2,d}$. No inner rotor currents are applied.

In general this relation can be written as follows:

$$\Psi_{s,d} = L_{s,d} I_{s,d,eq} + \Psi_{s,PM} \tag{B.1}$$

For $I_{s,q} < 100A$ this results in:

$$\begin{cases} \Psi_{s,d,upper} = 0.0006953\, I_{s,d,eq} - 0.1134 - 0.003\, I_{r2,d} & I_{s,d,eq} > -53\, A \\ \Psi_{s,d,linear} = 0.0021972\, I_{s,d,eq} - 0.03304 & I_{s,d,eq} \in [-111, -53]\, A \\ \Psi_{s,d,lower} = 0.00028678\, I_{s,d,eq} - 0.2458 - 0.003\, I_{r2,d} & I_{s,d,eq} < -111\, A \end{cases} \tag{B.2}$$

For $I_{s,q} > 100A$ this results in:

$$\begin{cases} \Psi_{s,d,upper} = 0.0006562\, I_{s,d,eq} - 0.1134 - 0.003\, I_{r2,d} & I_{s,d,eq} > -72\, A \\ \Psi_{s,d,linear} = 0.001306\, I_{s,d,eq} - 0.06829 & I_{s,d,eq} \in [-163, -72]\, A \\ \Psi_{s,d,lower} = 0.0002668\, I_{s,d,eq} - 0.2348 - 0.003\, I_{r2,d} & I_{s,d,eq} < -163\, A \end{cases} \tag{B.3}$$

B.2 $\Psi_{r1,q} = f(I_{r1,q}, I_{s,q})$

As stated in section 4.6, the most important current having the strongest impact on the inner rotor q-axis current $\Psi_{s,q}$ is the corresponding current $I_{r1,q}$. Also the influence of a high q-axis stator current $I_{s,q}$ can be noticed. Taking into account the optimal control reference currents, see section 4.4.2, a model for $|I_{s,q}| > 100A$ and $|I_{s,q}| < 100A$ has been derived. To do this, the matlab-function *fit* was used. The higher the equivalent d-axis current $I_{s,d,eq}$, the smaller the impact of $I_{s,q}$. From section 4.4.2 it is known that for $i_{s,q} > 200A$ the optimal d-axis stator current $I_{s,d}$ becomes negative. Also the field current jumps to a more negative value. In that case, the impact of $I_{s,q}$ will be neglected.

In general this relation can be written as follows:

$$\Psi_{r1,q} = L_{r1,q} I_{r1,q} + L_{r1,s,q} I_{s,q} \tag{B.4}$$

Based on figure A.18, a model is then derived. Note that $L_{r1,s,q}$ is set to be zero when $|I_{s,q}| > 200A$.

$$\begin{cases} \Psi_{r1,q} = 0.0003056\, I_{r1,q} + 0.00009642\, I_{s,q} + 0.008244 & I_{s,q} < -100\, A \\ \Psi_{r1,q} = 0.0003279\, I_{r1,q} + 0.00002421\, I_{s,q} & I_{s,q} \in [-100, 100]\, A \\ \Psi_{r1,q} = 0.0003056\, I_{r1,q} + 0.00009642\, I_{s,q} - 0.00753 & I_{s,q} > 100\, A \end{cases} \tag{B.5}$$

B.3 $\Psi_{r1,d} = f(I_{r1,d}, I_{s,d}, I_{r2,d})$

Since this reference value of this current must be kept zero for the optimal control case, a model of the d-axis inner rotor flux $\Psi_{r1,d}$is derived for small values of the corresponding current $I_{r1,d}$. As stated in section 4.6, the influence of the equivalent d-axis stator current $I_{s,d,eq}$ can be noticed as well.

In general this relation can be written as follows:

$$\Psi_{r1,d} = L_{r1,d} I_{r1,d} + L_{r1,s,d,eq} I_{s,d,eq} + \Psi_{r1,PM} \tag{B.6}$$

Since $I_{s,d,eq}$ is used and a q-axis current has almost no impact on $\Psi_{r1,d}$, figure A.13 is used to derive a model. Again, the matlab-function *fit* can be applied. This results in:

$$\begin{cases} \Psi_{r1,d} = 0.000328\, I_{r1,d} + 0.0002485\, I_{s,d,eq} - 0.1516 & I_{s,d,eq} > -50\, A \\ \Psi_{r1,d} = 0.000234\, I_{r1,d} + 0.00004749\, I_{s,d,eq} - 0.1591 & I_{s,d,eq} < -50\, A \end{cases} \tag{B.7}$$

B.4 $\Psi_{s,q} = f(I_{s,q})$

The q-axis stator current $I_{s,q}$ has a major impact on the corresponding flux $\Psi_{s,q}$. Although neglecting the influence of the equivalent d-axis stator current $I_{s,d,eq}$ is a simplification of the reality, it is possible that the controller knows enough to make an acceptable estimation of the actual current. Taking into account the statements explained in section 4.4.2.

For $I_{s,q}^{ref} < 200A$, the d-axis stator current $I_{s,d}^{ref}$is positive and the field current $i_{r2,d}^{ref}$,being negative, remains small. In this case, the impact of $I_{s,q}$ on the corresponding flux $\Psi_{s,q}$ remains the same. For higher $I_{s,q}^{ref}$, the behaviour changes significantly due to the negative $I_{s,d}^{ref}$ and the highly negative field current $i_{r2,d}$

In general the model can be written as follows:

$$\Psi_{s,q} = L_{s,q} I_{s,q} \tag{B.8}$$

Based on figure 3.13, a model can be derived.

$$\begin{cases} \Psi_{s,q} = 0.0015129\, I_{s,q} & |I_{s,q}| < 72\, A \\ \Psi_{s,q} = 0.00099162\, I_{s,q} + 0.037839 & |I_{s,q}| \in [72, 138]\, A \\ \Psi_{s,q} = 0.0005283\, I_{s,q} + 0.100957 & |I_{s,q}| > 138\, A \end{cases} \tag{B.9}$$

B.5 $\Psi_{s,q} = f(I_{s,q}, I_{s,d}, I_{r2,d})$

The impact of the equivalent d-axis stator current $I_{s,d,eq}$ is not negligible in some cases. This can be seen in figure 3.14. Therefore it can occur that, in some operation modes, the model derived in the previous section performs poorly. Also this model is designed to control certain reference values derived in the optimal control section, see 4.4.2. For the purpose of this thesis however, an accurate model is vital for a robust detection of faults. Therefore it is useful to include this in the model for $\Psi_{s,q}$. Based on figure .... and using the predefined matlab-function *fit* a model was derived.

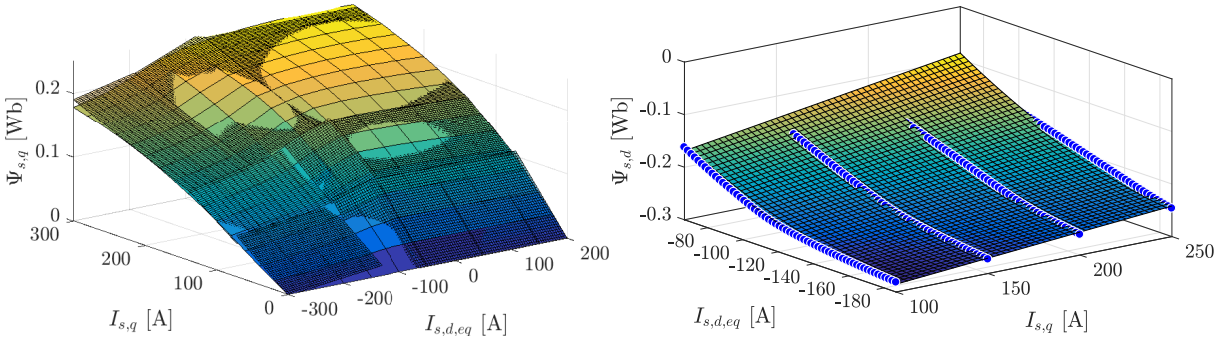

(a) $\Psi_{s,q} = f(I_{s,q}, I_{s,d,eq})$ (b) $\Psi_{s,d} = f(I_{s,q}, I_{s,d,eq})$

Figure B.2: Matlab fit of the stator flux

In general this model can be written as follows:

$$\Psi_{s,q} = L_{s,q} I_{s,q} + L_{s,q,d} I_{s,d,eq} \tag{B.10}$$

Different models have been derived, depending on the the currents $I_{s,q}$ and $i_{s,d,eq}$.

For $|I_{s,q}| < 73A$:

$$\begin{cases} \Psi_{s,q} = 0.0015129\, I_{s,q} + 0.0007\, I_{r2,d} & I_{s,d,eq} > -64A \\ \Psi_{s,q} = 0.0015129\, I_{s,q} + 0.000245\, (I_{s,d,eq} + 64) + 0.0007\, I_{r2,d} & I_{s,d,eq} \in [-130, -64]A \\ \Psi_{s,q} = 0.0009129\, I_{s,q} + 0.000245 \cdot 66 + 0.000103\, (I_{s,d,eq} + 130) + 0.0005\, I_{r2,d} & I_{s,d,eq} < -130A \end{cases} \tag{B.11}$$

For $|I_{s,q}| \in [73, 138]A$:

$$\begin{cases} \Psi_{s,q} = 0.00099162\, I_{s,q} - 0.00002857\, I_{s,d,eq} + 0.037839 + 0.0015\, I_{r2,d} & I_{s,d,eq} > -50A \\ \Psi_{s,q} = 0.00099162\, I_{s,q} + 0.000373\, (I_{s,d,eq} + 60) + 0.037839 + 0.0015\, I_{r2,d} & I_{s,d,eq} \in [-130, -50]A \\ \Psi_{s,q} = 0.00085162\, I_{s,q} + 0.000205\, I_{s,d,eq} + 0.0525 & I_{s,d,eq} < -130A \end{cases} \tag{B.12}$$

For $|I_{s,q}| > 138A$:

$$\begin{cases} \Psi_{s,q} = 0.0005083\, I_{s,q} + 0.100957 + 0.0008\, I_{r2,d} & I_{s,d,eq} > -74A \\ \Psi_{s,q} = 0.0005083\, I_{s,q} + 0.00035\, (I_{s,d,eq} + 74) + 0.100957 + 0.0008\, I_{r2,d} & I_{s,d,eq} \in [-190, -74]A \\ \Psi_{s,q} = 0.0005083\, I_{s,q} + 0.000203\, (I_{s,d,eq} + 190) + 0.060357 + 0.0008\, I_{r2,d} & I_{s,d,eq} < -190A \end{cases} \tag{B.13}$$

B.6 $\Psi_{s,d} = f(I_{s,q}, I_{s,d}, I_{r2,d})$

Similarly to the previous section, omitting $I_{s,q}$ in the model for the d-axis stator flux $\Psi_{s,d}$ is a major simplification in certain operation points. This can be seen from figure A.4 and A.5. It is shown in section 4.4.2 that the equivalent d-axis stator current$I_{s,d,eq}$ can be used to determine $\Psi_{s,d}$. Note that the effect of $I_{s,d,eq}$ changes for different values of $I_{s,q}$. This was taken into account in section B.1 by using two different models depending on $I_{s,q}$.

The impact of $I_{s,q}$ when $I_{s,d,eq} > 0$, is non-existent. For negative $I_{s,d,eq}$ the effect can be noticed when the current $I_{s,q} > 100A$. This is not incorporated in the models described in section B.1. For similar reasons stated in the previous section, it can be useful to take this impact into account. To do this, the model is recalculated for negative values of $I_{s,d,eq}$ and $I_{s,q}$ >100 A. Only then the effect of $I_{s,q}$ is relevant. This is done, again, using the matlab-function *fit*. Only now, instead of using planes, curved surfaces are used. For a highly negative equivalent d-axis stator current the effect of $I_{s,q}$ vanishes and the impact of $I_{s,d,eq}$ becomes constant. This was also taken into account designing the model for negative $I_{s,d,eq}$. If $I_{s,d,eq} > O$, the model described in section B.1 is used.

$$\begin{aligned} \Psi_{s,d} = -0.0834 + 0.0006764\, I_{s,q} + 0.002559\, I_{s,d,eq} + 2.075 \cdot 10^{-6}\, I_{s,q}\, I_{s,d,eq} \\ + 7.0897 \cdot 10^{-6}\, I_{s,d,eq}^2 \end{aligned} \tag{B.14}$$

Bibliography

[1] J.-C. Trigeassou, *Electrical Machines Diagnosis*. John Wiley & Sons, 2013.

[2] IEEE, "Ieee recommended practice for the design of reliable industrial and commercial power systems," *IEEE Std 493-2007 (Revision of IEEE Std 493-1997)*, pp. 1–689, June 2007.

[3] N. M. Y. U. B. V. Prashant W.Thamke and P. G. Asutkar, "Faults associated with permanent magnet synschronous motors," *International journal of Core Engineering and Management (IJCEM)*, vol. 2, June 2015.

[4] G. J. Paoletti and A. Golubev, "Partial discharge theory and technologies related to medium-voltage electrical equipment," *IEEE Transactions on Industry Applications*, vol. 37, no. 1, pp. 90–103, Jan 2001.

[5] L. Liu, "Robust fault detection and diagnosis for permanent magnet synchronous motors," Ph.D. dissertation, Florida State University, 2006.

[6] J. Druant, H. Vansompel, F. De Belie, J. Melkebeek, and P. Sergeant, "Torque analysis on a double rotor electrical variable transmission with hybrid excitation," *IEEE Transactions on Industrial Electronics*, 2016.

[7] J. Druant, F. De Belie, P. Sergeant, and J. Melkebeek, "Power flow in an induction machine based electrical variable transmission," in *2016 INTERNATIONAL SYMPOSIUM ON POWER ELECTRONICS, ELECTRICAL DRIVES, AUTOMATION AND MOTION (SPEEDAM)*, 2016, pp. 1197–1202.

[8] J. Druant, "Model based predictive control of multi-level inverters with integrated fault detection," Master's thesis, University of Ghent, EESA, EELAB, June 2013.

[9] J. Druant, H. Vansompel, F. De Belie, and P. Sergeant, "Optimal control for a hybrid excited dual mechanical port electric machine," *IEEE TRANSACTIONS ON ENERGY CONVERSION*, 2017. [Online]. Available: http://dx.doi.org/10.1109/TEC.2017.2651581

[10] E. D. Brabandere, "Model predictive torque control on an electric variable transmission for hybrid electric vehicles," Master's thesis, University of Ghent, EESA, EELAB, June 2015.

[11] P. F. Albrecht, J. C. Appiarius, R. M. McCoy, E. L. Owen, and D. K. Sharma, "Assessment of the reliability of motors in utility applications - updated," *IEEE Transactions on Energy Conversion*, vol. EC-1, no. 1, pp. 39–46, March 1986.

[12] A. H. Bonnett and C. Yung, "Increased efficiency versus increased reliability," *IEEE Industry Applications Magazine*, vol. 14, no. 1, pp. 29–36, Jan 2008.

[13] W. H. Kersting, "Causes and effects of single-phasing induction motors," *IEEE Transactions on Industry Applications*, vol. 41, no. 6, pp. 1499–1505, Nov 2005.

[14] S. Nandi and H. A. Toliyat, "Condition monitoring and fault diagnosis of electrical machines-a review," in *Conference Record of the 1999 IEEE Industry Applications Conference. Thirty-Forth IAS Annual Meeting (Cat. No.99CH36370)*, vol. 1, 1999, pp. 197–204 vol.1.

[15] K. Fonstad, "Variable frequency drives and motor insulation stresses." ABB, Tech. Rep., August 2011.

[16] T. G. Arora, M. V. Aware, and D. R. Tutakne, "Effect of pulse width modulated voltage on induction motor insulation," in *2012 7th IEEE Conference on Industrial Electronics and Applications (ICIEA)*, July 2012, pp. 2044–2048.

[17] R. M. Tallam, S. B. Lee, G. C. Stone, G. B. Kliman, J. Yoo, T. G. Habetler, and R. G. Harley, "A survey of methods for detection of stator-related faults in induction machines," *IEEE Transactions on Industry Applications*, vol. 43, no. 4, pp. 920–933, July 2007.

[18] Y. Gritli, "Diagnosis and fault detection in electrical machines and drives based on advanced signal processing techniques," Ph.D. dissertation, university Di Bolonga.

[19] J. Melkebeek, *Controlled Electrical Drives*. University of Ghent, 2016.

[20] T. Billard, T. Lebey, and F. Fresnet, "Partial discharge in electric motor fed by a pwm inverter: off-line and on-line detection," *IEEE Transactions on Dielectrics and Electrical Insulation*, vol. 21, no. 3, pp. 1235–1242, June 2014.

[21] J. Melkebeek, *Dynamics of Electrical Machines and Drives*. University of Ghent, 2016.

[22] D. Huger and D. Gerling, "An advanced lifetime prediction method for permanent magnet synchronous machines," in *2014 International Conference on Electrical Machines (ICEM)*, Sept 2014, pp. 686–691.

[23] L. Szab, D. Fodorean, and A. Vasilache, "Bearing fault detection of electrical machines used in automotive applications," in *2016 XXII International Conference on Electrical Machines (ICEM)*, Sept 2016, pp. 2184–2190.

[24] E. Elbouchikhi, V. Choqueuse, Y. Amirat, M. E. H. Benbouzid, and S. Turri, "An efficient hilbert huang transform-based bearing faults detection in induction machines," *IEEE Transactions on Energy Conversion*, vol. 32, no. 2, pp. 401–413, June 2017.

[25] R. Z. Haddad and E. G. Strangas, "Detection of static eccentricity and turn-to-turn short circuit faults in permanent magnet synchronous ac machines," in *2015 IEEE 10th International Symposium on Diagnostics for Electrical Machines, Power Electronics and Drives (SDEMPED)*, Sept 2015, pp. 277–283.

[26] J. Hong, S. B. Lee, C. Kral, and A. Haumer, "Detection of airgap eccentricity for permanent magnet synchronous motors based on the d-axis inductance," in *8th IEEE Symposium on Diagnostics for Electrical Machines, Power Electronics Drives*, Sept 2011, pp. 378–384.

[27] B. M. Ebrahimi, J. Faiz, and B. N. Araabi, "Pattern identification for eccentricity fault diagnosis in permanent magnet synchronous motors using stator current monitoring," *IET Electric Power Applications*, vol. 4, no. 6, pp. 418–430, July 2010.

[28] G. Vinson, M. Combacau, T. Prado, and P. Ribot, "Permanent magnets synchronous machines faults detection and identification," in *IECON 2012 - 38th Annual Conference on IEEE Industrial Electronics Society*, Oct 2012, pp. 3925–3930.

[29] D. c. Giancoli, *Natuurkunde- Deel 2*. Pearson benelux B.V., 2009.

[30] D. Casadei, F. Filippetti, C. Rossi, and A. Stefani, "Magnets faults characterization for permanent magnet synchronous motors," in *2009 IEEE International Symposium on Diagnostics for Electric Machines, Power Electronics and Drives*, Aug 2009, pp. 1–6.

[31] J. O. Estima and A. J. M. Cardoso, "Impact of inverter faults in the overall performance of permanent magnet synchronous motor drives," in *2009 IEEE International Electric Machines and Drives Conference*, May 2009, pp. 1319–1325.

[32] C. C. Chan, A. Bouscayrol, and K. Chen, "Electric, hybrid, and fuel-cell vehicles: Architectures and modeling," *IEEE transactions on vehicular technology*, vol. 59, no. 2, pp. 589–598, 2010.

[33] X. Sun, M. Cheng, Y. Zhu, and L. Xu, "Application of electrical variable transmission in wind power generation system," *IEEE Transactions on Industry Applications*, vol. 49, no. 3, pp. 1299–1307, 2013.

[34] Y. Cheng, C. Espanet, R. Trigui, A. Bouscayrol, and S. Cui, "Design of a permanent magnet electric variable transmission for hev applications," in *2010 IEEE Vehicle Power and Propulsion Conference*, Sept 2010, pp. 1–5.

[35] P. S. J. Druant, F. De Belie and J. Melkebeek, "Field oriented control for an induction-machine-based electrical variable transmission," *IEEE TRANSACTIONS ON VEHICULAR TECHNOLOGY*, vol. 65, no. 6, pp. 4230–4240, 2016. [Online]. Available: http://dx.doi.org/10.1109/TVT.2015.2496625

[36] F. De Belie, E. De Brabandere, J. Druant, P. Sergeant, and J. Melkebeek, "Model based predictive torque control of an electric variable transmission for hybrid electric vehicles," in *2016 INTERNATIONAL SYMPOSIUM ON POWER ELECTRONICS, ELECTRICAL DRIVES, AUTOMATION AND MOTION (SPEEDAM)*, 2016, pp. 1205–1209.

[37] M. Hoeijmakers, "Rotating electromechanical converter," U.S. Patent US 9 018 863, April 28, 2015.

[38] E. Nordlund and C. Sadarangani, "The four-quadrant energy transducer," in *Conference Record of the 2002 IEEE Industry Applications Conference. 37th IAS Annual Meeting (Cat. No.02CH37344)*, vol. 1, Oct 2002, pp. 390–397 vol.1.

[39] J. Melkebeek, *Elektrische Aandrijftechniek*. University of Ghent, 2016.

[40] F. Verbelen, J. Druant, S. Derammelaere, H. Vansompel, F. De Belie, K. Stockman, and P. Sergeant, "Benchmarking the permanent magnet electrical variable transmission against the half toroidal continuously variable transmission," *MECHANISM AND*

MACHINE THEORY, vol. 113, pp. 141–157, 2017. [Online]. Available: http://dx.doi.org/10.1016/j.mechmachtheory.2017.03.005

[41] Y. Cheng, A. Bouscayrol, R. Trigui, and C. Espanet, "Inversion-based control of a pm electric variable transmission," in *2011 IEEE Vehicle Power and Propulsion Conference*, Sept 2011, pp. 1–6.

[42] Y. Cheng, R. Trigui, C. Espanet, A. Bouscayrol, and S. Cui, "Specifications and design of a pm electric variable transmission for toyota prius ii," *IEEE Transactions on Vehicular Technology*, vol. 60, no. 9, pp. 4106–4114, 2011.

[43] B. Denys, "Emulating a hybrid electric vehicle with an electric variable transmission," Master's thesis, University of Ghent, EESA, EELAB, June 2016.

[44] J. Druant, P. Sergeant, F. De Belie, and J. Melkebeek, "Modeling and control of an induction machine based electric variable transmission," in *Young Researchers Symposium, Proceedings*, 2014, p. 5.

[45] L. Guzzella and C. Onder, *Introduction to modeling and control of internal combustion engine systems*. Springer Science & Business Media, 2009.

[46] S. Kouro, P. Cortés, R. Vargas, U. Ammann, and J. Rodríguez, "Model predictive controla simple and powerful method to control power converters," *IEEE Transactions on Industrial Electronics*, vol. 56, no. 6, pp. 1826–1838, 2009.

[47] V. Yaramasu and B. Wu, *Model Predictive Control of Wind Energy Conversion Systems*. John Wiley & Sons, 2016.

[48] A. Merabet, L. Labib, and A. M. Y. M. Ghias, "Robust model predictive control for photovoltaic inverter system with grid fault ride-through capability." *IEEE Transactions on Smart Grid*, vol. PP, no. 99, pp. 1–1, 2017.

[49] R. D. Keyser, *Computer control of Industrial Processes*. University of Ghent, 2016.